

**SHEET RESISTIVITY OF DIAMOND-LIKE CARBON
FILMS PREPARED BY HIGH POWER IMPULSE
MAGNETRON SPUTTERING TECHNIQUE**



Ponthip Chaiyabin

**A Thesis Submitted in Partial Fulfillment of the Requirements for the
Degree of Master of Science in Applied Physics
Suranaree University of Technology
Academic Year 2020**

คำสภาพัฒนาการเชิงแผ่นของฟิล์มคาร์บอนคล้ายเพชรเตรียมโดย
เทคนิคไฮพลาเวอร์อิมแพคส์แมกนีตรอนสปัตเตอร์ริง



วิทยานิพนธ์นี้เป็นส่วนหนึ่งของการศึกษาตามหลักสูตรปริญญาวิทยาศาสตรมหาบัณฑิต
สาขาวิชาฟิสิกส์ประยุกต์
มหาวิทยาลัยเทคโนโลยีสุรนารี
ปีการศึกษา 2563

SHEET RESISTIVITY OF DIAMOND-LIKE CARBON FILMS

PREPARED BY HIGH POWER IMPULSE MAGNETRON

SPUTTERING TECHNIQUE

Suranaree University of Technology has approved this thesis submitted in partial fulfillment of the Requirements for the Degree of Master of Science in Applied Physics.

Thesis Examining Committee



(Assoc. Prof. Dr. Panomsak Meemon)

Chairperson



(Assoc. Prof. Dr. Prayoon Songsiriritthigul)

Member (Thesis Advisor)



(Dr. Ratchadaporn Supruangnet)

Member (Thesis Co-Advisor)



(Asst. Prof. Dr. Phitsanu Poolcharuansin)

Member



(Assoc. Prof. Dr. Chatchai Jothityangkoon)

Vice Rector for Academic Affairs
and Quality Assurance



(Prof. Dr. Santi Maensiri)

Dean of Institute of Science

พรทิพย์ ชัยบัล : ค่าสภาพต้านทานเชิงแผ่นของฟิล์มคาร์บอนคล้ายเพชรเตรียมโดยเทคนิค
ไฮพาวเวอร์อิมแพลส์แมกนีตรอนสปัตเตอร์ริง (SHEET RESISTIVITY OF DIAMOND-LIKE
CARBON PREPARED BY HIGH POWER IMPULSE MAGNETRON SPUTTERING
TECHNIQUE) อาจารย์ที่ปรึกษา : รองศาสตราจารย์ ดร.ประยูร ส่งสิริฤทธิกุล, 93 หน้า.

ฟิล์มคาร์บอนคล้ายเพชร/ค่าสภาพต้านทานเชิงแผ่น/ไฮพาวเวอร์อิมแพลส์แมกนีตรอนสปัตเตอร์ริง/
เครื่องตรวจจับแพนด้ารุ่นที่ 3/อนุภาคฟิลิกส์

วิทยานิพนธ์นี้มุ่งเน้นไปที่การศึกษาความเป็นไปได้ในการใช้ฟิล์มบางคาร์บอนคล้ายเพชร (DLC) เป็นตัวต้านทานแบบฟิล์มบางในเครื่องตรวจวัดอนุภาคมูลฐานที่มีชื่อเรียกว่า PandaX-III ในงานนี้ ฟิล์มบางคาร์บอนคล้ายเพชรถูกเตรียมโดยใช้เทคนิคแมกนีตรอนสปัตเตอร์กำลังแรงสูง องค์ประกอบของฟิล์ม บางคาร์บอนคล้ายเพชรถูกวิเคราะห์โดยเทคนิคสเปกโทสโกปีของโฟโตอิเล็กตรอนที่ถูกกระตุ้นโดยรังสีเอกซ์ (X-ray photoelectron spectroscopy, XPS) และ สเปกโทสโกปีการดูดกลืนรังสีเอกซ์ (X-ray absorption spectroscopy, XAS) การวิเคราะห์ด้วยเทคนิคดังกล่าวสามารถระบุปริมาณคาร์บอนชนิด sp^2 และ sp^3 ในฟิล์มบางได้ นอกจากนี้ยังตรวจพบการปนเปื้อนของคาร์บอนและออกซิเจน ในการเตรียมฟิล์มนั้น ประเภทของปั๊มสุญญากาศที่ใช้ในการสร้างสุญญากาศในห้องสปัตเตอร์ต้องมีการพิจารณาเพื่อลดการปนเปื้อนของไฮโดรคาร์บอนในฟิล์มบาง นอกจากนี้ ยังได้ศึกษาการปลดปล่อยแก๊สของวัสดุที่ใช้เป็นฐานรองฟิล์มบางที่โค้งงอได้เพื่อให้ข้อมูลในการเลือกฐานรองที่เหมาะสม พบว่า Kapton เป็นฐานรองที่โค้งงอได้และเหมาะสมสำหรับใช้ปลูกฟิล์มบาง DLC ที่จะใช้ในเครื่องตรวจจับ PandaX-III วัดความต้านทานแผ่นของฟิล์มคาร์บอนคล้ายเพชร ได้มีการศึกษาค่าความต้านทานของฟิล์มบางที่ช่วงอุณหภูมิระหว่างอุณหภูมิห้องและอุณหภูมิใน โตรเจนเหลว ที่อุณหภูมิห้อง ค่าความต้านทานของฟิล์มบางที่มีความหนามากกว่า 45 นาโนเมตรมีค่าประมาณ 0.37 และมีค่าเพิ่มขึ้นเป็น 3.23 กิกะโอห์ม/ตร.ม. หากฟิล์มมีความหนามากกว่า 45 นาโนเมตร ค่าความต้านทานของฟิล์มบางคาร์บอนคล้ายเพชรเพิ่มขึ้นเมื่ออุณหภูมิลดลง และที่อุณหภูมิการทำงานของ PandaX-III ซึ่งเป็นอุณหภูมิของซีนอนเหลว ค่าความต้านทานของฟิล์มบางคล้ายเพชรมีค่าสูงถึงหลายร้อยกิกะโอห์ม แสดงให้เห็นว่าฟิล์มบางคาร์บอนคล้ายเพชรที่เตรียมขึ้นในงานนี้มีคุณสมบัติทางไฟฟ้าที่เหมาะสมสำหรับใช้เป็นตัวต้านทานความต้านทานใน PandaX-III

สาขาวิชาฟิสิกส์
ปีการศึกษา 2563

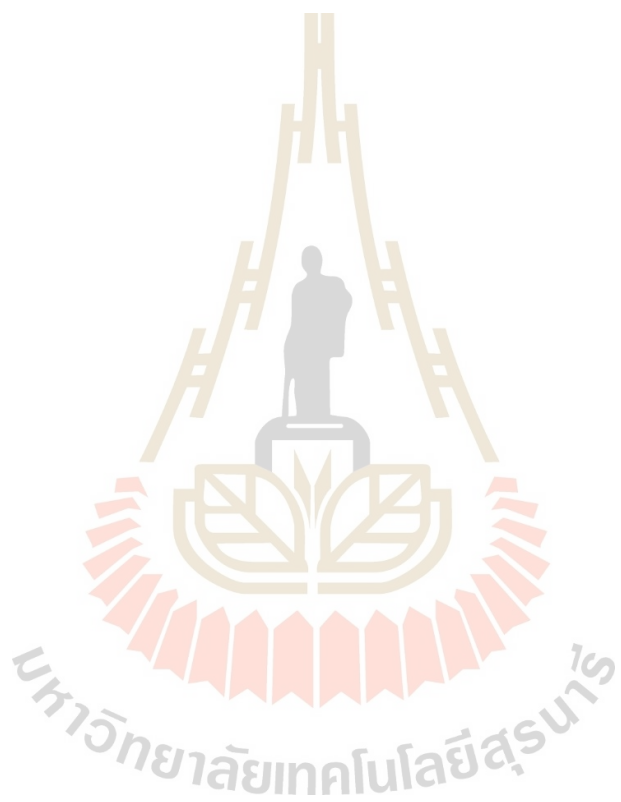
ลายมือชื่อนักศึกษา พรทิพย์ ชัยบัล
ลายมือชื่ออาจารย์ที่ปรึกษา ประยูร ส่งสิริฤทธิกุล
ลายมือชื่ออาจารย์ที่ปรึกษาร่วม ผ

PONTHIP CHAIYABIN : SHEET RESISTIVITY OF DIAMOND LIKE
CARBON FILMS PREPARED BY HIGH POWER IMPULSE MAGNETRON
SPUTTERING TECHNIQUE. THESIS ADVISOR : ASSOC. PROF. PRAYOON
SONGSIRIRITTHIGUL, Ph.D. 93 PP.

DIAMOND-LIKE CARBON/SHEET RESISTIVITY/HIPIMS/PANDAX-III
DETECTOR/PARTICLE PHYSICS

This thesis focused on the feasibility study for utilization of diamond-like carbon (DLC) thin films as resistive films in an elementary particle detector, namely PandaX-III detector. In this work, DLC films were deposited by using a high-power impulse magnetron sputtering (HiPIMS) technique. The composition of the DLC films were characterized by X-ray photoelectron spectroscopy and X-ray absorption spectroscopy. The sp^2 and sp^3 carbon contents in the films could be identified. Carbon and oxygen contaminations were also detected. Types of vacuum pumps used to evacuate gas in the sputtering chamber must be considered to reduced hydro-carbon contamination in the DLC film. Out-gassing of bendable substrate materials were also studied to provide information for choosing a proper substrate. It was found that Kapton is a proper bendable substrate for DLC films to be used in the PandaX-III detector. Sheet resistivity of the DLC films between room and liquid nitrogen temperatures was measured. At room temperature, the sheet resistivity was approximately 0.37 and 3.23 giga-ohm/sqm. for DLC films with thickness larger and smaller than 45 nm, respectively. The resistance of the DLC films increases when decreasing temperature. At the operating temperature of the PandaX-III, at the liquid xenon temperature, the resistance of the DLC films could be as high as hundreds of giga-ohm.

This suggests that DLC films in this work have electrical property suitable for being used as resistive resistor in the PandaX-III.



School of Physics

Academic Year 2020

Student's signature _____ พรทิพย์ ชัยนิล

Advisor's signature _____ ช.ป. อ.

Co-advisor's signature _____ อ.

ACKNOWLEDGEMENTS

The main part of this work was conducted at the Synchrotron Light Research Institute and the Department of Physics of Mahasarakham University under co-supervision Assoc. Prof. Dr. Prayoon Songsiriritthigul, Dr. Ratchadaporn Supruangnet and Asst. Prof. Dr. Phitsanu Poolcharuansin. Their guidance and support are gratefully acknowledged. I would also like to thank Prof. K.L. Giboni, T. Zhang, C. Kobdaj, and Y. Yupeng for providing me the opportunity to be trained at the Department of Physics of Shanghai Jiao Tong University and the Shanghai Key Laboratory for Particle Physics and Cosmology (INPAC) under the PandaX-III Project.

Many of my friends at SUT and SLRI are thankful for making my life at SUT unforgettable. I am deeply appreciated Dr. Tanachat Eknapakul and Jidapa Lomom for assisting in compiling this thesis book. The scholarship from the Synchrotron Light Research Institute (Public Organization) is greatly acknowledged.

Never-ending supports and love from my parents, sister and brother contributing to my success are greatly acknowledged.

Ponthip Chaiyabin

CONTENTS

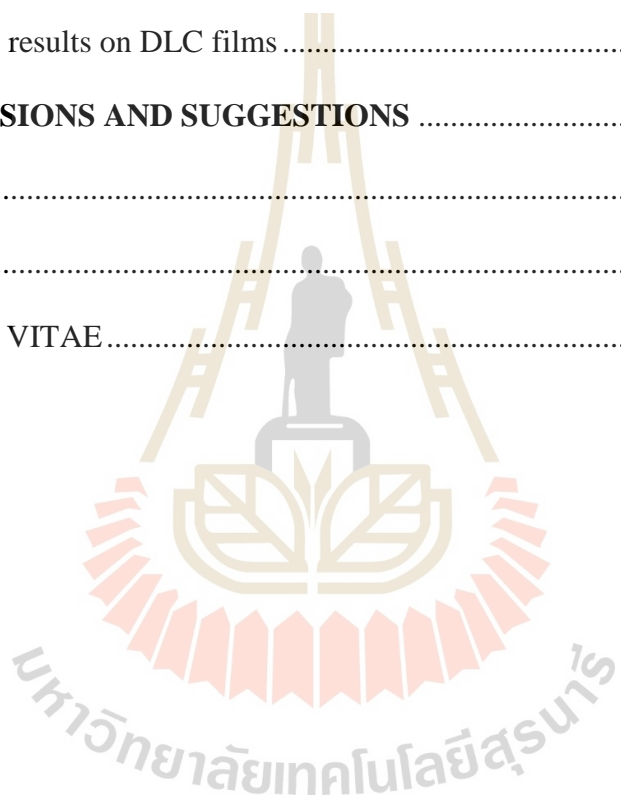
	Page
ABSTRACT IN THAI.....	I
ABSTRACT IN ENGLISH	II
ACKNOWLEDGEMENTS	IV
CONTENTS.....	V
LIST OF FIGURES	VIII
LIST OF TABLES	XIV
LIST OF ABBREVIATION	XV
CHAPTER	
I INTRODUCTION.....	1
1.1 The Background and Applications of Diamond-like carbon (DLC).....	1
1.2 Research objectives.....	6
1.3 Scope and limitation of the study.....	6
II LITERATURE REVIEW.....	7
2.1 The diamond-like carbon (DLC) films.....	7
2.1.1 Physical properties of DLC films.....	10
2.1.2 Thermal properties of graphene	12
2.2 DLC films deposition techniques.....	17
2.2.1 Direct current (DC) technique.....	18
2.2.2 Radio frequency (RF) technique	19
2.2.3 High power impulse magnetron sputtering (HiPIMS) technique	21
2.2.4 Ion deposition technique	25

CONTENTS (Continued)

	Page
2.2.5 Pulsed laser deposition (PLD) technique	26
2.3 Related properties of DLC films	28
2.3.1 Uniform electron gas.....	28
2.3.2 Hall effect.....	29
2.4 The application of DLC films for PandaX-III.....	30
2.5 DLC films characterization techniques	35
2.5.1 X-ray photoemission spectroscopy (XPS)	36
2.5.2 X-ray absorption spectroscopy (XAS).....	38
III EXPERIMENTS and METHODS.....	43
3.1 The HiPIMS system and setup.....	43
3.2 Outgassing measurements.....	50
3.3 Charaterization techniques.....	51
3.3.1 principle of synchrotron radiation.....	51
3.3.2 BL3.2Ua of the Synchrotron Light Research Institute (SLRI)	54
3.3.3 principle of XPS.....	55
3.3.4 principle of XAS	59
IV RESULTS AND DISCUSSIONS.....	65
4.1 DLC films properties.....	65
4.1.1 DLC films thickness.....	66
4.1.2 DLC films homogeneity.....	66
4.2 DLC films resistivity.....	68
4.2.1 DLC films resistivity at various thicknesses.....	69

CONTENTS (Continued)

	Page
4.2.2 DLC films resistivity as a function of growing position.....	71
4.2.3 DLC resistivity as a function of temperature	72
4.3 Raman spectroscopy results on DLC films	73
4.4 XPS results on DLC films.....	76
4.5 XAS results on DLC films	79
V CONCLUSIONS AND SUGGESTIONS	82
REFERENCES	84
APPENDIX.....	91
CURRICULUM VITAE.....	93



LIST OF FIGURES

Figure	Page
1.1 The ternary phase diagram of hardness and coefficient of friction map for various compositions of popular carbon-based materials.....	2
1.2 All-carbon device applications in various fields	3
1.3 In the last four decades, the number of papers on diamond-like carbon coatings has increased dramatically (data from Scopus database for all DLC modifications).....	4
1.4 Comparing DCMS versus HiPIMS deposition technique	5
1.5 Different heterogeneous materials are depicted schematically based on structural complexity	6
2.1 Amorphous and nanocrystalline carbon sheets in a ternary phase diagram	8
2.2 Electrical resistivity of materials	9
2.3 a) An a-C:H film having a density of 1.7 g/cm ³ , 30% hydrogen, 65 percent sp ² , 20 percent sp ³ , and 15 percent sp ¹ bonds has a structure model. Interactions between ions and films during the formation of ta-C and a-C:H: b) direct and indirect subplantations, c) a-C:H growth scheme, d) a-C:H growth scheme.....	10
2.4 a) Structural comparison of diamond, DLC and graphite. b) Characteristic diagram of DLC.....	11
2.5 Carbon allotropes and their derivatives have different thermal characteristics. a) Diagram based on literature-reported mean values. b) the thermal conductivity of a variety of carbon allotropes as a function of temperature	13

LIST OF FIGURES (Continued)

Figure	Page
2.6 (a) The use of nonequilibrium molecular dynamics (NEMD) to investigate thermal transport in GNR is depicted in this diagram. (b) GNR representations of several fault types	14
2.7 A three-dimensional nanotube architecture that combines poles, carbon nanotubes, and graphene sheets to produce tunable cross-plane heat transmission is shown in this schematic diagram	15
2.8 Rational design of the Pt ₁ /OLC catalyst undergoes a reduction in size and introduces curvature	16
2.9 Typical DLC Production Process	17
2.10 Scheme of DC ion plating deposition system.....	18
2.11 The radio frequency magnetron PECVD deposition device is seen in a schematic diagram.....	19
2.12 Schematic of RF capacitatively coupled plasma (CCP) chemical vapour deposition system	20
2.13 Scheme of RF glow discharge deposition system	21
2.14 Diagram of the HiPIMS Process	22
2.15 Schematic diagram of experimental apparatus.....	23
2.16 Schematic diagram of (a) the inverted magnetron and (b) experimental arrangements.....	24
2.17 a) Scheme of ion-beam deposition technique. B) Scheme of dual beam deposition system	26
2.18 Schematic diagram of PLD technique	27

LIST OF FIGURES (Continued)

Figure	Page
2.19 Comparison between the $H(r_s, t)$ from the PBE correlation and $[S(r_s, t) - 1]\epsilon_c(r_s)$ for two different electron densities	28
2.20 Magnetization direction controlled physical properties	29
2.21 The schematic cross section of the 10 cm x 10 cm resistive MicroMEGAS with sputtered carbon, as well as an image of a prototype chamber are shown below	31
2.22 Large resistivity map for resistive strip foil. Resistivity of the surface as a function of sputtered carbon thickness	32
2.23 On a semilogarithmic scale, resistance fluctuation in megaohms of pure DLC and 8 percent boron-doped DLC versus temperature	33
2.24 a) The field cage mock-final up's design. The acrylic thickness was raised to 50 mm. b) Aerial image of the PandaX III detector by an artist	34
2.25 Schematic view of the PandaX III detector	35
2.26 a) At various laser intensities, XPS C 1s peaks of a graphite target, diamond thin film, and DLC thin films were obtained. b) Deconvolution of the DLC films deposited at 0.9×10^8 and 7.1×10^8 W/cm ² XPS C 1s peaks	37
2.27 Experimental and fitted NEXAFS spectra of (a) UNCD/a-C:H film deposited, (b) a-C film deposited, and (c) a-C:H film.....	39
2.28 Measured (black dotted line) and fitted (red line) C k-edge taken from ta-C film.....	40

LIST OF FIGURES (Continued)

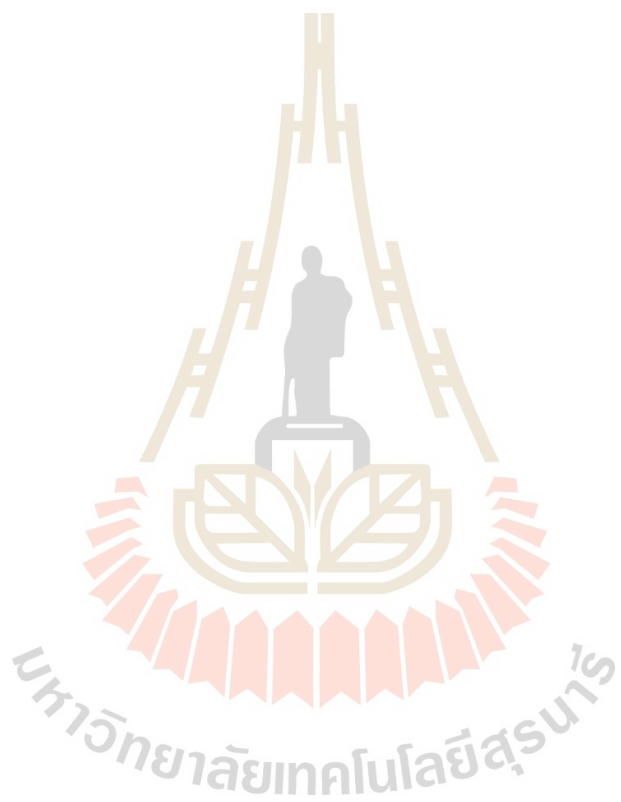
Figure	Page
2.29 The XPS N 1s and XAS N k-edge spectra of the sample with nitrogen content before and after annealing.....	41
3.1 Schemes of HiPIMS	44
3.2 a) Setting up HiPIMS technique at Mahasarakham University and b) HiPIMS at SLRI Thailand.....	45
3.3 a) Graphite target and b) sputtering system.....	46
3.4 Plasma in HiPIMS and starting deposition time.....	47
3.5 a) Holder substrate with 1 series, b) substrate as Kapton foil with pattern, c) DLC films after deposited and d) DLC films as pattern on glass substrates.....	48
3.6 a) Measuring resistance of DLC films by mega-ohmmeter with liquid nitrogen environment and b) test probe.....	49
3.7 a) Laser interferometer instrument for measured thickness of DLC films. b) Measuring resistance of DLC films by pico-ammeter and c) electronics shield with stainless steel foil box.....	50
3.8 Scheme of PTFE and acrylic outgassing measurement.....	51
3.9 The principal structures of the synchrotron.....	52
3.10 The spectrum range of the synchrotron radiation.....	53
3.11 XPS and XAS measurements at BL3.2Ua: PES	55
3.12 the electronic state exists in the atom	56
3.13 The universal inelastic mean free path curve	58
3.14 The X-ray absorption mechanism is depicted in this diagram	60

LIST OF FIGURES (Continued)

Figure	Page
3.15 The hydrogen molecule's MO diagram. Two σ molecular orbitals are formed from two 1s atomic orbitals	61
3.16 (a) Raw drain current spectrum. (b) the Mesh current corrects the spectrum. (c) the mesh's carbon contamination was removed from the spectra. (d) spectrum with the pre-edge (280 eV) and post-edge (320 eV) set to 0 and 1, respectively	64
4.1 Deposition time versus thickness of films	65
4.2 SEM cross-sectional image of DLC-10.....	67
4.3 Thickness mapping of DLC film prepared at 20 and 40 mins deposit time.....	68
4.4 Electrical resistance measurements using patterned DLC coatings on glass	69
4.5 Surface resistivity as a function of deposit time.....	70
4.6 Three-dimension: Deposition time, thickness and surface (sheet) resistivity of DLC films at 10, 20 and 30 min.....	71
4.7 Thickness ad resistivity relationship of the DLC films prepared at 20 and 40 mins deposition time.....	72
4.8 Temperature versus resistance in liquid nitrogen environment.....	73
4.9 Raman spectra of the DLC-10, DLC-20 and DLC-30.....	74
4.10 Raman spectrum of DLC-10 indicates the G and D peaks fitting.....	75
4.11 C 1s XPS spectrum taken from the DLC-10, DLC-20 and DLC	77
4.12 Deconvolution of the C1s XPS spectrum of the DLC-10, DLC-20 and DLC-30....	78
4.13 DLC films with three different coating times with normalized C K-edge XANES spectra	80

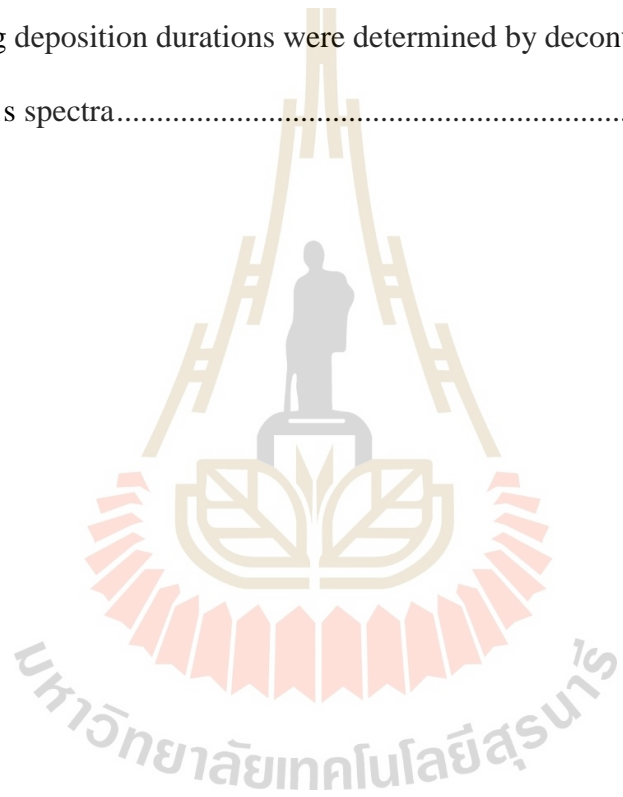
LIST OF FIGURES (Continued)

Figure	Page
4.14 DLC films' normalized C K-edge XANES spectra using curve fitting.....	81



LIST OF TABLES

Table	Page
4.1 DLC film thickness, electrical resistance, and sheet resistivity.....	70
4.2 Raman spectra fitting parameters	76
4.3 Peak positions, regions under the peak, and the $sp^3:sp^2$ ratio for DLC films with varying deposition durations were determined by deconvolution of the XPS C 1s spectra.....	79



LIST OF ABBREVIATIONS

DLC	Diamond-like Carbon
DFT	density functional theory
MPGDs	Micro Pattern Gaseous Detectors
PVD	Physical vapor deposition
HiPIMS	High power impulse magnetron sputtering
$G\Omega/m^2$	giga-ohm/sq.
Xe	Xenon
PTFE	Polytetrafluoroethylene
R_s	Sheet resistivity
ρ	resistivity
t	thickness
R	Resistance

CHAPTER I

INTRODUCTION

1.1 The Background and Applications of Diamond-like carbon (DLC)

Diamond-like carbon (DLC) films are an amorphous network made up of sp^2 (graphitic-like), sp^3 (diamond-like), and hydrogen bonds with features that are similar to diamond, such as high hardness, chemical inertness, resistivity, and low coefficient of friction. The hydrogenated amorphous carbon (a-C:H, ta-C:H) and the hydrogen free amorphous carbon (a-C, ta-C) are the two primary groups on the ternary phase diagram of material coating, as shown in figure 1.1. The hydrogen concentration, sp^3/sp^2 ratio, and deposition process factors all have a major influence on the features of these films. There are carbon atoms with (>80%) sp^3 hybridized carbon in tetrahedral amorphous carbon films (ta-C) (Charitidis et al., 2013).

Device applications based on DLC include electronics: transistors (CNT/graphene), optoelectronics: solar cells (CNT/ C_{60}), biosensors (CNT/graphene), mechanics: strain sensors (CNT/graphene), radiation detectors (graphite/diamond), and energy: Li-ion batteries (CNT/graphene), as shown in figure 1.2. As a result, the sp^2 and sp^3 hybridized carbon compounds have shown tremendous promise in electronics and sensors. The majority of carbon has good physical properties, making it ideal for electrical, optoelectronic, energy storage, and sensor development. The majority of carbon atoms in diamond and DLC are sp^3 hybridized. Density functional theory (DFT) was used to examine the transformation and electrical structures of graphene on several types of

diamond surfaces. The development of applications in sp^2/sp^3 heterostructures is based on experiments and theory studies (Yuan et al., 2019).

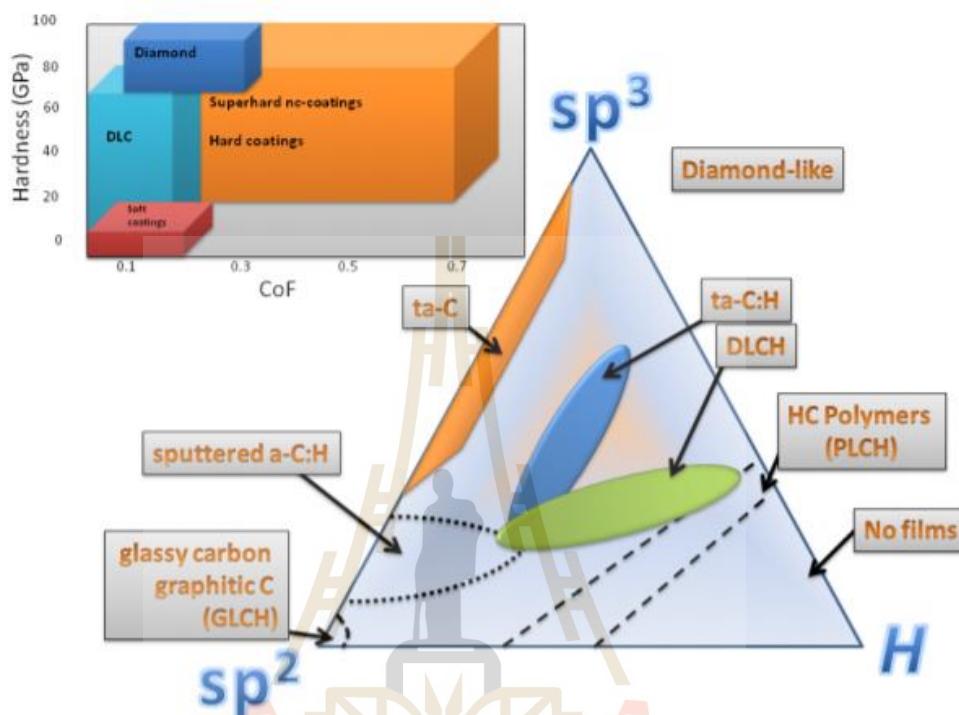


Figure 1.1 The ternary phase diagram of hardness and coefficient of friction map for various compositions of popular carbon-based materials (Charitidis et al., 2013).

Several variants of the qualities can be employed to meet the needs of various applications. Hard amorphous carbon films were initially published in the 1950s, and roughly 20 years later, intensive study on DLC began all over the world. In the ensuing years, the value of DLC for industrial applications became increasingly obvious, and the number of publications climbed steadily. To make a-C: H ta-C, several deposition processes were used. According to the Scopus database, the number of publications

progressively increased from a low point in the 1980s to a high point in the year 2000, as seen in Figure 1.3 (Bewilogua et al., 2014).

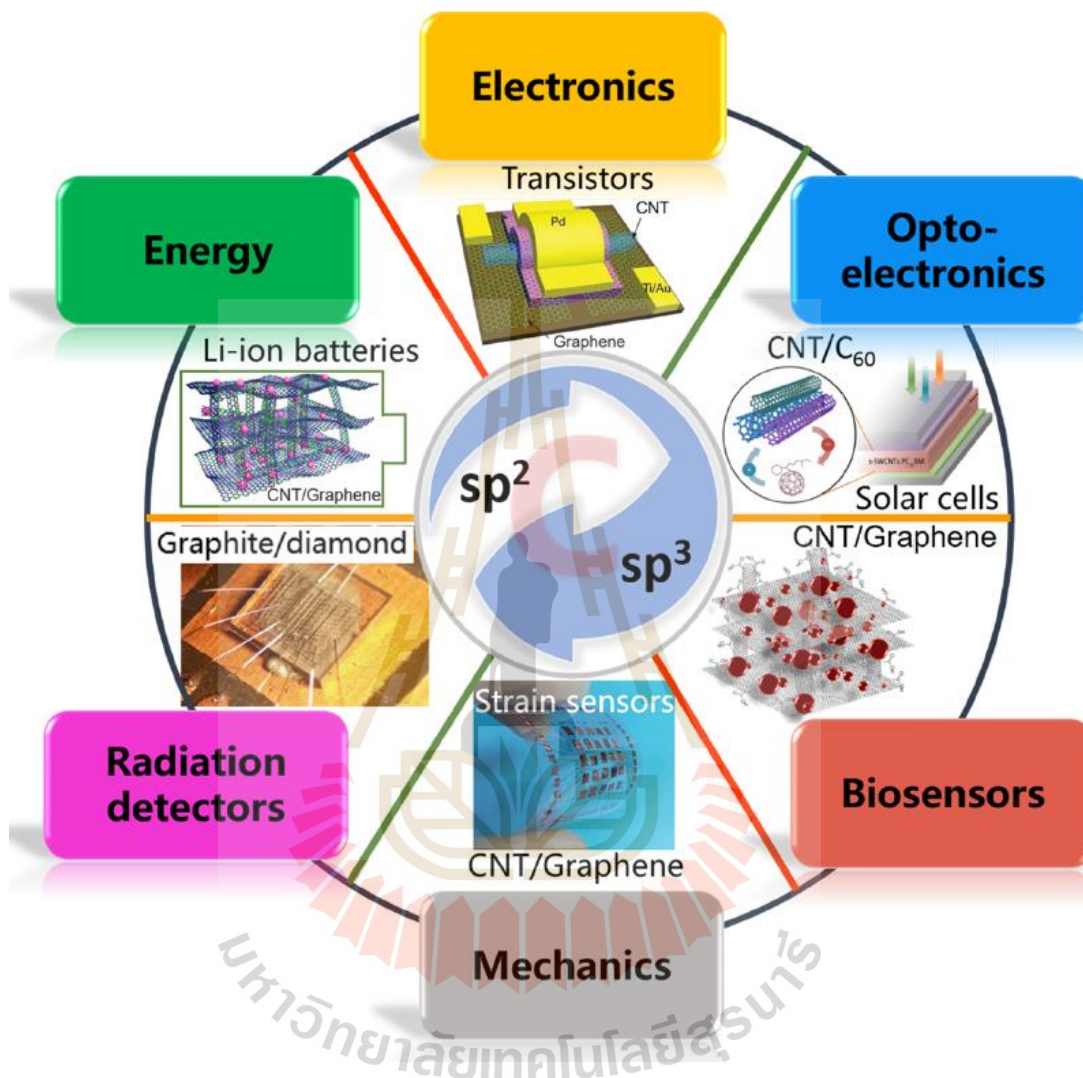


Figure 1.2 All-carbon device applications in various fields (Yuan et al., 2019).

Recently, it was revealed that resistive electrodes for Micro Pattern Gaseous Detectors (MPGDs) could be made from DLC films created using the sputtering approach. The resistivity of DLC films is determined by their thickness and deposition time (Ochi et al., 2014). The presence of a considerable amount of sp^3 hybridized carbon atoms in DLC films gives them their particular characteristics. The inclusion of hydrogen atoms can potentially change the characteristics of DLC films. The number of sp^3 specie and H atoms

in thin films is determined by the process used to prepare it. Sputter vapor deposition and arc physical vapor deposition (PVD) technologies produce DLC films without H when no H-containing gas is used. DLC films with H in the composition are always produced via plasma-enhanced chemical vapor deposition (PE-CVD) utilizing hydrogen-containing gas (Moriguchi et al., 2016). The high power impulse magnetron sputtering (HiPIMS) technique (Anders, 2017) has recently been shown to be a promising method for producing better quality of amorphous carbon films with higher hardness, higher modulus, higher homogeneity, and lower friction coefficient, than those produced by the DC magnetron sputtering (DCMS) technique (see figure 1.4). Additionally, the films could be deposited at a faster rate.

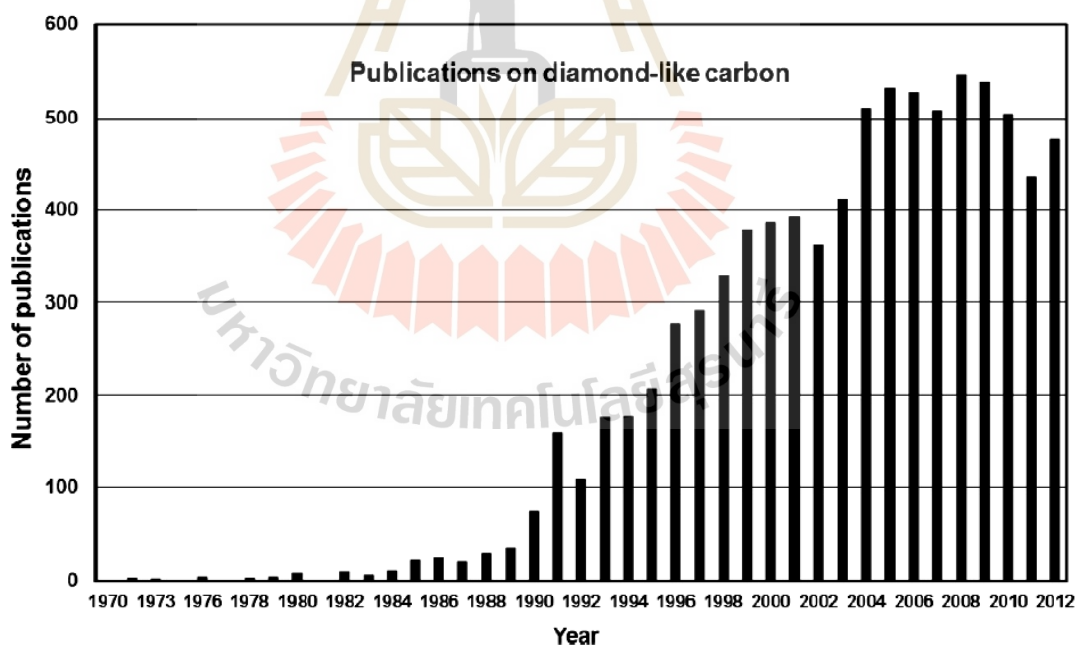


Figure 1.3 In the last four decades, the number of papers on diamond-like carbon coatings has increased dramatically (data from Scopus database for all DLC modifications) (Bewilogua et al., 2014).

When nanostructured materials are utilized as electrodes, they can achieve high energy densities at high rates, which can be substantially improved if the right nanostructured materials are used. They divided them into four categories: 0-D, which includes core–shell nanoparticles, nanospheres, and their composites, 1-D, which includes carbon nanotubes and nanowire arrays, 2-D including graphene based composites and carbon coated nanobelts, and 3-D nanostructures, as shown in figure 1.5 (Panda et al., 2019).

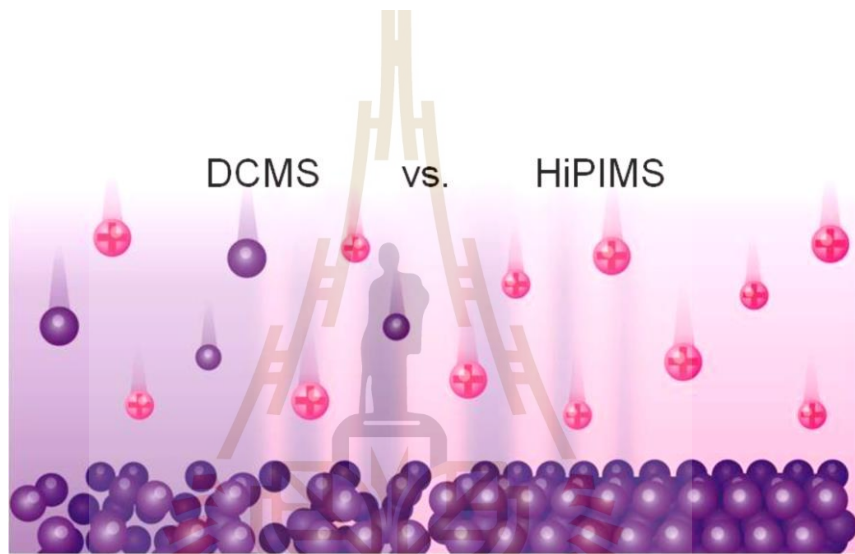


Figure 1.4 Comparing DCMS versus HiPIMS deposition technique (https://www.sintef.no/contentassets/e136731e6d2144e9a7cb38ac947151a3/fasolin-stefano_ampea-workshop.pdf).

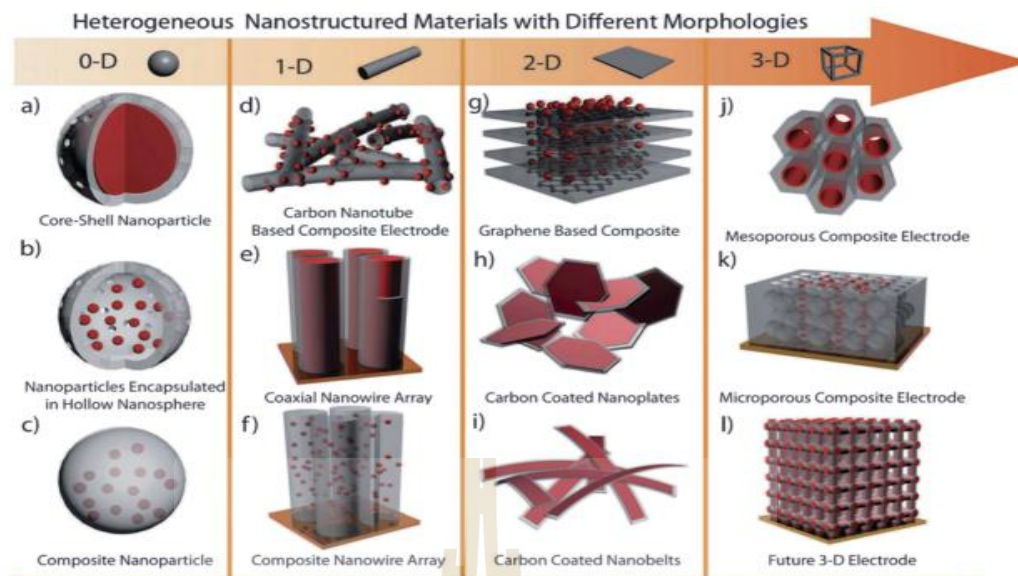


Figure 1.5 Different heterogeneous materials are depicted schematically based on structural complexity (Panda et al., 2019).

1.2 Research objectives

- a) To obtain experiences with high power impulse magnetron sputtering (HiPIMS) technique for preparing diamond-like carbon (DLC) films.
- b) To investigate the feasibility to apply the DLC films in detectors for elementary particle detection.

1.3 Scope and limitation of the study

The goal of this study is to look at DLC films made using the HiPIMS technology. The properties of DLC films were investigated using the HiPIMS technology and electrical property measurements. We're looking at DLC films that could be utilized as a large-area resistive surface for electrodes in nuclear and particle physics detectors, which necessitates resistivity in the $G/sq.$ region. The HiPIMS technique was used to test the characteristics of DLC films. In addition to the electrical properties of the DLC films being measured.

CHAPTER II

LITERATURE REVIEWS

In this chapter, the promising properties of DLC, techniques used to prepare DLC films will be discussed. The High Power Impulse Magnetron Sputtering (HiPIMS) system for preparing DLC in the PandaX-III detector application will also be explained.

2.1 The diamond-like carbon (DLC) films

DLC is known to have distinct properties covering higher hardness, low friction coefficients, chemical inertness, wear resistance, optical transparency in the IR spectral range, and low electrical conductivities. The following types of DLC coatings were identified: firstly, the H-free amorphous carbon films or a-C, the H-free tetrahedral amorphous carbon films or ta-C with a high fraction of tetrahedral coordinated sp^3 bonded carbon atoms, and the hydrogenated and tetrahedral amorphous carbon films (a-C:H and ta-C:H), respectively. There is also the modified hydrogenated amorphous carbon films (a-C:H:X), where X can be the non-metal elements such as silicon, oxygen and nitrogen.

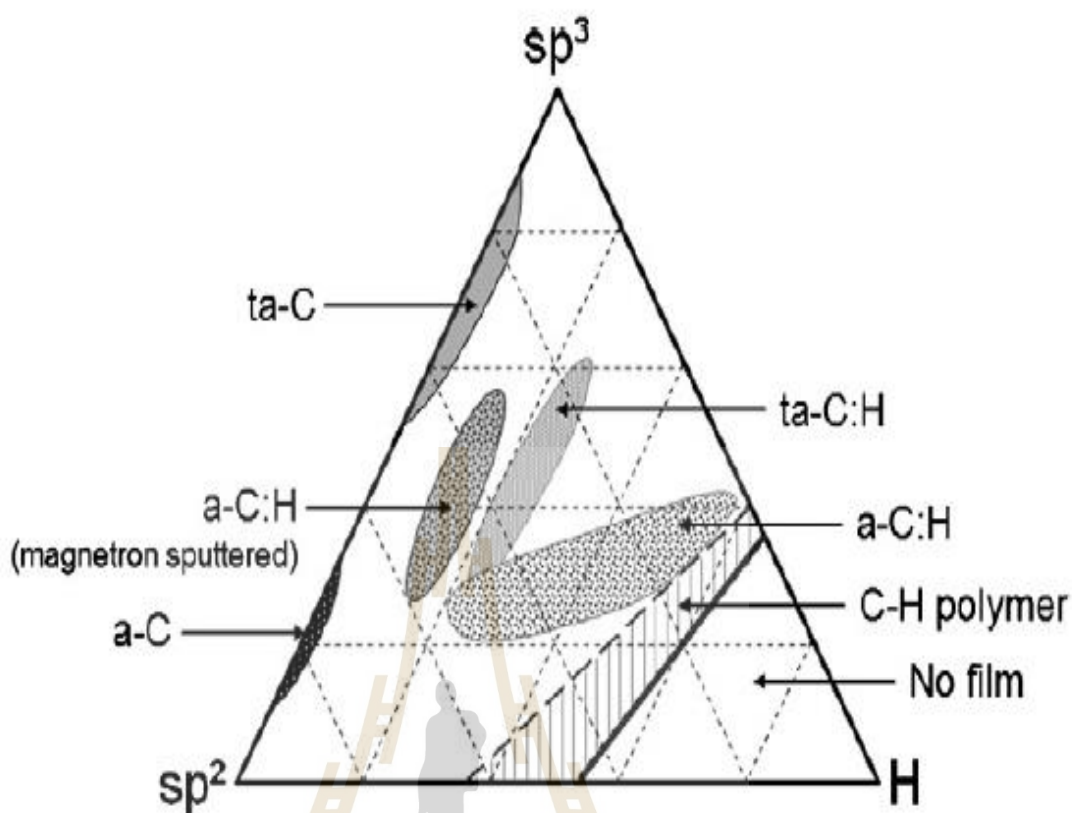


Figure 2.1 Amorphous and nanocrystalline carbon sheets in a ternary phase diagram (Bewilogua et al., 2014).

For PVD, there are two methods: 1) arc (ta-C creates hardness near the diamond low friction in oil but is difficult to create thick coatings and sensitive to surface condition) and 2) sputter ta-C supports conductive DLC Low hardness). a-C:H to ta-C, or semiconductor-insulator, are DLC films having electrical properties in the low-high resistivity range. As demonstrated in figure 2.1 and 2.2, the R of a-C:H and ta-C films is $10^4 - 10^{12} \Omega/\text{cm}$ and $10^6 - 10^{10} \Omega/\text{cm}$, respectively (Bewilogua et al., 2014). As a result, DLC is a semiconductor.

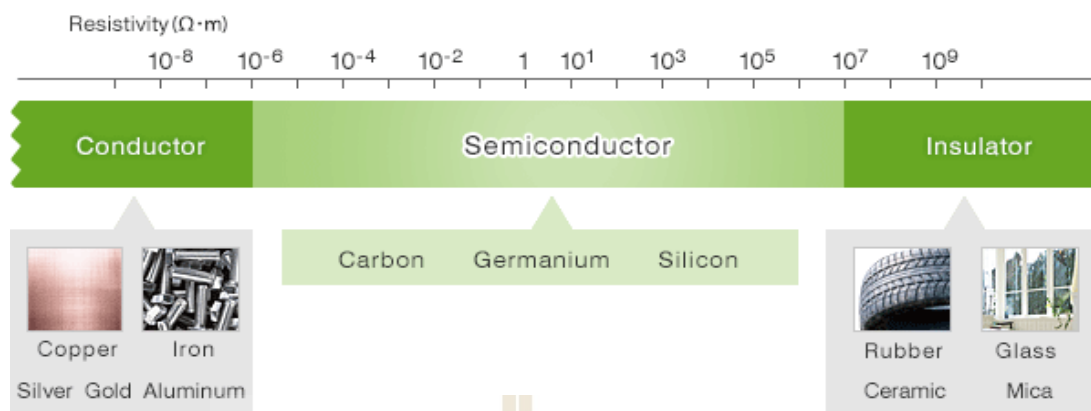


Figure 2.2 Electrical resistivity of materials (<https://www.hitachi-hightech.com/global/products/device/semiconductor/properties.html>).

Figure 2.3 (a) depicts an a-C:H film model with a dominant the share of sp^2 specie and a H content of 30%. The computer modelling of pure amorphous carbon or both pure and hydrogenated amorphous carbon by several reports in the 1990s. The results have been compared to the experiments in means of mass densities, H contents, interference functions, and radial distribution functions. The best points of agreement between experiment and computational calculation may be utilized to make inferences about the contributions of sp^3 , sp^2 , and sp^1 bonds (one-dimensional carbon such as acetylene-like), and electronic densities of states could be calculated (Bewilogua et al., 2014).

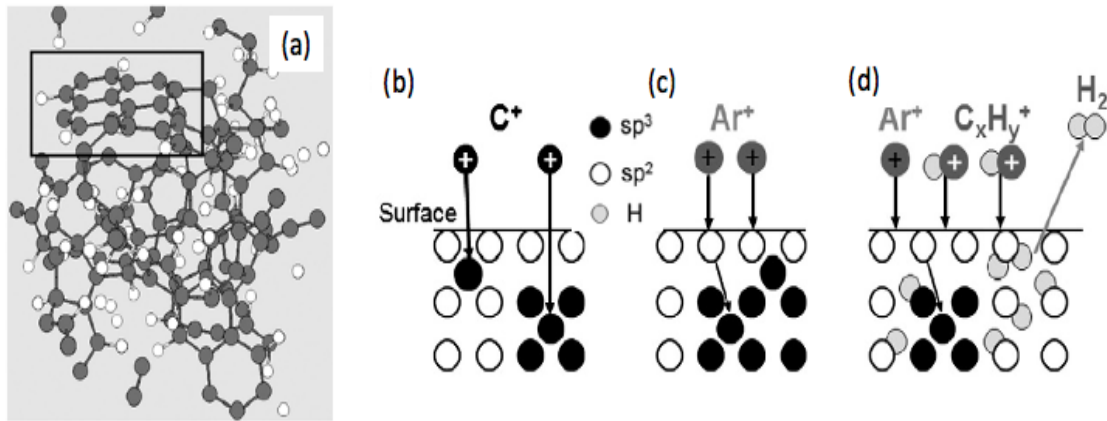


Figure 2.3 a) An a-C: H film having a density of 1.7 g/cm³, 30% hydrogen, 65 percent sp², 20 percent sp³, and 15 percent sp¹ bonds has a structure model. Interactions between ions and films during the formation of ta-C and a-C:H: b) direct and indirect sub-plantations, c) a-C:H growth scheme, d) a-C:H growth scheme (Bewilogua et al., 2014).

In a continuous paper, Robertson established and extended a similar concept with the model of film growing to plasma deposited a-C:H films. Ions will be densified as they enter the subterranean region. The experimentally results determined density maxima of the ta-C film were understood as the result of densification due to the ion impacting the surface and, at higher energies, energy dissipation accompanied by annealing and density decline. Figure 2.3(b)-(d) show how ions can have a direct (carbon ion) or indirect (known as surface displacement of atoms into an interstitial location) impact on the surface. (Bewilogua et al., 2014).

2.1.1 Physical properties of DLC films

Thin layer coatings having an amorphous structure are known as DLC coatings. As illustrated in figure 2.4(a), the overall structure of non-crystalline from DLC carbon incorporates both diamond (sp³ bonded carbon production) and graphite (sp² bonded carbon formation). The ratio between the production of sp³ and sp² percent

hydrogen by the composition and structure of metal and other material inside percent determines the physical properties (such as material) of the DLC coating. Figure 2.4(b) shows the amorphous carbon end-stage diagram presented by Ferrari and Robertson to explain the conceptual structure of DLCs (Ferrari et al., 2000).

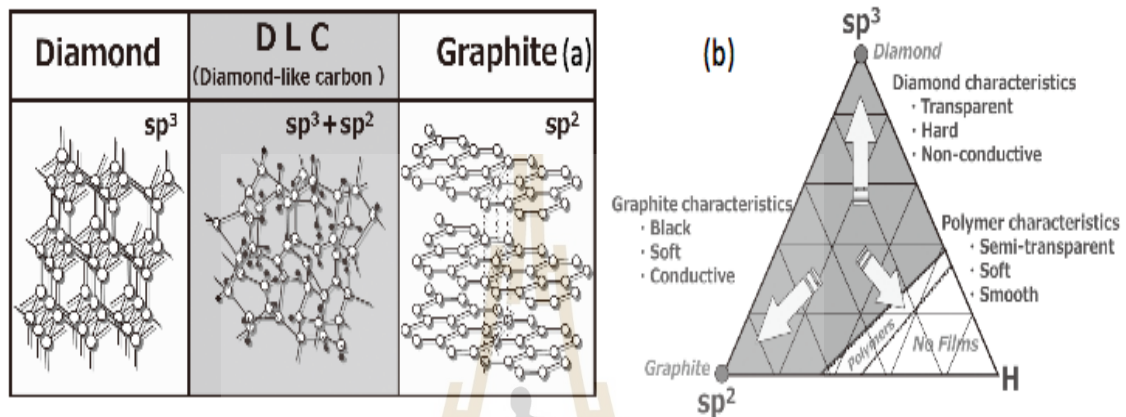


Figure 2.4 a) Structural comparison of diamond, DLC and graphite. b) Characteristic diagram of DLC (Tanaka et al., 2019).

Depending on the ratio of sp^3 and sp^2 production, hydrogen-free DLC can be classified as ta-C or a-C. Because a high degree of stiffness is needed for industrial application, ta-C is frequently employed in DLC coatings. The ta-C DLC coating is promising in reducing the friction coefficients in oil, in addition to its high hardness and thermal durability. As a result, the ta-C DLC coating is regarded as one of the most effective surface treatment solutions for objects that come into contact with engine lubricants. The ta-C: H and the ta-C: H can also be used. In the absence of lubrication, hydrogenated DLC has the capability to drastically decrease the friction factor. The proper DLC coating structure for the target product must be determined and designed based on these features. (Tanaka et al., 2019).

2.1.2 Thermal properties of graphene

Carbon compounds, which appear in a range of allotropes, hold a unique position in terms of thermal properties, as shown in Figure 2.5(a). The thermal conductivity of different carbon allotropes spans more than five size orders, ranging from less than 0.01 W mK⁻¹ in amorphous carbon to more than 2000 W mK⁻¹ in diamonds or graphene at ambient temperature. At 77 K, type-II diamonds have a thermal conductivity of 10,000 W mK⁻¹. At room temperature, carbon nanotubes (CNTs) exhibit a thermal conductivity of 3,000-3,500 W mK⁻¹, which is higher than that of diamond, the best bulk thermal conductor.

The K values of the high-purity, diamond (sp² and sp³), and amorphous carbon are shown in Figure 2.5(b). These graphs are considered on the published recommended values, which were compiled and analyzed from hundreds of investigations using conventionally recognized experimental data (Balandin, 2011).

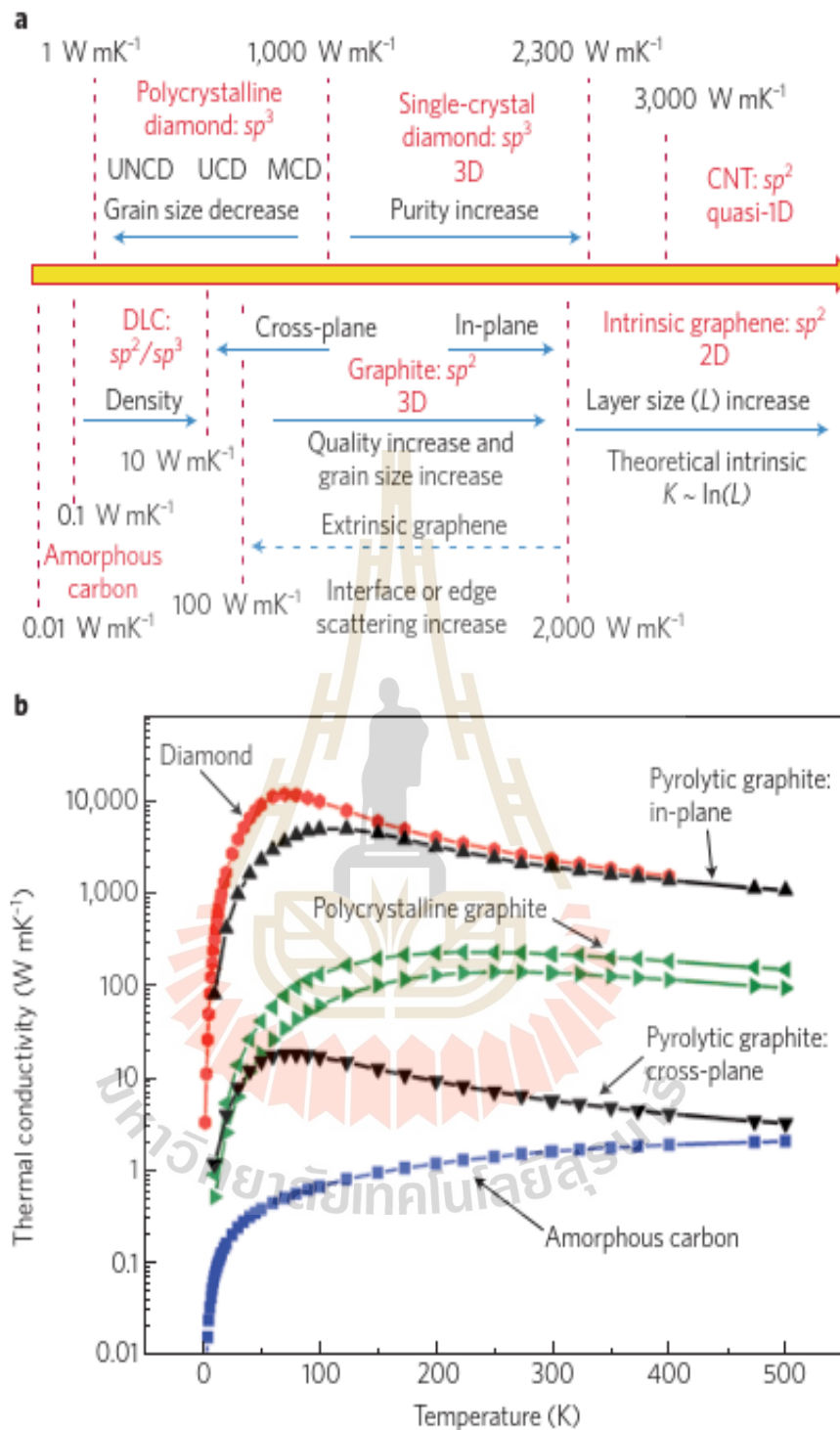


Figure 2.5 Carbon allotropes and their derivatives have different thermal characteristics.

a) Diagram based on literature-reported mean values. b) The thermal conductivity of a variety of carbon allotropes as a function of temperature (Balandin, 2011).

In this approach of atoms at both ends, Figure 2.6(a) depicts one of the imbalanced molecular dynamics methods which are widely employed to explore thermal transport in graphene known as GNRs. The sides are kept, while the hot and cold zones within a few nanometers are evaluated. By finding the thermal boundary conditions or constant temperature in hot and cold regions, a constant temperature gradient is enforced within the graphene sheet, which is then used to evaluate the material's thermal conductivity. MD simulations have shown how heat may be regulated or varied in comparison to pure graphene by integrating atomic alterations to the honeycomb structure. Vacancies or Stone-Wales defects, grain boundaries, tension, chemical function, isotope impurities (^{13}C) or replacement defects, and roughness of edges or folds in GNRs all cause such alterations, as seen in figure 2.6(b).

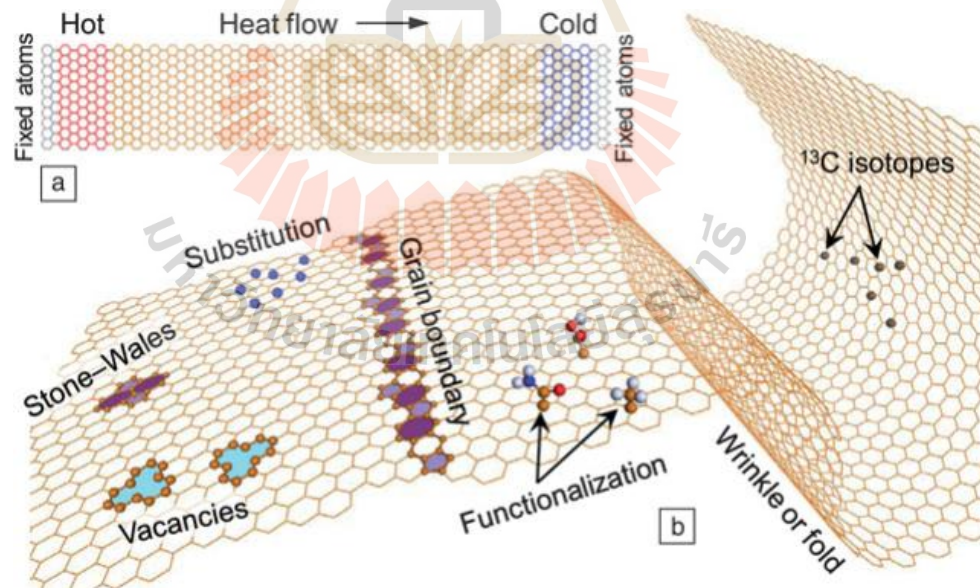


Figure 2.6 (a) The use of nonequilibrium molecular dynamics (NEMD) to investigate thermal transport in GNR is depicted in this diagram. (b) GNR representations of several fault types (Pop et al., 2012).

Reducing the inter-layer spacing (ILD) and raising the inter-layer spacing (ILD) can, for example, lower the graphene piles' weak thermal inter-layer connections, resulting in increased cross-plane thermal conductivity. Longer IJDs and shorter ILDs, when combined, can reduce heat conductivity between planes, resulting in insulation or thermoelectric applications. Figure 2.7 depicts a new generation of nanomaterials that combine the best properties of graphene and carbon nanotube architectures to provide variable thermal mechanical activity. It can be used in a variety of applications, including efficient fuel cell electrodes, large- surface-area nanostructures for hydrogen storage, supercapacitors, and customizable multidimensional heat carrier materials (Pop et al., 2012).

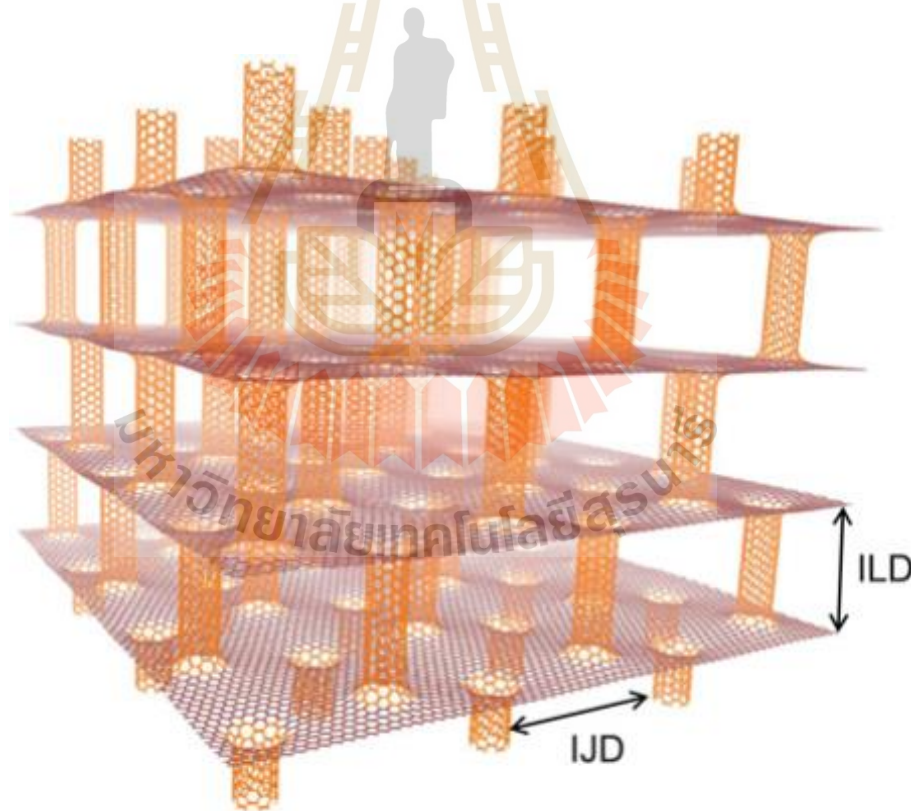


Figure 2.7 A three- dimensional nanotube architecture that combines poles, carbon nanotubes, and graphene sheets to produce tunable cross-plane heat transmission is shown in this schematic diagram (Pop et al., 2012).

The construction of the vacancy defect and functional group on the onion-like carbon (OLC) supporter is a vital step in stabilizing the isolated metal atoms to produce this clever catalyst design (figure 2.8(a)). A high-angle ring-through dark channel transmission electron microscopy (HAADF-STEM) has been utilized to determine the pattern of platinum (Pt) atoms distributed on an OLC-compatible device, as shown in figure 2.8(b). Isolated Pt atoms (named Pt₁/OLC) were discovered using a high-angle ring-through dark channel transmission electron microscope (HAADF-STEM). After surface-oxidized detonation nanodiamond (DND) fusion oxidized at 1,500 °C, a typical multi-shell fullerene structure with a 5 nm in diameter and a layer spacing of 0.35 nm was seen as OLC particles across the support line with no clear nanoparticles or clusters at the same time as shown in figure 2.8(c) (Liu et al., 2019).

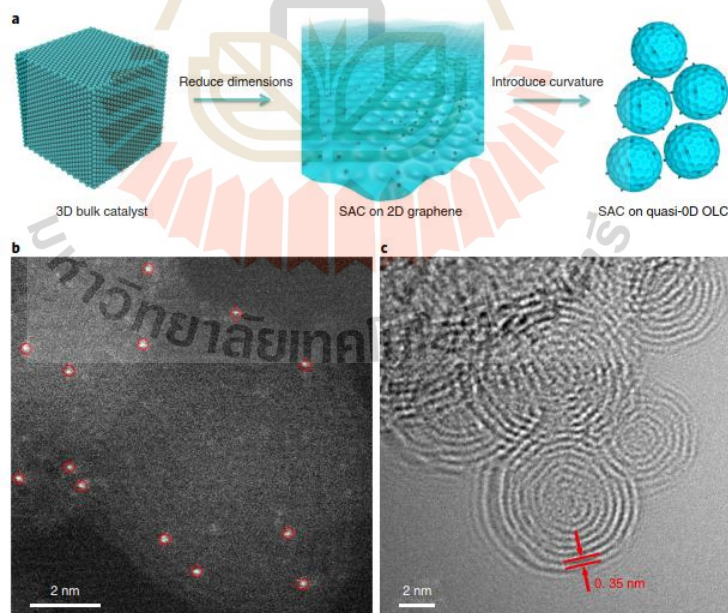


Figure 2.8 Rational design of the Pt₁/OLC catalyst undergoes a reduction in size and introduces curvature (Liu et al., 2019).

2.2 DLC films deposition techniques

There are two types of DLC film production methods: Physical Vapor Deposition (PVD) and Chemical Vapor Deposition (CVD). PVD employs solids (graphite) as a carbon source, while CVD uses gas (hydrocarbons like methane). PVD is separated into two types: sputtering arc deposition and vapor laser deposition. Radio frequency (RF), direct current (DC), Penning ionization meter (PIG), and self-discharge technologies are all used in CVD. We've been using RF discharge plasma CVD, PIG plasma CVD, and arc PVD, as shown in Figure 2.9 (MORIGUCHI et al, 2016).

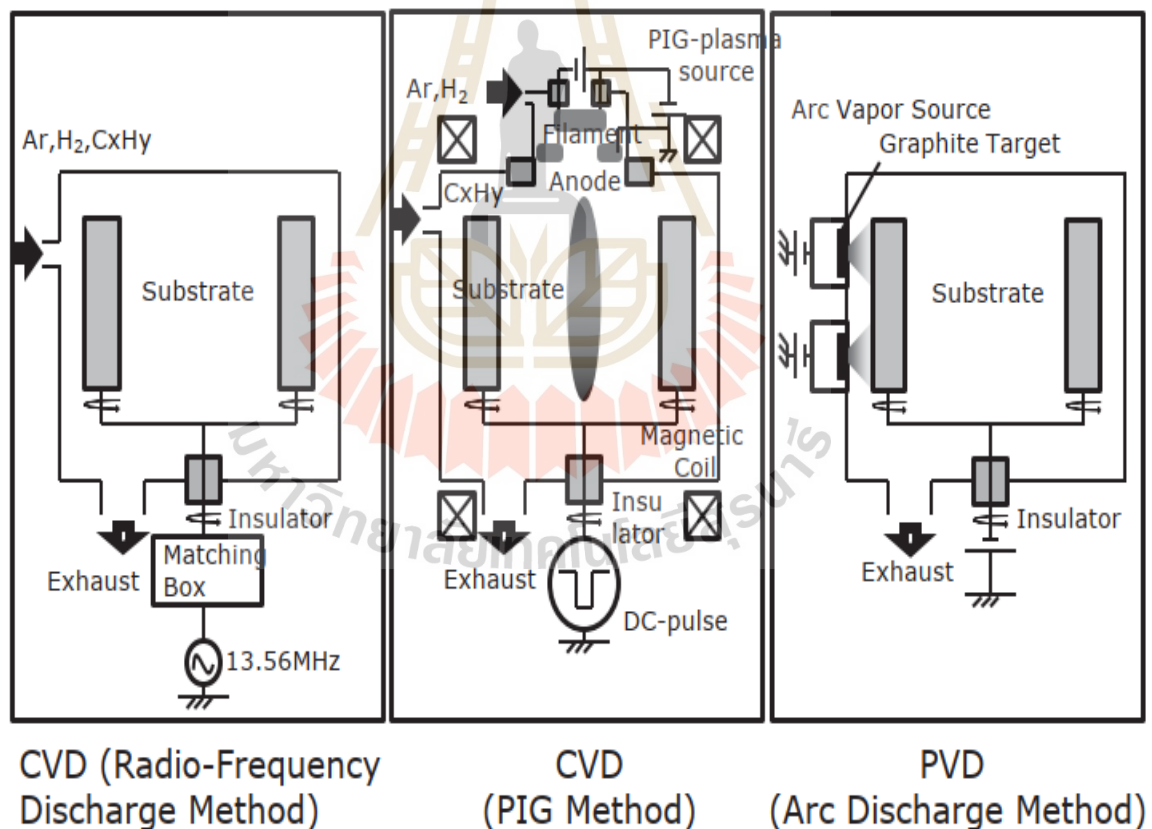


Figure 2.9 Typical DLC Production Process (MORIGUCHI et al., 2016).

2.2.1 Direct current (DC) technique

A totally Direct current (DC) coating was developed in the Weissmantel a-C:H group after an "ion plating" technique in which hydrocarbon ions were formed in the benzene atmosphere by hot cathode ionization, a-C:H film. Accelerating these ions to a negative DC causes it to expand. The substrate has a bias to it (up to 800 V). This deposition process is depicted in Figure 2.10. Stiff, somewhat transparent, and electrically insulating, these films are used in a variety of applications. The structure is described as a nanocrystalline combination of graphite-like and diamond-like elements (Bewilogua et al, 2014).

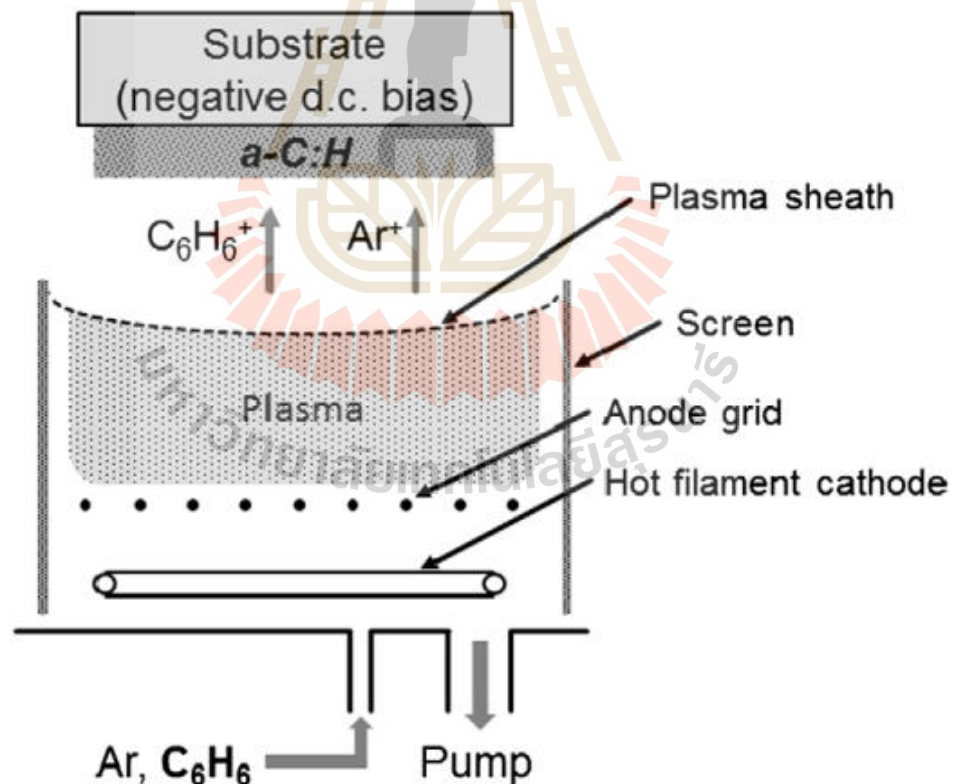


Figure 2.10 Scheme of DC ion plating deposition system (Bewilogua et al., 2014).

2.2.2 Radio frequency (RF) technique

A self-built RF PECVD apparatus is used to deposit the DLC films. Figure 2.11 depicts the device schematic. The DC bias voltage in the front panel of the magnetron cathode is replaced by a magnetic field which can be applied to the RF PECVD plane cathode. The E and B fields produce E & B electron floatation. In addition, secondary electrons generated by ion bombardment are limited to the area of the cathode, resulting in the increase of plasma density (Huang et al., 2012).

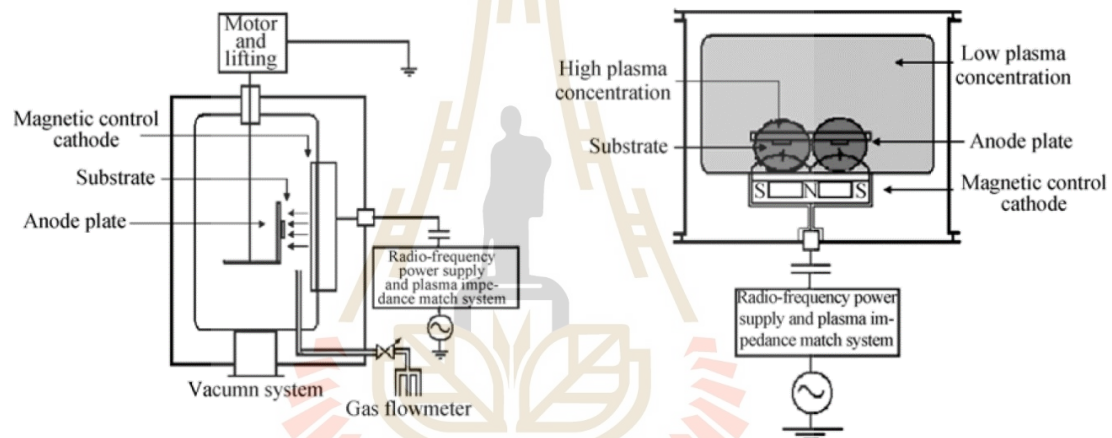


Figure 2.11 The radio frequency magnetron PECVD deposition device is seen in a schematic diagram. (Huang et al., 2012).

During accumulation, a methane + argon premix was ruptured by RF plasma power of 13.56 MHz; 100 W at constant chamber pressure (0.215 mbar) to deposit nickel nanocrystalline in the thin-film DLC composite. The plasma was created between two aluminum (Al) discs (2.54 cm in diameter). Figure 2.12 illustrates a drawing of a radio-assisted plasma vapor deposition system (R. Paul et al., 2012).

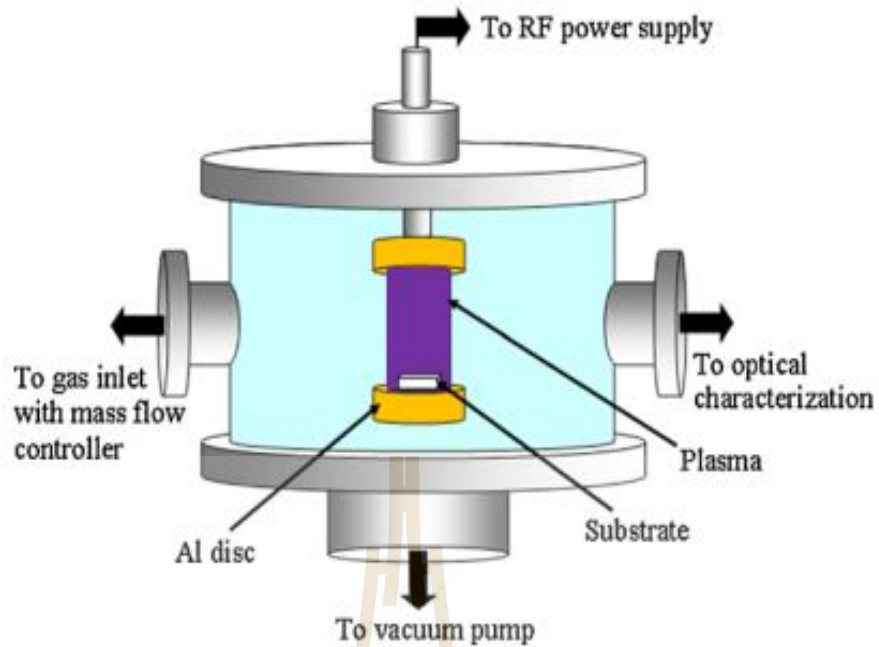


Figure 2.12 Schematic of RF capacitively coupled plasma (CCP) chemical vapour deposition system (Cheng et al., 2010).

Some scientists have reported results of a-C: H accumulation investigations since mid- 1970s; however, the Holland and Ojha work, in particular, can be deemed damaging due to their use of radio frequency (rf - 13.56 MHz) fluorescence emission. To address problems with insulating film a-C: H deposition in butane gas (C_4H_{10}) (for method - form see figure 2.13) (Bewilogua et al., 2014).

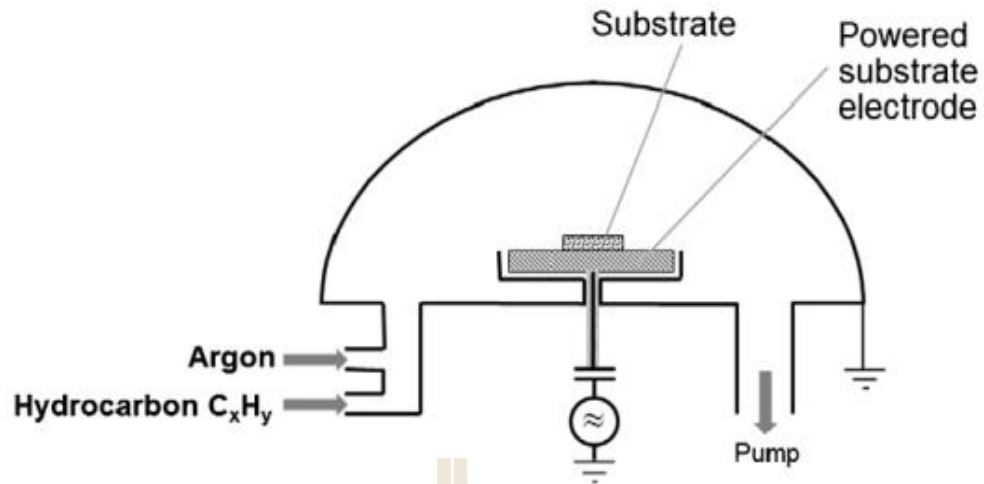


Figure 2.13 Scheme of RF glow discharge deposition system (Bewilogua et al., 2014).

2.2.3 High power impulse magnetron sputtering (HiPIMS)

Figure 2.14, High Power Impulse Magnetron Sputtering (HiPIMS) is a state-of-the-art in sputtering technique cooperating between Magnetron Sputtering (MS) equipped with a high voltage (HV) pulsed power source in order to the physical vapor deposit to coat the thin films. HiPIMS creates a high-density plasma by focusing HV, the target coating material was burst within brief duration, resulting in a high degree of ionization in the form of plasma of the coating material.

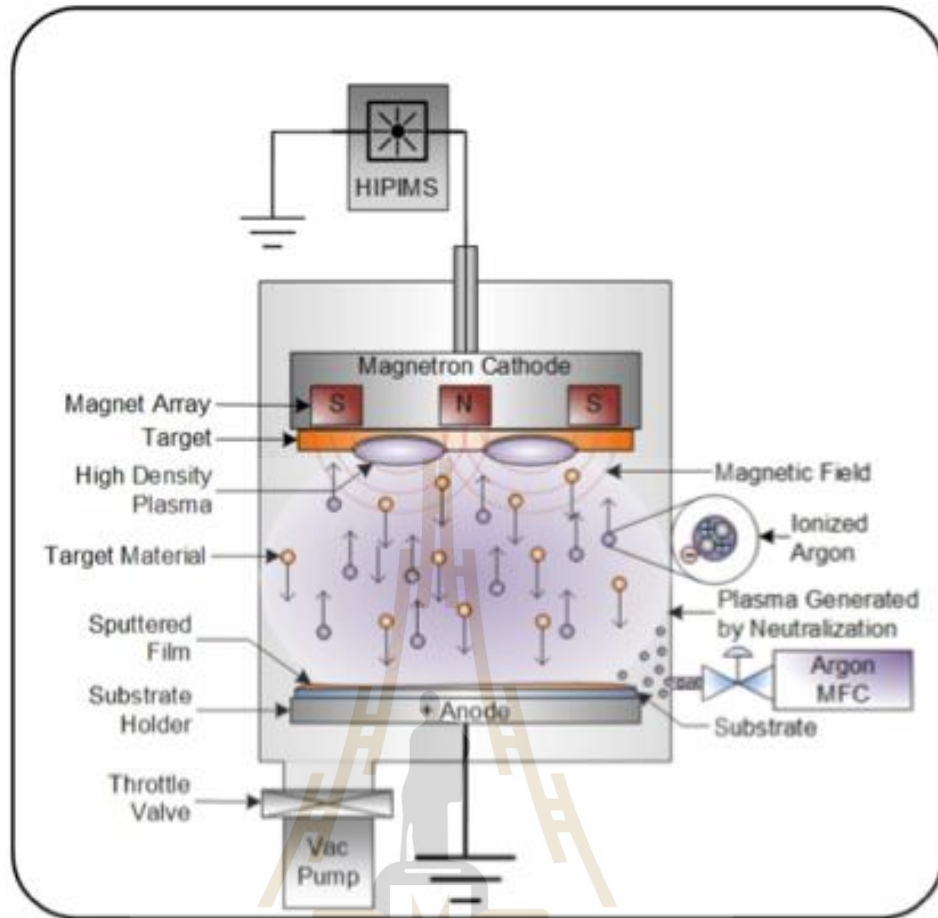


Figure 2.14 Diagram of the HiPIMS Process (<http://www.semicore.com/news/93-what-is-hipims>).

A large fraction of the sputtered target material can be ionized in the plasma cloud by pulsing the target coating material with bursts of high voltage energy - with a length of 100 seconds on the order of kW/cm² but a relatively short duration or "Duty time" of less than 10% - without overheating the target and other system components. The target has a chance to cool during the majority of "Off duty" time, resulting in a low average cathode power of 1-10 kW, which enhances process stability.

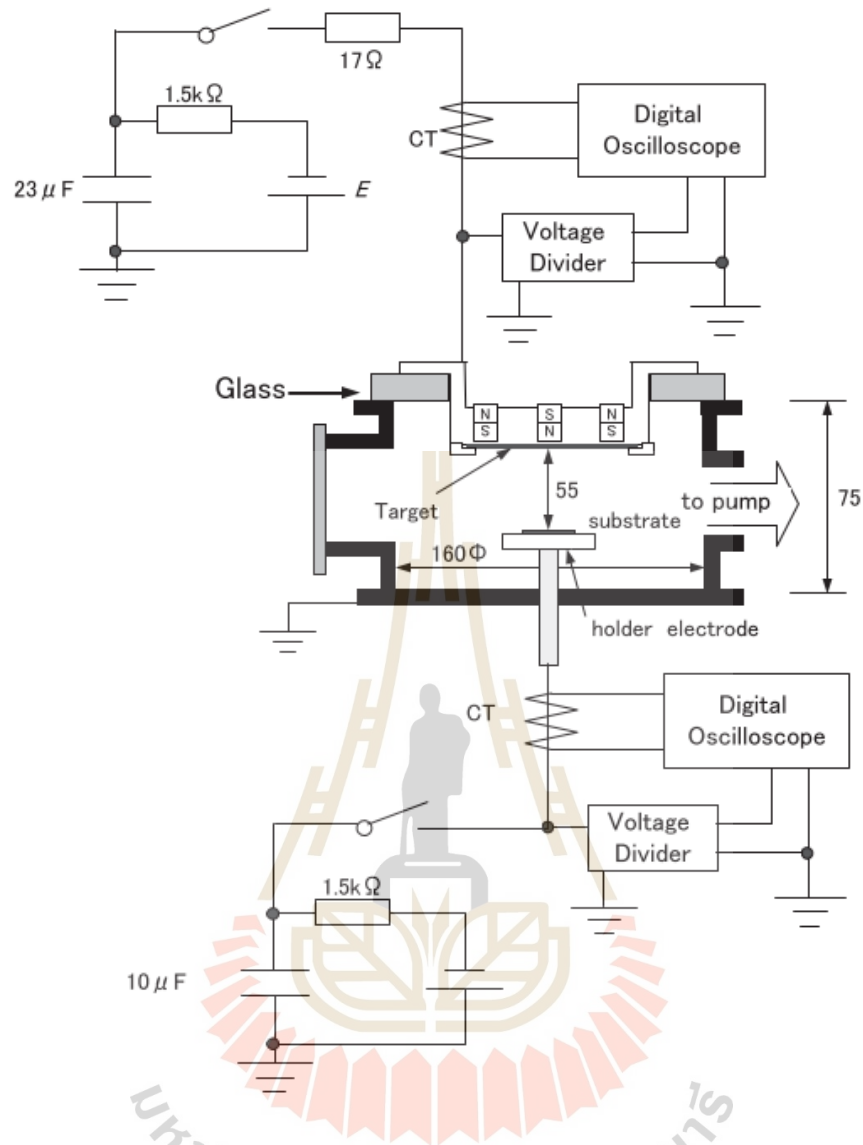


Figure 2.15 Schematic diagram of experimental apparatus (Kimura et al., 2016).

A carbon target with $80 \text{ mm} \times 2 \text{ mm}$ (diameter \times thickness) is positioned at the top of the vacuum chamber through glass with 10 mm thickness, and a field magnet is formed, as illustrated in figure 2.15. The mean parallel element of magnetic induction at the erosion rail, examined at a point 2-3 mm below the target surface using a set of permanent magnets positioned 2 mm behind the target, was around 0.05 T in the region. Among the workpiece and the chamber with $160 \text{ mm} \times 75 \text{ mm}$ (diameter \times height), pulsed voltage is supplied to close the target surface. The pulsed voltage source for HiPIMS is

made up of a DC voltage source with a maximum output of 2 kV, a resistor, a capacitor (= 23 F), a high voltage insulated bipolar transistor (IGBT) switch, and a distance between the workpiece and the substrate. The combination of the Ar and CH₄ flow rates was controlled at roughly 20 sccm over a total pressure range of 0.3 to 2 Pa. The target voltage was adjusted to repeat at around 110 Hz, with 0.55 J of energy provided each pulse width of 40-50 s. The current transformer senses the waveform of the emitted current and divides the goal voltage. A digital oscilloscope set to 1/1000th of a second is used to monitor a voltage divider. (Kimura et al., 2016).

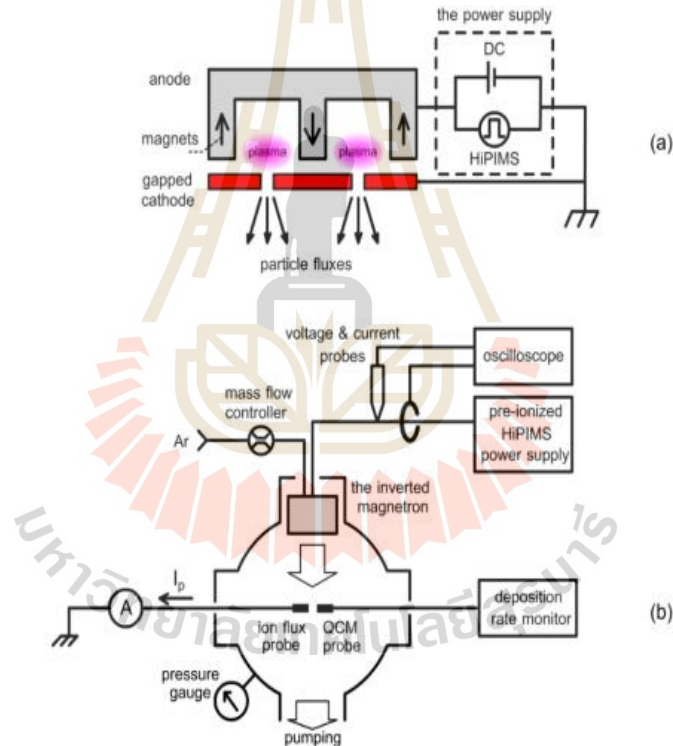


Figure 2.16 Schematic diagram of (a) the inverted magnetron and (b) experimental arrangements.

The inverted magnetron's structure has been described previously. Figure 2.16(a), on the other hand, shows a schematic layout of the magnetron setup used in the

current study. A gap nickel cathode and a grade 410 stainless steel anode are used in most magnetrons. The positive electrode is grounded, whereas the anode is biased to a positive voltage. The center disk and the ring are the two concentric components of a blank nickel cathode. The center disk has a diameter of about 31 mm, while the inner and outer diameters of the ring target are 37 mm and 70 mm, respectively. Both the center disk and the ring have a thickness of about 6 mm. A complete circular gap with a width of 3 mm was formed using this targeting arrangement; it is vital to notice that the central disk is supported by the target holder supporting the magnetron's axis. For clarity, the central disk holder is not depicted in figure 2.16(b). Electrons are trapped at the cathode gap by a magnetic field created by permanent magnets placed in the anode. As a result, plasma can form around the cathode gap, allowing the cathode material to be sputtered.

2.2.4 Ion deposition technique

Aisenberg and Chabot published the next major paper on solid amorphous carbon, which coined the name "diamond-like carbon" at the time. Ion-beam deposition techniques were used to create these coatings on a room-temperature surface. The ion beam is made up of carbon ion and argon ion produced in a vent system with graphite as the active electrode material. The device's outline is depicted in figure 2.17(a). Positive carbon ions and gases are collected from the emission zone and deposited on a negatively biased surface, with the ion energy adjustable based on the reactant potential. Scratch resistance, electrical insulation, transparency, and chemical resistance are all tested on the films that are deposited. The structure has been described as a partial crystal with a diamond-like lattice constant. Also described was the fabrication of a thin transistor utilizing an insulating carbon layer. The cutting effectiveness of paper cutting blades might be greatly increased by employing a diamond-like carbon layer, according to the same

author in 1973. These films "reduced the coefficient of friction," according to a wear test using coated blades.

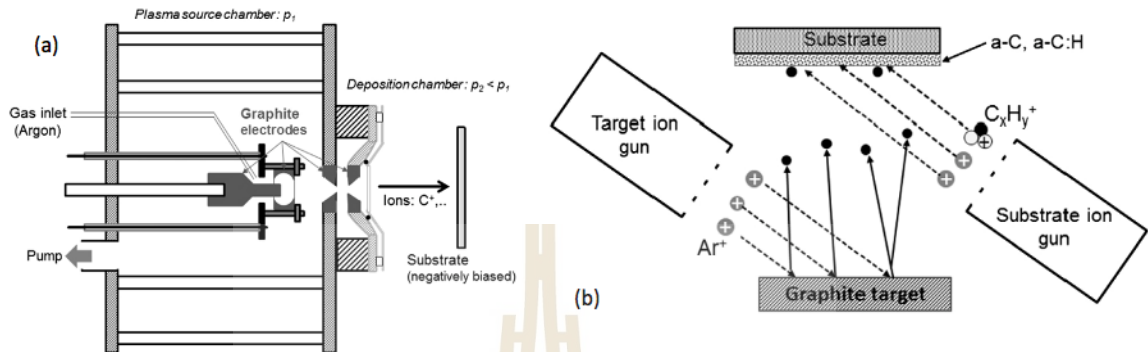


Figure 2.17 a) Scheme of ion-beam deposition technique. B) Scheme of dual beam deposition system (Bewilogua et al., 2014).

Other approaches for a-C:H collecting and detailed films have been developed since the mid-1970s. Weissmantel and colleagues describe two methods for producing DLC coatings using a double beam process, in which the carbon target is sprayed with ions of argon and the films of carbon forming on the surface is assaulted by a second ion source activated by about 1 kV of the gas mixture of argon and methane (figure 2.17(b)). The collected carbon sheet is stiff and amorphous, with crystals imbedded in the surface region with the highest ion current density (Bewilogua et al., 2014).

2.2.5 Pulsed laser deposition technique (PLD)

A PLD technique is used to create carbon thin films on various substrates. A KrF Excimer laser with a 248 nm emission wavelength and a frequency of 20 hertz was used to evaporate graphite. Using the mean spot size, the laser fluency was calculated to be 3.3 J/cm². The turbo molecular pump's vacuum chamber is ejected to achieve a vacuum

pressure of 3×10^{-7} Torr. During deposition, Ar is employed as a background gas at pressures ranging from 1 - 800 mTorr. The Silicon [100] substrate is used to deposit a thin carbon coating on single crystal intrinsic silicon, which has been ultrasonically cleaned before deposition. The revolving graphite surface positioned on the target within the vacuum chamber is the focus of the pulsed laser beam. For thin film deposition, at a distance of 4 cm from the target, the substrate is put in front of the coated plasma plume. The experimental setup is depicted schematically in Figure 2.18. (Usman et al., 2016).

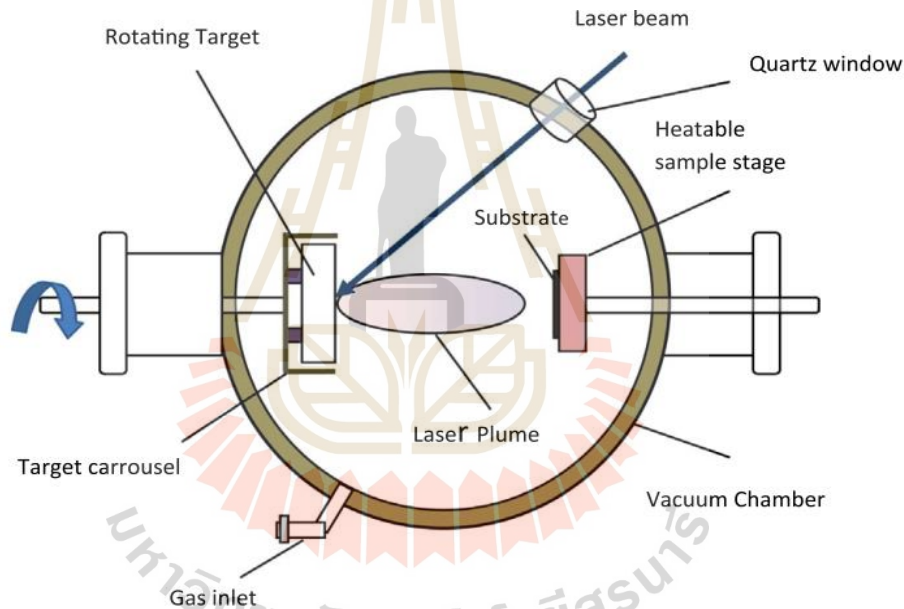


Figure 2.18 Schematic diagram of PLD technique (Usman et al., 2016).

2.3 Related properties of DLC films

2.3.1 Uniform electron gas

The correlation function is based on three correlation conditions. The Perdew, Burke, and Ernzerhof (PBE) correlation is used to create our function theoretically. The $H(r_s, t)$ function is used by PBE to uniformly raise the correlation energy of a gas electron. Instead, the multiplicative $S(r_s, t)$ function is suggested. As a result, the mathematical pattern is unique. The two functions' responses to the gradient t parameter are shown in Figure 2.19. It's worth noting that the two functions have the same asymptotic properties. Rather, it functions consistently in the medium, particularly as the electron density rises. Therefore, it is assumed that the success of our relationship works with its behaviour in the middle region (Chachiyo et al., 2020).

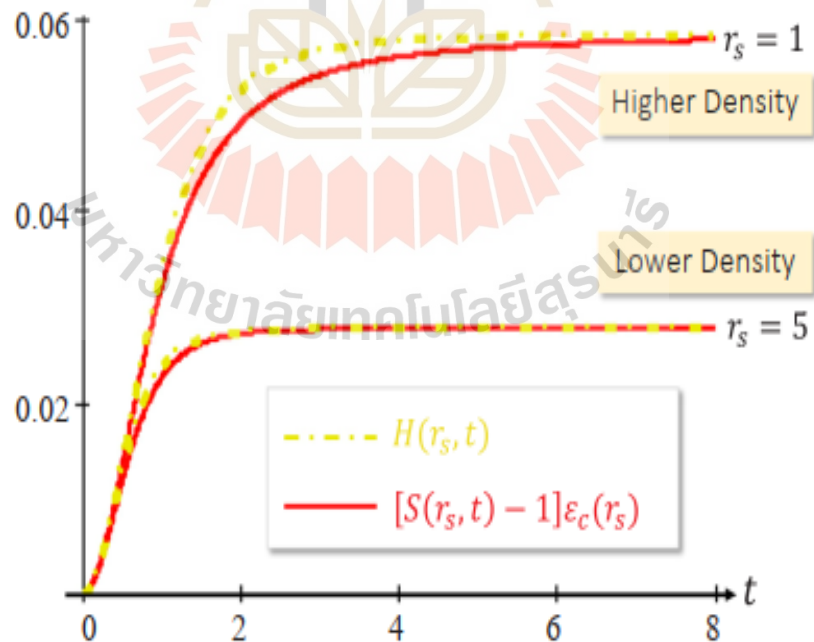


Figure 2.19 Comparison between the $H(r_s, t)$ from the PBE correlation and $[S(r_s, t) - 1]\epsilon_c(r_s)$ for two different electron densities (Chachiyo et al., 2020).

2.3.2 Hall effect

The direction of rotation has become the focus of condensed matter physics thanks to a huge spin-textured band material anticipated by theory and confirmed in experiments over the years. The rotation of the direction of rotation considerably separates the orbital structure with an energy level one magnitude higher than traditional seminal splitting in this novel family of quantum materials, resulting in changes. Many physical features result in a plethora of hitherto unseen phenomena (figure 2.20) (Liao et al., 2020).

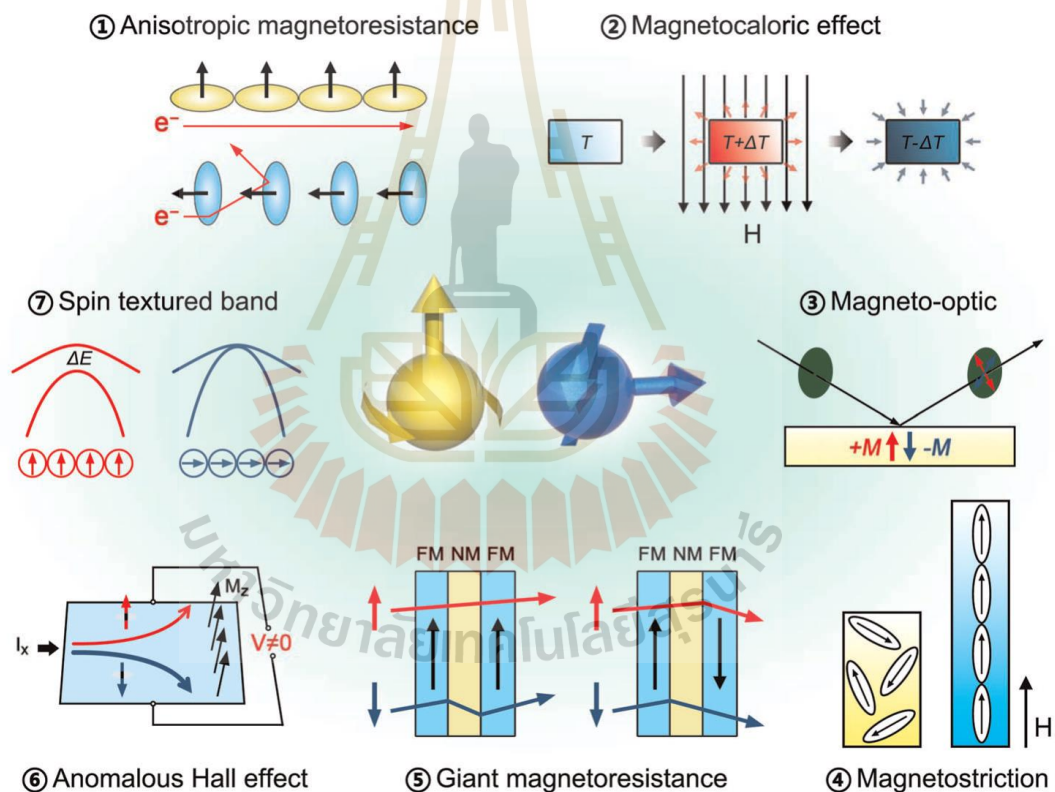
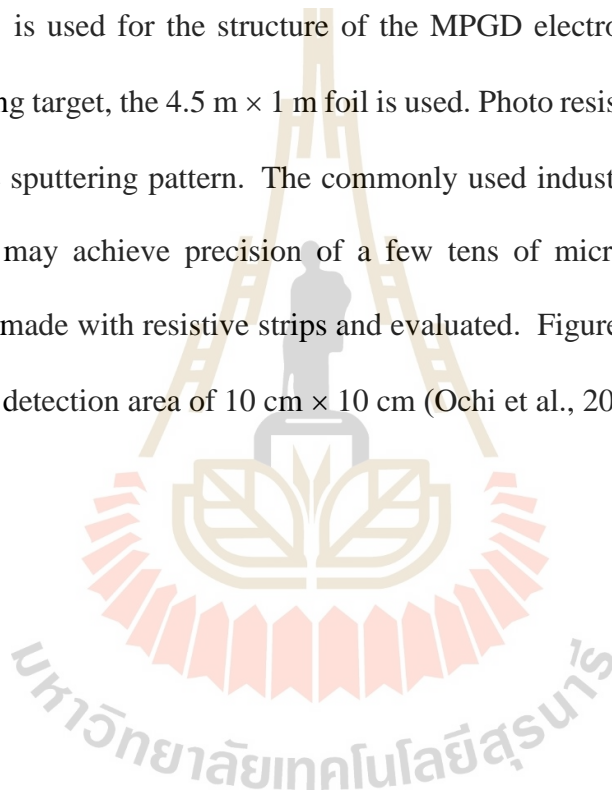


Figure 2.20 Magnetization direction controlled physical properties (Liao et al., 2020).

2.4 The application of DLC films for PandaX-III

PandaX-III is a gaseous Xenon Time Projection Chamber (TPC) with a high pressure for detecting Double Beta Decay. DLC has outstanding mechanical and chemical qualities that are similar to those of crystalline diamond, allowing it to be used as a protective coating in a variety of applications. DLC films have been deposited using a number of ways so far. By integrating the liftoff technique, amorphous diamond-like carbon (a-DLC) is used for the structure of the MPGD electrodes. As a substrate and graphite sputtering target, the 4.5 m × 1 m foil is used. Photo resist imaging determines the precisions of the sputtering pattern. The commonly used industrial printed circuit board (PCB) method may achieve precision of a few tens of micrometers. MicroMEGAS prototypes were made with resistive strips and evaluated. Figure 2.21(a) depicts a small prototype with a detection area of 10 cm × 10 cm (Ochi et al., 2014).



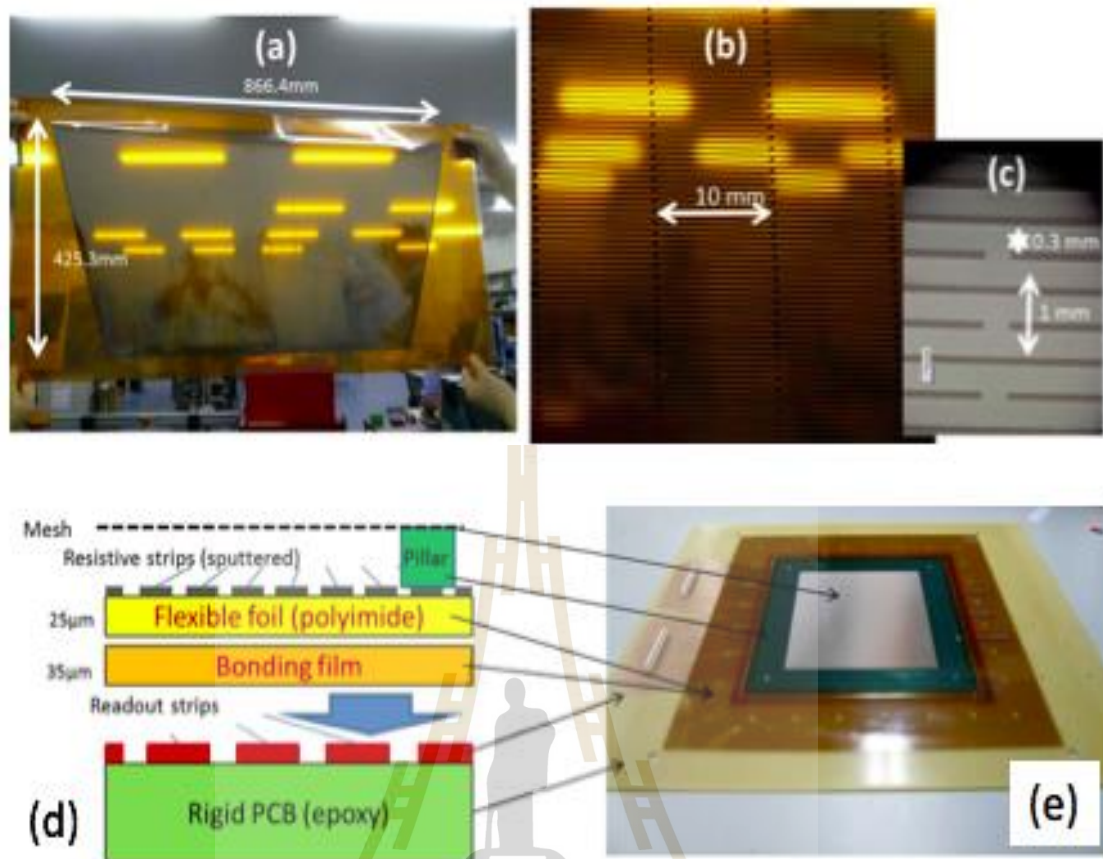


Figure 2.21 The schematic cross section of the 10 cm x 10 cm resistive MicroMEGAS with sputtered carbon, as well as an image of a prototype chamber are shown below (Ochi et al., 2014).

Figure 2.21 shows the big foil (a), an enlarged image (b), and a microscopic image (c). The trapezoidal shape of 85 cm × 45 cm was successfully created using 415 mm pitch strips. The uniformity resistivity of this huge foil was tested. As indicated in figure 2.21, DLC large foil will be used as a resistive electrode in the PandaX III detector (Ochi et al., 2014).

The resistivity map for big resistive strip foil is shown in figure 2.22(a). For each 5 cm position, the resistivity of the HV feed line (both inclined sides) was measured. The units of measurement are MW. Although the projected resistive value has not yet been

computed, this finding is consistent with estimations, and the uniformity is estimated to be less than 30%. (Ochi et al., 2014).

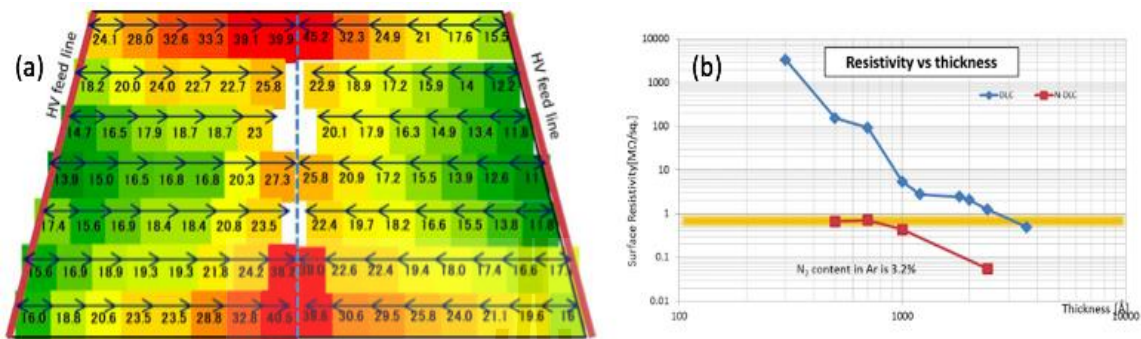


Figure 2.22 Large resistivity map for resistive strip foil. Resistivity of the surface as a function of sputtered carbon thickness (Ochi et al., 2014).

Surface resistivity as a function of sprayed carbon thickness is shown in figure 2.22(b)). The resistivity of pure carbon sputtering is shown in blue, whereas that of nitrogen doped foils is shown in red. The orange ring reflects the ATLAS MicroMEGAS's needed resistivity (Ochi et al., 2014).

Figure 2.23 depicts the resistance of pure and 8 percent boron-doped DLC sheets as a function of temperature. As the temperature and is dropped, a considerable rise in resistance is noticed, as expected in a metal-to-insulator transition (Sikora et al., 2009).

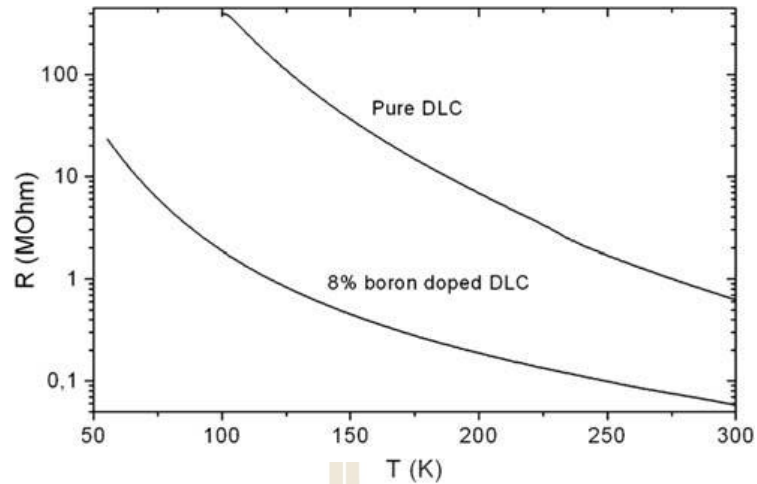


Figure 2.23 On a semilogarithmic scale, resistance fluctuation in megaohms of pure DLC and 8 percent boron-doped DLC versus temperature (Sikora et al., 2009).

Unfortunately, malfunctions were reported at 60 kV. They were caused by a cathode ring in one corner where the panels were connected. The machined dovetails can leave small air-filled gaps, according to a closer examination. In the mockup, the gaps were even positioned in the radial direction, which is the direction of the electric field. The thickness of Acrylic moved in this route was much less than 20 mm, even without counting trails on surfaces. During a redesign, the dovetails were all cut to different lengths. As a result, radial alignment was avoided. At the same time, the panel thickness was increased from a potentially dangerous 20 mm to a safe 50 mm. There were no more concerns with the modified mock-up throughout subsequent tests (see figure 2.24(a)). The cylinder needs to be assembled with a lot of force, which is difficult with this panel design. The fact that the force must be exerted at an angle to the Acrylic surface adds to the difficulty. It was decided to adjust the design after discussing with the Acrylic cylinder manufacturer. We'll construct the cylinder using a different method, obviating the need for dovetails totally (Chaiyabin et al., 2017).

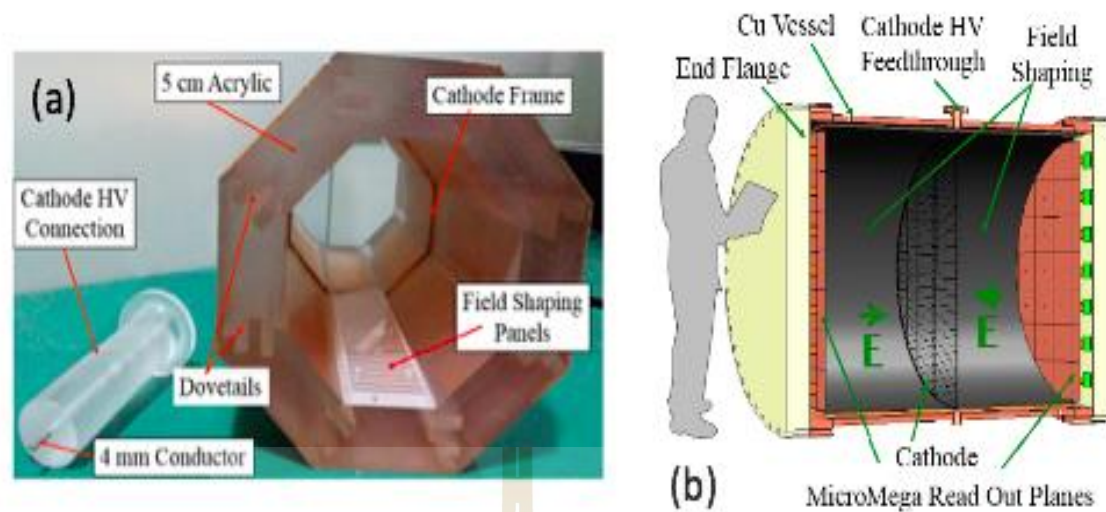


Figure 2.24 a) The field cage mock-final up's design. The acrylic thickness was raised to 50 mm. b) Aerial image of the PandaX III detector by an artist (Chaiyabin et al., 2017).

PandaX-III is a TPC that detects Double Beta Decay using High Pressure Xenon (HPXe). The detector will be installed in the JinPing lab in China's Szechuan province (CJPL II). A 2 m long cylinder with a 1.6 m inner diameter serves as the detection vessel. It has a 35mm wall thickness and is made of oxygen-free high conductivity (OFHC) copper to securely withstand the 10 bar pressure of 200 kg of 90 percent enriched ^{136}Xe . At normal temperature, the detector will switch on and off. As a result, a cryogenic instrument is not required. It will be immersed in a large water barrier with more than 5 meters of pure water in all directions during data collecting, as shown in figure 2.24(b).

Flat end caps, which are unusual for a pressure vessel, are shown in Figure 2.25. Domed end caps would, in fact, be easier to produce. Flat coverings, on the other hand, are more compatible with both ends' flat read out planes. We must restrict the amount of dead xenon to a minimum due to the limited supply and highly high cost of enriched ^{136}Xe (Chaiyabin et al., 2017).

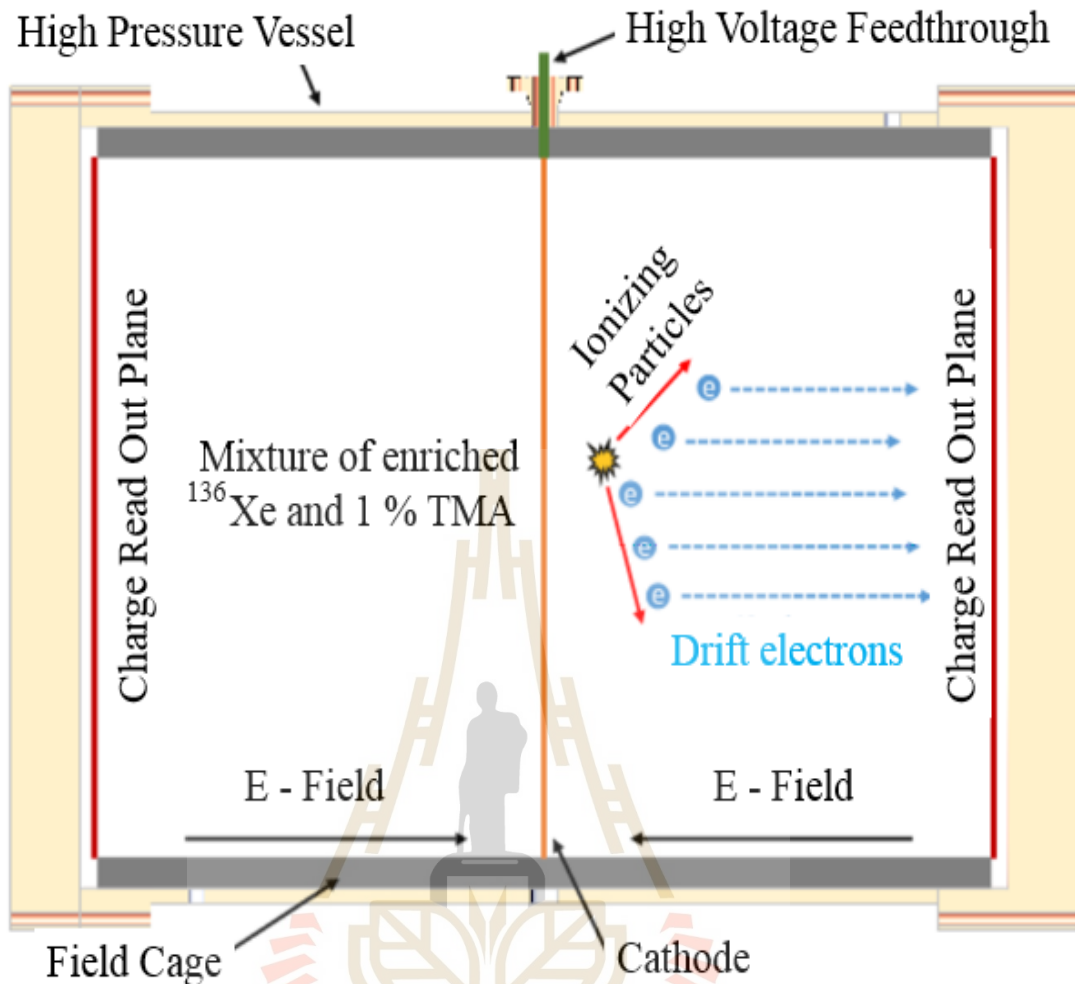


Figure 2.25 Schematic view of the PandaX III detector (Chaiyabin et al., 2017).

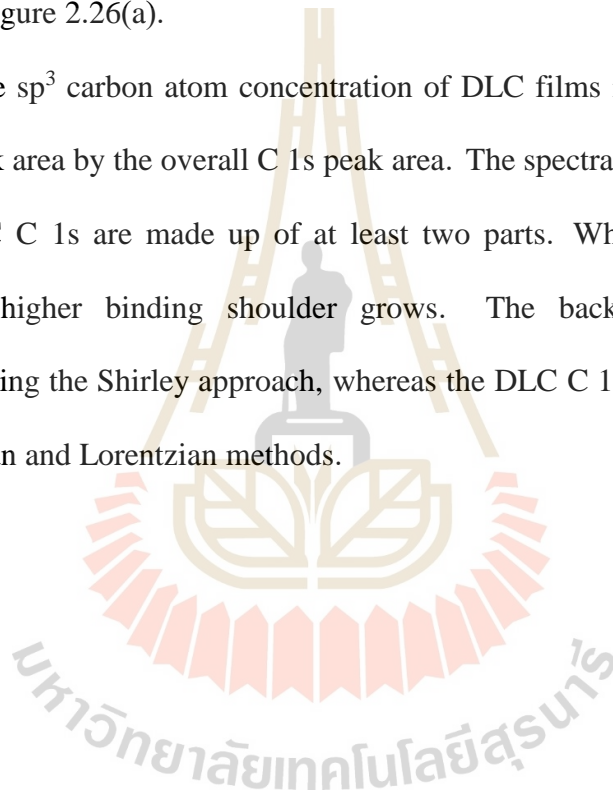
2.5 DLC films characterization techniques

Various analytical approaches, such as X-ray photoemission spectroscopy (XPS), infrared spectroscopy (IR), and thermal desorption spectroscopy, can be used to approximate the $sp^2:sp^3$ bonding ratio in DLC (TDS). This section describes some of the most prevalent ways for evaluating DLC films. The techniques used in this work, on the other hand, are highlighted.

2.5.1 X-ray photoemission spectroscopy (XPS)

The most powerful equipment for examining the composition of DLC films appears to be X-ray photoelectron spectroscopy (XPS). DLC films examination of XPS is difficult in the early phases and necessitates specialist due to its sophisticated nature. Merel and his colleagues used the breakdown of C1s to determine the sp^3 concentration of DLC films until 1995. The XPS C1s peaks of DLC samples grown at various laser intensities were shown in figure 2.26(a).

The sp^3 carbon atom concentration of DLC films is calculated by dividing the relevant peak area by the overall C 1s peak area. The spectra in figure 2.26(b) clearly reveal that DLC C 1s are made up of at least two parts. When the laser intensity is increased, the higher binding shoulder grows. The background contribution is approximated using the Shirley approach, whereas the DLC C 1s peaks are fitted using a blend of Gaussian and Lorentzian methods.



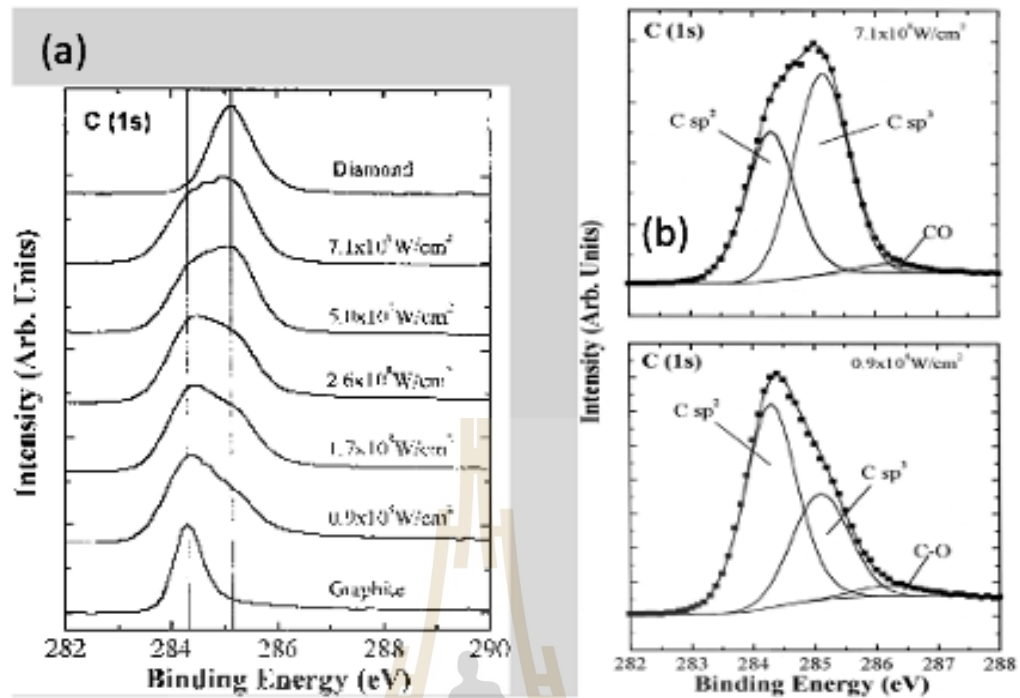


Figure 2.26 a) At various laser intensities, XPS C 1s peaks of a graphite target, diamond thin film, and DLC thin films were obtained. b) Deconvolution of the DLC films deposited at 0.9×10^8 and 7.1×10^8 W/cm² XPS C 1s peaks (Merel et al., 1995).

Figure 2.26(b) shows the fits of the samples deposited at the highest and lowest laser intensities. At 284.4 eV and 285.2 eV, the C1s XPS spectra are divided into at least two primary components, which correspond to sp² and sp³ hybridized carbon atoms, respectively. The ratio of the aforementioned peak area over the entire C1s peak area is utilized to calculate the sp³ carbon atom concentration from the deconvoluted spectra. This approach is currently reliable and well accepted (Merel et al., 1995). XPS is a highly surface-sensitive technology, so it's important to keep the surface clean. Surface analytic studies are typically carried out under ultrahigh vacuum (UHV) conditions for comprehensive characterization with highly surface-sensitive technologies. Despite the

fact that the residual gas pressure is quite low under UHV circumstances, the surfaces are never kept completely clean (Steinberger et al., 2017). As a result, for removing contaminants on surfaces, XPS analyses have been employed in conjunction with sputter ion etching.

One of the most dependable techniques for analyzing the structure of DLC films is XPS, which is well known. This is a surface-sensitive approach, thus surface contamination on the sample must be avoided. Surface pollutants, on the other hand, can be identified using this technique. Zemek and the rest of the group have validated the above information (Zemek et al., 2016). The effects of argon sputtering on DLC and nanocrystalline diamond film surface XPS analysis are investigated. Before and after cleaning surfaces, sp^2 and sp^3 hybridization of DLC films are shown. Using high-energy resolution core-level XPS, the effect of an argon cluster ion beam on the composition and chemical bonding of DLC and nanocrystalline was examined, with a focus on the peak widths and hybridization of carbon atoms as determined by C 1s lines.

2.5.2 X-ray absorption spectroscopy (XAS)

Because of its capacity to provide high accuracy information on the local structure around excited carbon atoms and the orientation of carbon bonds, the XAS approach has lately gained popularity for characterization of diverse carbon films. The properties of X-ray absorption spectra were used to judge the local bonding configurations within an amorphous carbon in the beginning of the XAS approach (Lenhart et al., 2005). Shinya and his team successfully used deconvoluting near-edge X-ray absorption fine structure (NEXAFS) to investigate local bonding topologies inside amorphous and nanocrystalline carbon till 2009. (Shinya et al., 2009).

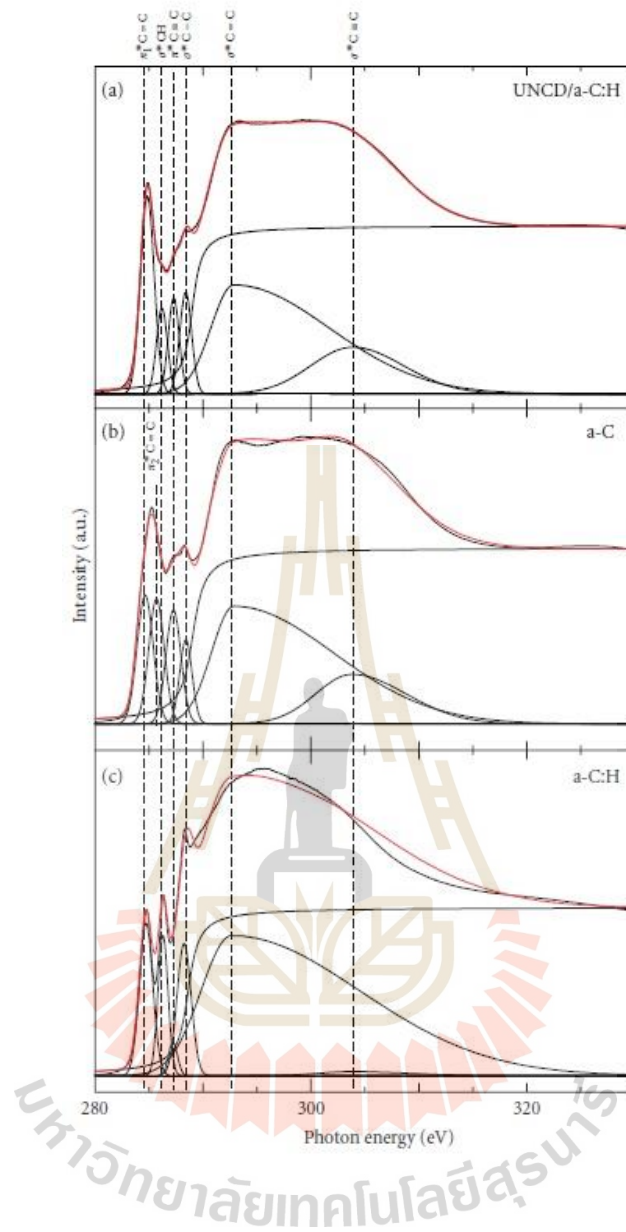


Figure 2.27 Experimental and fitted NEXAFS spectra of (a) UNCD/a-C:H film deposited, (b) a-C film deposited, and (c) a-C:H film (Shinya et al., 2009).

Different bonding configurations such as and bonds were identified by deconvoluting the absorption spectra of carbon films. Figures 2.27(a), (b), and (c) show the NEXAFS spectra of the UNCD/a-C:H film, a-C film, and a-C: H film, respectively. A spectrum from fitting is represented by the red solid line. The experimental data is

subtracted in data analysis by an error-function step originating from the C K-edge at the ionization potential. The C=C, C-H, and C-C peaks in the subtracted spectrum decomposed into Gaussian peaks (Shinya et al., 2009).

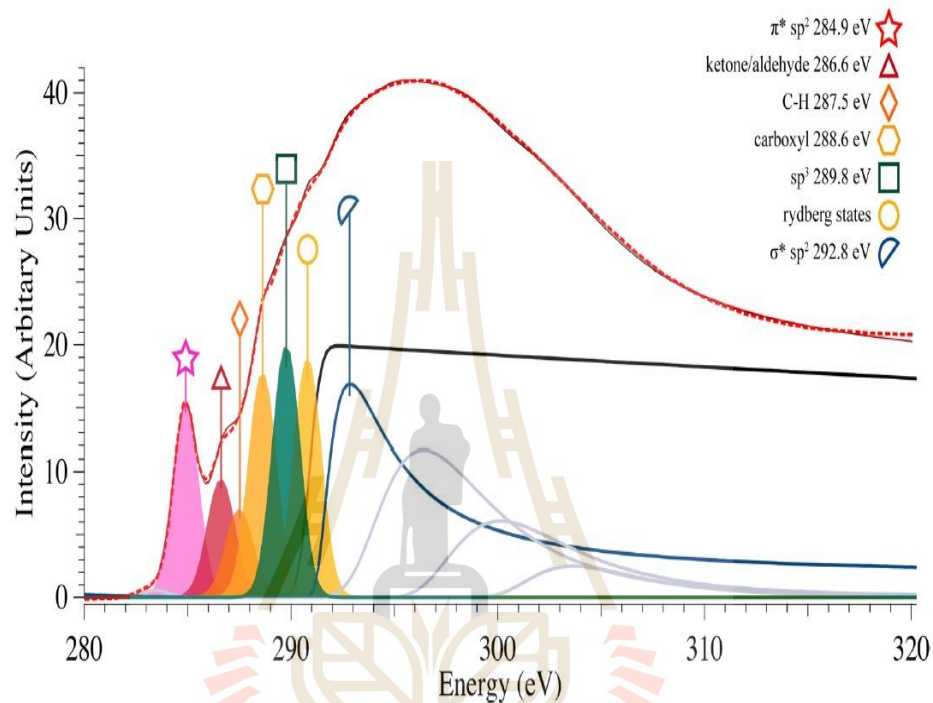


Figure 2.28 Measured (black dotted line) and fitted (red line) C k-edge taken from ta-C film (Sainio et al., 2016).

At this time, using the XAS approach to investigate local bonding configurations is widely acknowledged and applied. The transition peaks and ionization function make up the majority of C K-edge spectra. The corresponding peak area over the overall C K-edge peak area is used to evaluate the sp^2 and sp^3 bond ratios. As shown in figure 2.28, the C K-edge spectra of a ta-C thin film (one of the DLC structures) has seven peaks corresponding to sp^2 , ketone/aldehyde, C-H, carboxyl, sp^3 , Rydberg states, and sp^2 at 284.9, 286.6, 287.5, 288.6, 289.8, 291.0, and 292.8 (Sainio et al., 2016).

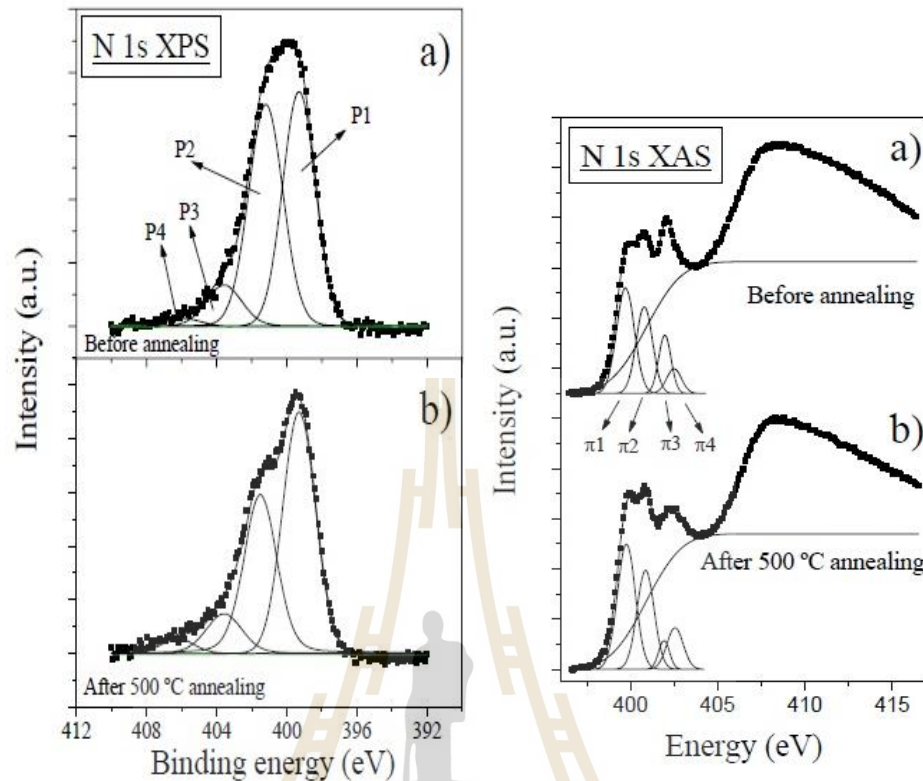
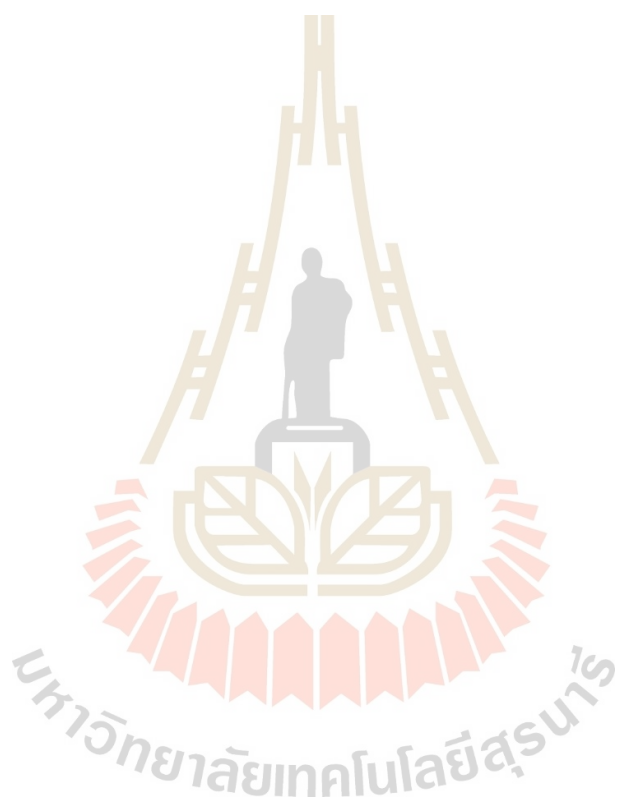


Figure 2.29 The XPS N 1s and XAS N k-edge spectra of the sample with nitrogen content before and after annealing (Quiros et al., 2015).

There have been numerous reports on the comparison of XAS and XPS techniques (Quiros et al., 2015). Figure 2.29 shows N k-edge XAS and N 1s XPS of a carbon nitride sheet. Quiros and his colleagues used XAS and XPS techniques to examine amorphous carbon nitride sheets. The effects of annealing treatments on the XPS and XAS spectra have been detected. Different sputtering and assistance conditions are used to generate carbon nitride films. Their atomic ratios of N/C on the surface are 0.3 and 0.5, respectively. The N 1s XPS and N k-edge XAS spectra of the sample with nitrogen concentration before and after annealing are shown in Figure 5. A link between the low

binding energy components of XPS at 399.3 eV, with transitions 399.6 and 400.8 eV of XAS spectra were observed.



CHAPTER III

EXPERIMENTS AND METHODS

In this chapter describes techniques and experimental details of this thesis work. The information of the instrumentations and experimental setup are also provided. The materials investigated in this work was DLC films prepared by a HiPIMS technique. In addition to electrical properties measurements, advanced characterization techniques such as XPS and XAS were employed to study the elemental and chemical composition in the DLC films. A simple set-up for out gassing measurement was used to investigate the out-gassing rate of the substrate.

3.1 The HiPIMS system and setup

All of the experiments took place in a custom-built cylindrical vacuum tank with a diameter of 260 mm and a length of 300 mm that was pumped down to a base pressure of 6.5×10^{-4} Pa using a turbo molecular pump and a rotary pump. Argon was injected into the tank at flow rates ranging from 4 to 32 sccm to modify the working pressure between 0.27 Pa and 2.4 Pa. A capacitance pressure gauge was used to determine and control the operational pressure and flow rates. Figure 3.1 depicts the general layout of the chamber (Poolcharuansin et al, 2015).

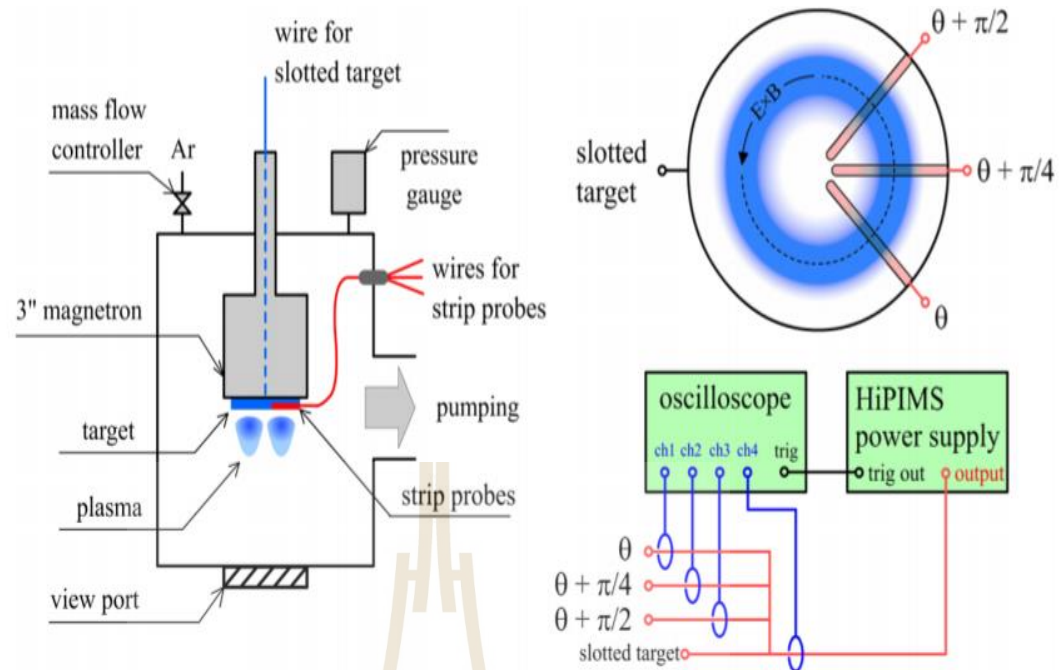


Figure 3.1 Schemes of HiPIMS (Poolcharuansin et al., 2015).

As indicated in figures 3.2(a) and (b), we implemented the HiPIMS technique at Maharakham University and SLRI Thailand. The HiPIMS power supply is superimposed over a dcMS power supply with graphite target in the sputtering system for film deposition, as shown in figures 3.3(a) and (b). The rate of deposition of DLC films under various deposition conditions is depicted in many conditions. It is commonly known that the rate of film deposition is highly influenced by the target's sputtering rate. When the HiPIMS is superimposed, both the ionization ratio and the sputtering rate increase, resulting in a higher deposition rate.

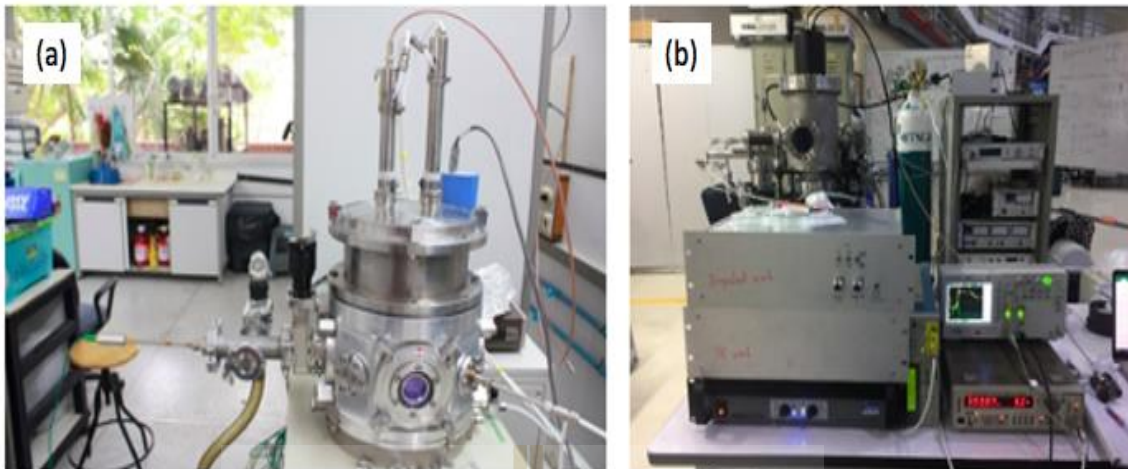


Figure 3.2 a) Setting up HiPIMS technique at Mahasarakham University and b) HiPIMS at SLRI Thailand.

We must create plasma in a vacuum system in HiPIMS. Pumps can help us create a vacuum in the chamber. We'd like a high-vacuum system to increase the mean free route to atoms and reduce gas pollution. As a result, we chose the turbomolecular pump since it has a high vacuum range of 10^{-2} to 10^{-8} mbar. We need to pump at atmospheric pressure, hence we'll need a pump that can handle atmospheric pressure up to 10^{-2} mbar. To connect to the turbo pump, we use a scroll pump. We can flow Ar gas into the chamber at roughly 10 sccm when the chamber's base pressure is around 10^{-5} mbar. When the system reaches a pressure of roughly 10^{-2} mbar, we can start deposition films by turning on the HiPIMS to magnetron as shown in figure 3.4.

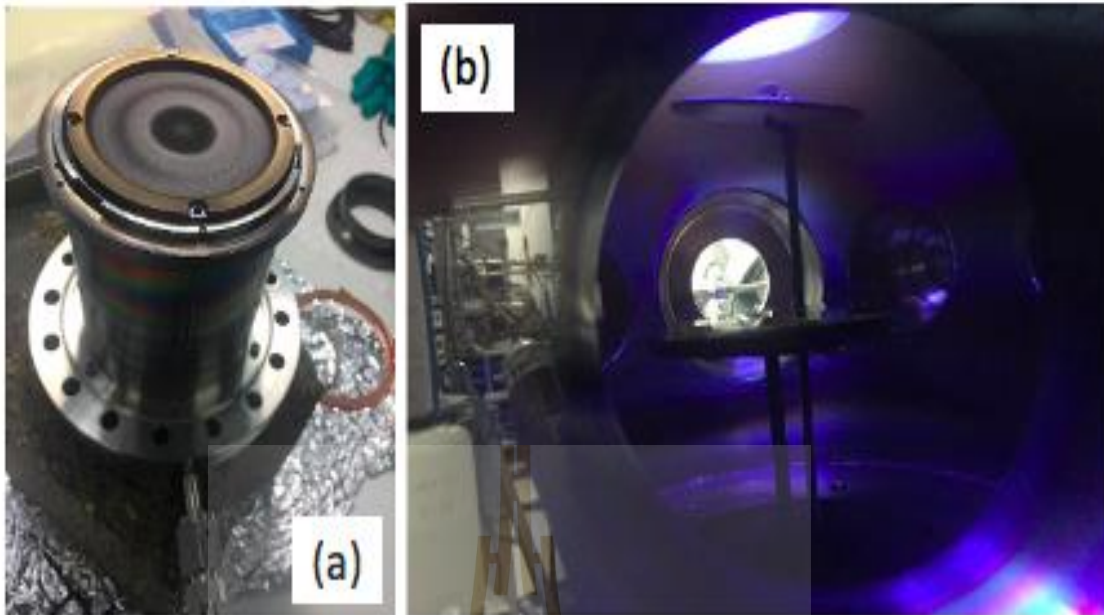


Figure 3.3 a) Graphite target and b) sputtering system.

HiPIMS employed pure graphite as the objective for making DLC films. Microscope slide glass with 11 cm² and 25 cm² diameters was employed as a substrate for DLC films. In an ultrasonic bath. For 20 minutes, the substrates were gently washed with ethanol and then DI water.

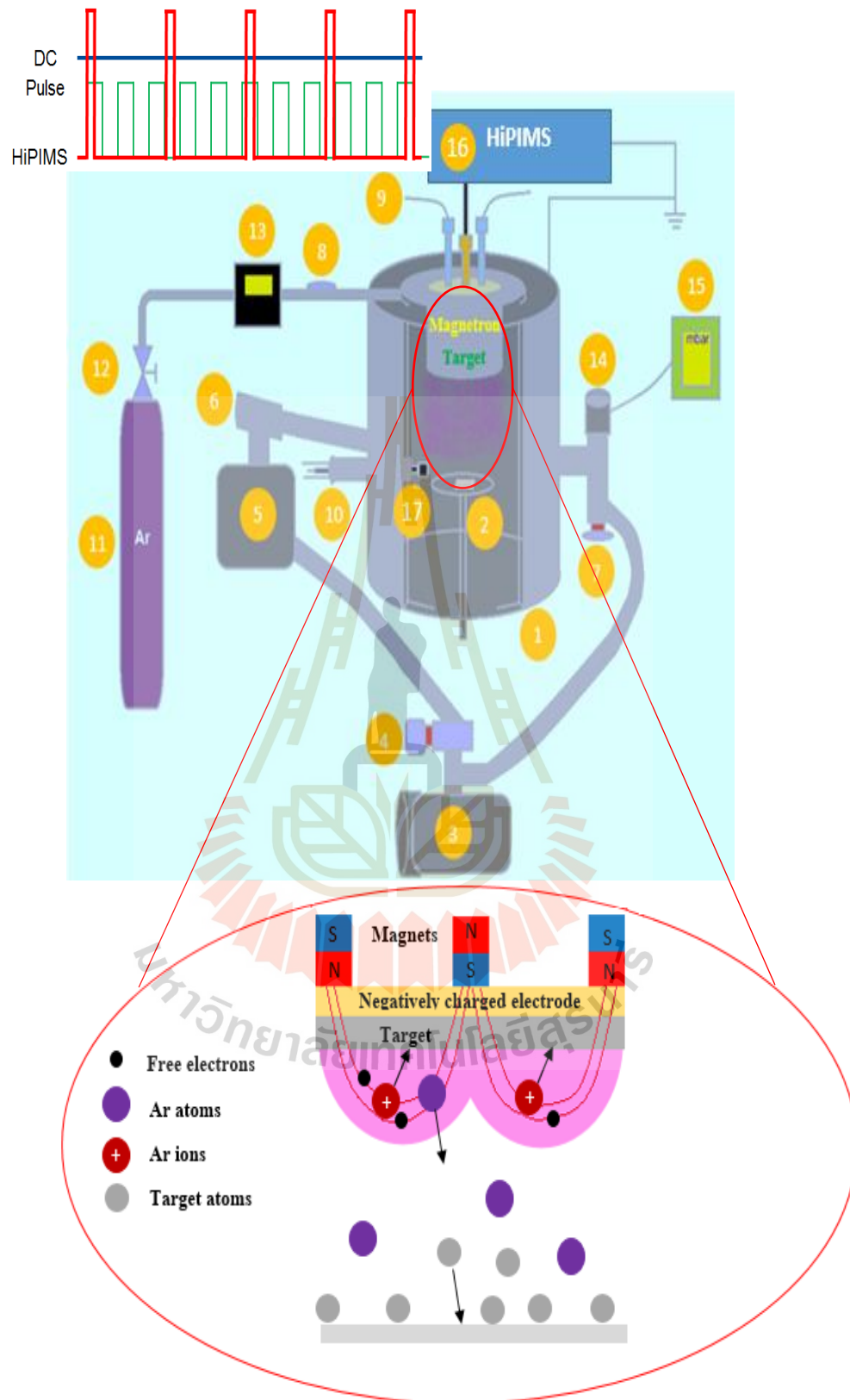


Figure 3.4 Plasma in HiPIMS and starting deposition time.

The substrates were then N_2 gas-blow-dried. The smaller substrates were prepared for chemical and structural analysis, while the bigger ones were prepared for electrical resistivity testing.

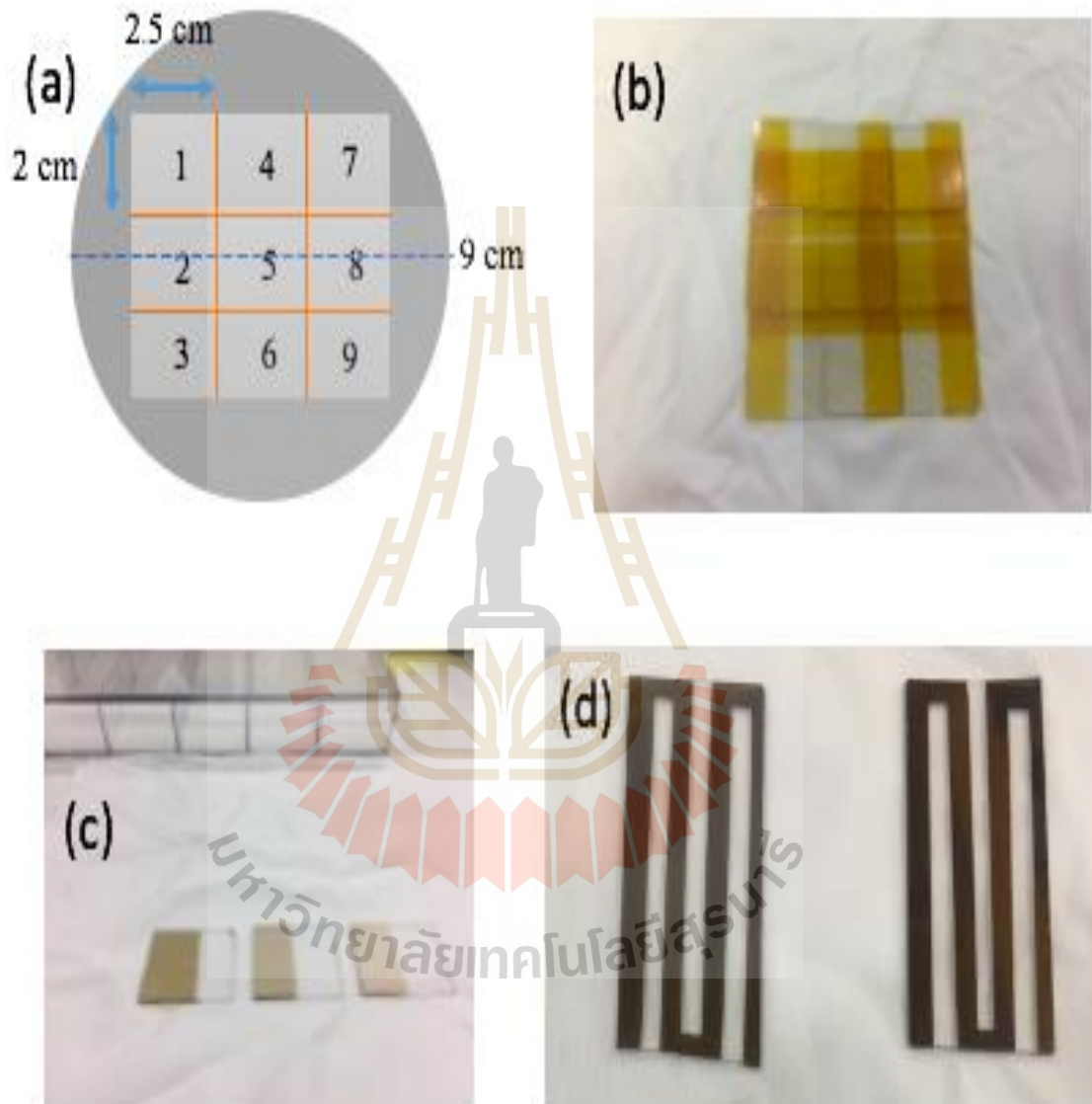


Figure 3.5 a) Holder substrate with 1 series, b) substrate as Kapton foil with pattern, c) DLC films after deposited and d) DLC films as pattern on glass substrates.

Graphite target is used to deposit DLC films on glass and acrylic substrate for 10, 20, and 30 minutes. Figures 3.5(a) and (b) show how Kapton tape is used to adhere substrates as a pattern. Figure 3.5(c) shows the DLC films after deposited on the substrate. The sheet resistivity (ρ) of the DLC films was measured using a mega-ohm electrometer to measure the resistance (R) between left and right ends of the DLC strip, as illustrated in figure 3.5(d).

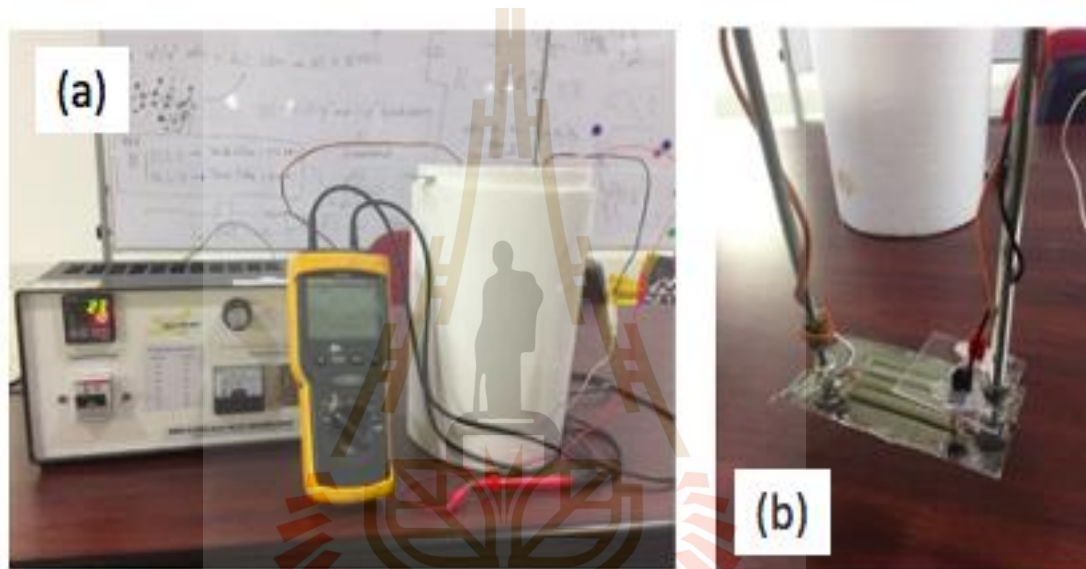


Figure 3.6 a) Measuring resistance of DLC films by mega-ohmmeter with liquid nitrogen environment and b) test probe.

HiPIMS deposited DLC thin films for 10, 20, and 30 minutes at a specified average power of 110 Watts. The Ar gas flow rate was maintained at 25 sccm throughout the experiment. The operating pressure was around 4.5 mTorr, with a distance of 60 mm between the target and the substrate. A mega-ohm electrometer was used to test the electrical resistance between both ends of the patterned DLC films. Using nitrogen vapor in a liquid nitrogen dewar, the temperature of the films may be regulated. A laser

interferometer was used to determine the thickness of the DLC films; figure 3.6 shows the measurement of DLC films. Resistance of DLC films were measured by pico-ammeter equipped with electronics shield with stainless steel foil box as shown in figures 3.7(b) and (c).

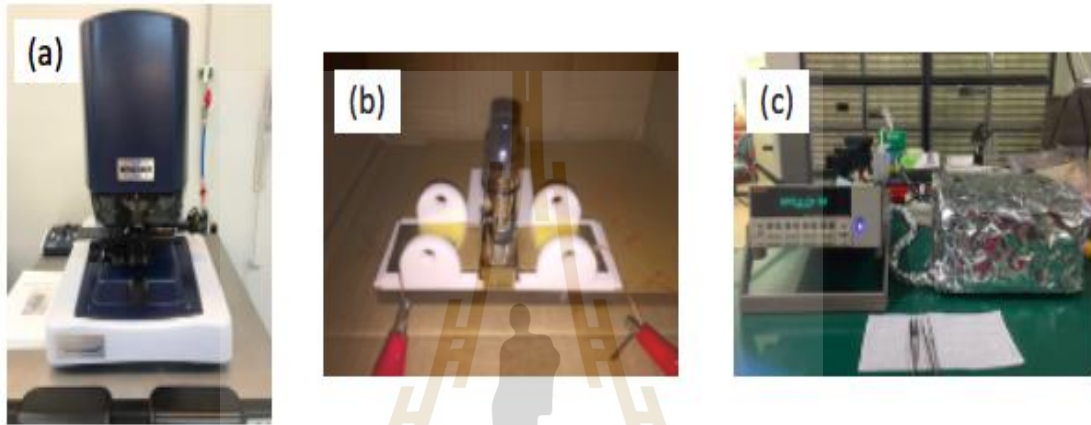


Figure 3.7 a) Laser interferometer instrument for measured thickness of DLC films. b) Measuring resistance of DLC films by pico-ammeter and c) electronics shield with stainless steel foil box.

3.2 Outgassing measurements

RGA measures the outgassing rate of PTFE and acrylic under a variety of circumstances. First, the chamber is cleaned at 200 degrees Celsius and then chilled for around 24 hours. The leakage of the chamber is measured, followed by acrylic or Teflon in a vacuum chamber under four conditions. Finally, the RGA spectrum and outgassing rate of acrylic or Teflon are measured, as illustrated in figure 3.8.

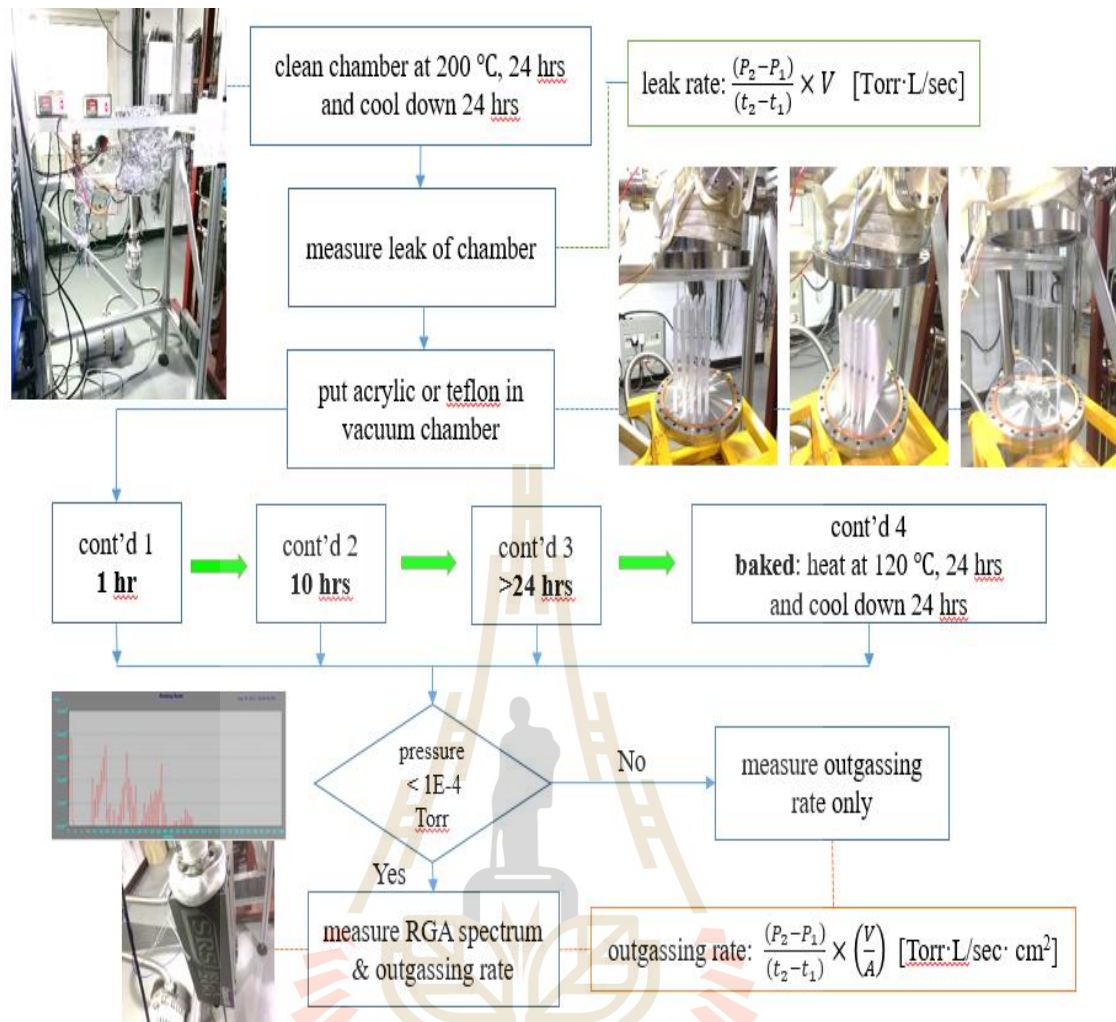


Figure 3.8 Scheme of PTFE and acrylic outgassing measurement.

3.3 Characterization techniques

3.3.1 principle of synchrotron radiation

A synchrotron is a huge machine that accelerates charged particles such as electrons and ions to near-light speeds. When these electrons or ions are deflected by magnetic fields, they produce synchrotron radiation or synchrotron light, which is highly electromagnetic radiation. The synchrotron's main structures are depicted in figure 3.9. The electrons generated by the electron gun (1) are accelerated in the linear accelerator

(linac) in the first stage (2). This wave causes high electric and magnetic fields and is used to accelerate electrons. When the electrons enter the linac, the intense electric field are switched back and forth between negative potential and positive potential (Wilson et al., 1996).

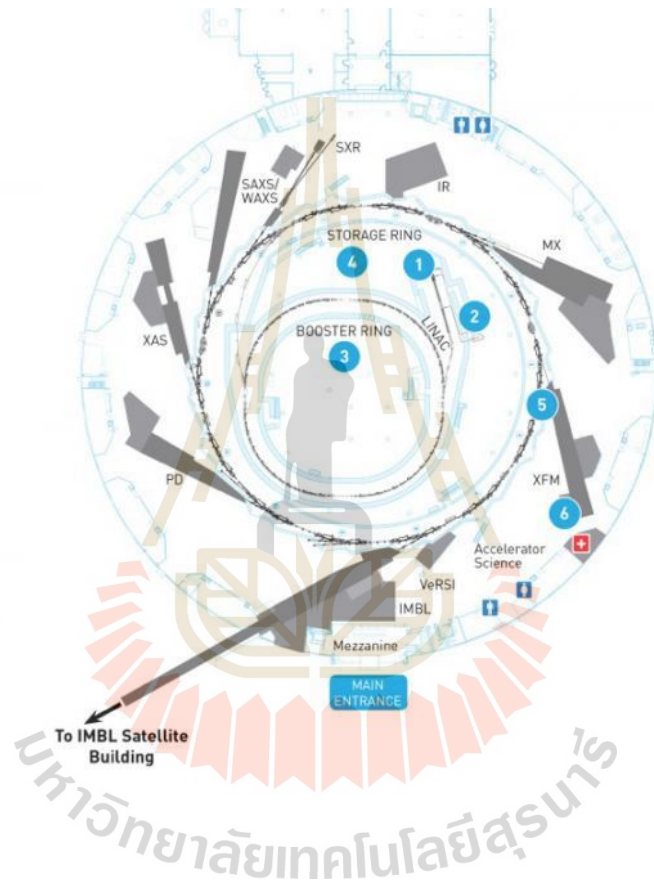


Figure 3.9 The principal structures of the synchrotron (ANSTO group, 1997).

Charged particles (electrons) are propelled to the speed of light as a result of the change in electric field. They are transferred to the booster ring (3) in the second stage, where they are accelerated in the energy range up to giga-electron volts while the magnetic field is adjusted to match the energy of the electrons in order to maintain the electric radius of curvature. After that, they're moved to a circular storage ring (4). Synchrotron light is emitted tangentially to the electron orbit when electrons in the storage ring are diverted by

the magnetic field. This radiation is carried into the beamlines (5), where it is used in a variety of studies. Synchrotron radiation spans a wide range of wavelengths in general (over 4 types, consists of infrared, visible light, ultraviolet, and x-rays). This radiation is extremely bright, or millions of times brighter than other light sources.

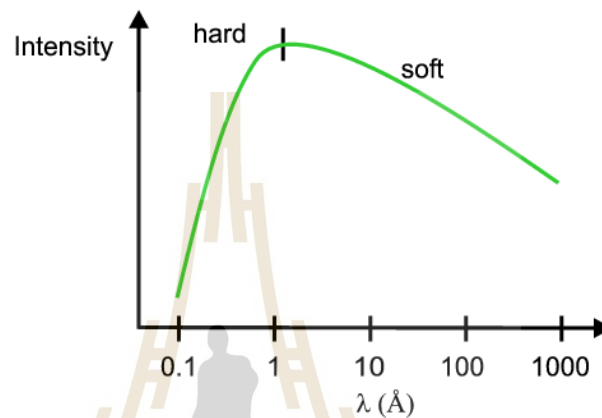


Figure 3.10 The spectrum range of the synchrotron radiation (Paul et al., 2006).

The synchrotron radiation possesses unique properties include Wide continuous spectrum and adjustability, polarization, Very high intensity (flux) and high brilliance, and Pulsed character. The details will be summarized below.

A bending magnet produces a continuous spectrum of synchrotron radiation. Figure 3.10 depicts the spectral range of synchrotron radiation. This range extends from infrared to hard X-rays. Synchrotron light is sometimes referred to as white light because its spectrum contains all wavelengths. Furthermore, synchrotron radiation may be tailored to the right energy range for any material, making it an adaptable source of radiation. The synchrotron radiation emitted by a bending magnet is horizontally polarized in the plane of the storage ring and linearly polarized above and below the orbit, but the emission

synchrotron radiation above and below the orbit is circularly polarized. The vibration of synchrotron sources is horizontally polarized, as illustrated in figure 3.4, but X-ray radiation from laboratory sources vibrates in all planes. This function is useful when researching magnetic materials. Synchrotron radiation has a very high photon flow. In general, the flux is determined by the number of electrons cycling in the ring per unit time (beam current), which is much higher in synchrotron radiation than in ordinary X-ray sources. Synchrotron radiation's tremendous flux and brightness can be utilized to measure tiny and diluted samples, as well as high-resolution data. Synchrotron radiation is not continuous, but rather occurs in short bursts. Synchrotron radiation's pulsed property can be studied in specific specialized studies (Paul et al., 2006).

3.3.2 BL3.2Ua of the Synchrotron Light Research Institute (SLRI)

XPS spectra were used to determine the chemical bonding states of DLC films. As shown in figure 3.11, XPS measurements were taken at the Synchrotron Light Research Institute of Thailand's BL3.2Ua: PES (Photoelectron Emission Spectroscopy) beamline. A thermionic electron gun generates the electrons, which are subsequently accelerated in the linear accelerator by a 2,856 MHz high-power microwave (LINAC). The LINAC generates a 40 MeV electron accelerator, which is then delivered to the booster synchrotron and accelerated to 1.2 GeV. The electron beam energy from the Synchrotron source is 1.2 GeV, with a 150 mA electron current injected for each operation cycle. The beam emittance is 41 nm-rad. The beam current is operated at 100 mA with a lifetime of approximately 12 hours.

When compared to beam size, the DLC film was formed on the substrate holder, and the sample scale area must be greater than 55 mm². On the substrate holder, fluorescent and gold samples are utilized to check the beam position and as a reference, respectively. To

prevent the electric charging of DLC films, a portion of the top of the sample is covered with stripes of conductive carbon tape.

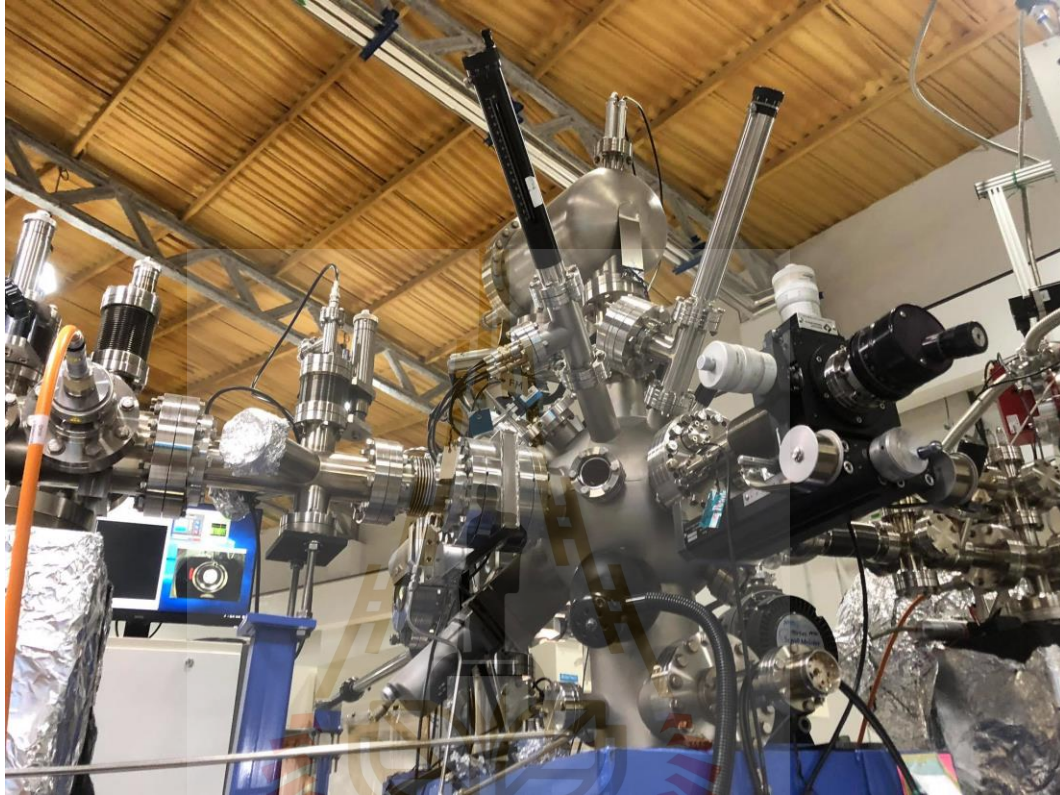


Figure 3.11 XPS and XAS measurements at BL3.2Ua: PES.

3.3.3 principle of XPS

Surface investigation techniques such as X-Ray photoelectron spectroscopy (XPS) probe a depth of 2 to 5 nm from the surface. Chemical species of the atom at the surface can be revealed via XPS. It works on the basis of the photoelectric effect. Irradiating a material with soft x-rays causes electrons in the core level to be excited to vacuum states. The binding energy and the exciting photon energy determine the kinetic energies of these excited electrons. The number of emitting electrons in each kinetic energy or binding energy is displayed in a general XPS spectrum. Because the binding energies

are element-specific. The photoelectron can be used to determine which elements are present in a given substance.

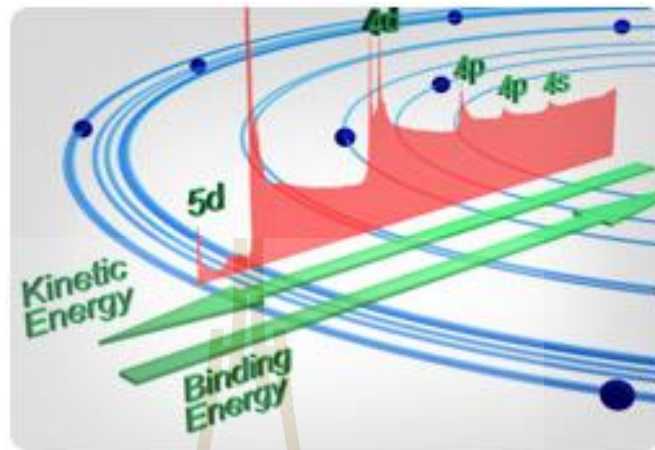


Figure 3.12 the electronic state exists in the atom.

Each XPS peak displays the electronic states present in the atom (e.g., 1s, 2s, 2p, 3s, etc.) as illustrated in figure 3.12. Gaussian-Lorentzian curves can be seen in the XPS peaks. Due to many factors affecting the magnitude of FWHM, such as the resolution of the detector or the size of an X-ray beam, the breadth of FWHM is a determinant of chemical bond in samples. The following equation gives the kinetic energy of emitted photoelectrons.

$$E = E_k + E_B + \Phi, \quad (3.1)$$

where E is the photon energy, E_k is the electron's kinetic energy after being expelled, E_B is the electron's binding energy in the material, and Φ is the material's work function. The minimal energy necessary for an electron to escape from a substance is specified as the work function. Core electron binding energies can range from 10 eV to a

few keV, while typical work functions are on the order of a few eV. As a result, soft X-rays (200-2000 eV) are routinely used to excite a wide variety of orbitals in most elements. Figure 3.7 depicts the entire procedure. Both Fermi levels are equal for a conducting sample in electrical contact with the analyzer. The work function in equation 3.1 corresponds to that of the analyzer in this example. This is not the case for insulators or samples that cannot be grounded. To calibrate the spectrometer and obtain precise binding energies, reference peaks of well-known energy can be employed. Because the photoelectrons' inelastic mean free route is rather short, XPS is a surface sensitivity technique. The Beer-Lambert law can explain this.

$$I(x) = I_0 \exp\left(\frac{-x}{\lambda \cos\theta}\right), \quad (3.2)$$

$I(x)$ is the intensity after traveling x distances, I_0 is the initial intensity, and θ is the angle between the photoelectron's emitting angle and the surface normal. λ is a mean free path that is inelastic. Approximately 99.7% of photoelectrons that were excited from core electrons came from depths of 3 or a few nm below the surface. Figure 3.13 (Biesinger, 2018) shows the experimental mean free paths of components in various materials (Mohai, 2000).

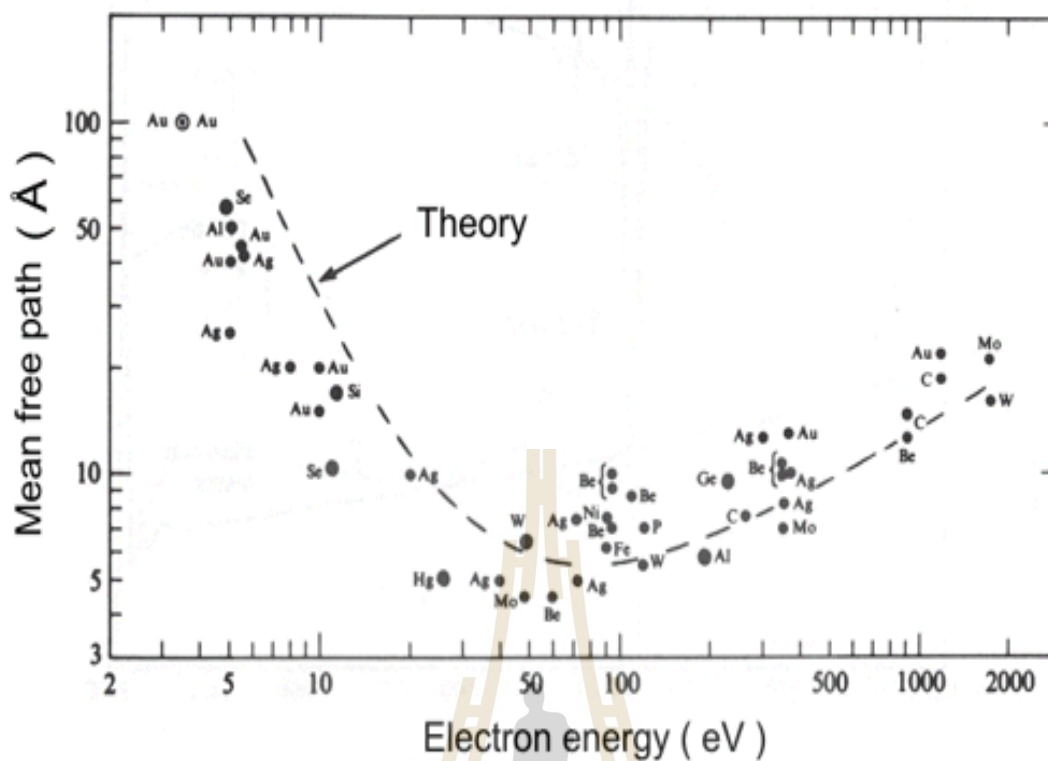


Figure 3.13 The universal inelastic mean free path curve (Raúl, 2000).

Normally, XPS survey spectra are used to determine the presence of components in samples. As shown in figure 3.13, detailed scans of certain orbitals may reveal a number of convoluted peaks with various binding energies, which are the result of different chemical shifts. The existence of atoms bonded in distinct chemical environments, such as attaching to different elements or oxidation states, causes chemical shift. The data can be deconvoluted by fitting a number of Gaussian-Lorentzian peaks to the spectra, and distinct chemical environments can be recognized based on the binding energies of these peaks.

It is frequently impossible to have the sample in electrical contact with the analyser while working with insulating substances. Sample charging occurs when electrons leave the surface and are not replenished. Charging can induce broadening or

splitting of peaks if the charge of the sample surface is heterogeneous, as photoelectron energies are affected by the resulting electric field, and can cause broadening or splitting of peaks if the charge of the sample surface is heterogeneous. A consistent flow of electrons from the anode reduces the effects of charging in spectrometers with a non-monochromated X-ray source, but these electrons are absent when employing a monochromator.

3.3.4 principle of XAS

X-ray absorption spectroscopy (XAS) is a widely used technique for determining a material's local geometric or electrical structure. A core electron is generally stimulated to an empty energy level or ejected from the atom after the electron has been evicted by X-ray. The photons emitted have a unique absorption of energy levels with each element, as electrons from another shell fall into a core hole. In general, XAS relies on the material's absorbance to derive information about the atomic local structure. A core electron is excited to an empty energy level or ejected from the atom after the electron has been evicted by X-ray. As shown in figure 3.14, electrons from another shell fall into a core hole, and the photoelectrons that are emitted have a unique absorption of energy levels with each element. These photoelectrons are also given information about the adjacent atom's local structure, which can be used to derive the local structure of atoms. However, in order to excite electrons from the core-shell, XAS required high-energy X-ray stimulation. As a result, one approach that makes use of the synchrotron light source is XAS. X-ray energy is typically around 104 eV, with soft x-rays ranging from 100 eV to 3 keV being employed for low Z elements like carbon (285 eV), nitrogen (400 eV), and oxygen (530 eV) and hard x-rays are above 3 keV.

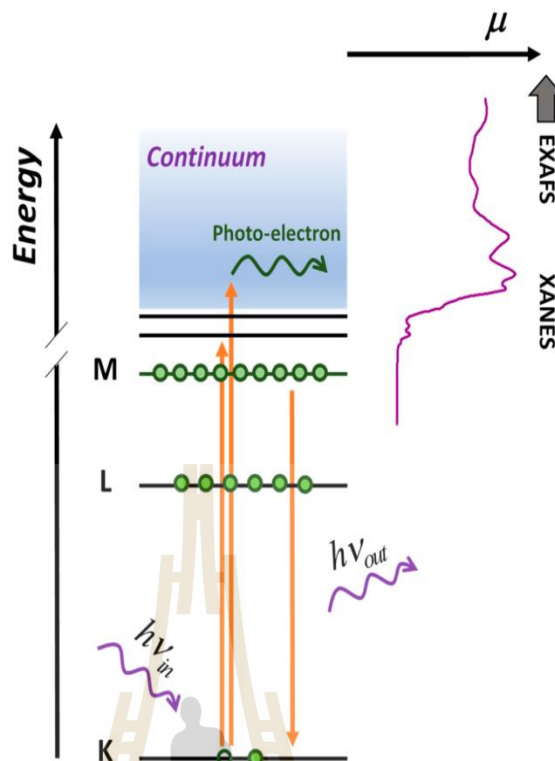


Figure 3.14 The X-ray absorption mechanism is depicted in this diagram (Stöhr, 1992).

The released electrons are from the adsorbate and substrate, as seen in figure 3.11. Soft X-ray sources may typically penetrate a sample to a depth of 1 μm . Before the absorbed X-rays reach the surface, photoelectrons and Auger electrons are created. These electrons' electron-electron interactions are inelastically dispersed. Because of the inelastic scattering of electrons, some electrons cascade. When an electron reaches the surface, those with an energy greater than the work function will escape into the vacuum. Electrons are detected as they emerge from the surface.

The electron distribution around nuclei is described by the Molecular Orbital Theory (MO), which is a wave function. The facilitation of atom bonding was produced by the development of molecular orbitals by combining their atomic orbitals. The electrons are not assigned to a single atomic link, but rather are spread throughout the entire

molecule. The maximum number of valence electrons in each MO is two electrons with opposite spins. The MO with the lowest energy is the first to be filled. According to their symmetry, molecular orbitals are split into distinct categories. Molecular orbitals that are symmetrical around the bond axis are called orbitals. The 1s orbitals of two hydrogen atoms caused one bonding σ orbital and one anti-bonding σ^* orbital.

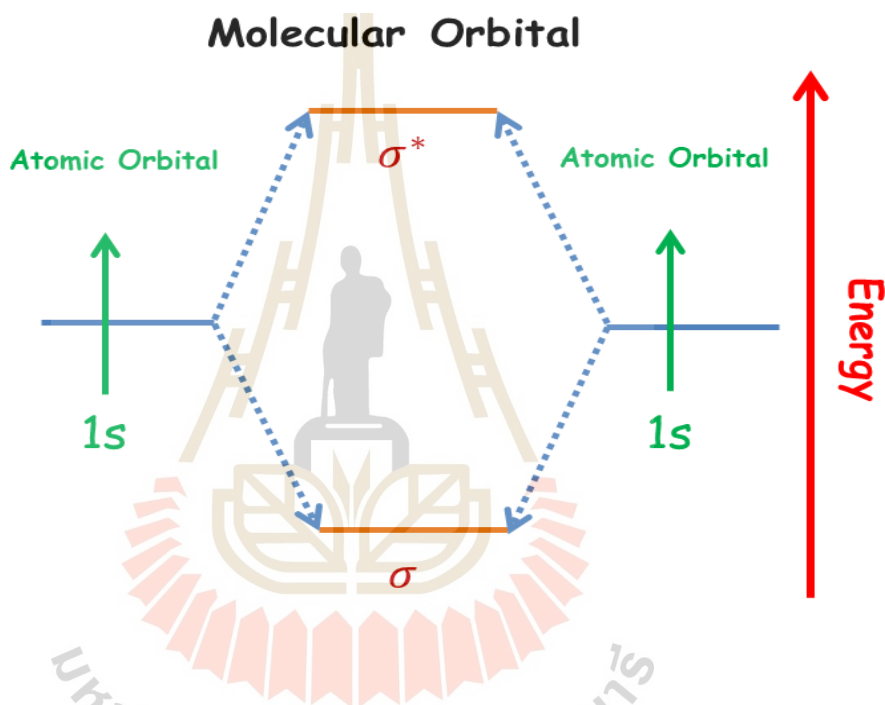


Figure 3.15 The hydrogen molecule's MO diagram. Two σ molecular orbitals are formed from two 1s atomic orbitals.

Figure 3.15 shows a typical K-edge spectrum for a two-atom molecule. The resonances $1s^*$, which consist of a lower energy area and a high-resolution region, are visible in the XAS spectrum. At higher energies above the absorption edge, the resonances corresponding to $1s^*$ transitions exhibit a larger pattern. At the $1s^*$ resonances and the absorption edge, information regarding molecular orbitals does not usually surface.

Furthermore, the $1s^*$ resonance responds exclusively to molecules with double and triple bonds. As a result, the $1s^*$ resonance is absent in single bond molecules (Stöhr, 1992).

The improper variation of raw XAS signal is the first issue to address when normalizing the C K edge XAS spectrum. Many things can generate these variances. The XAS experiment at BL3.2a is depicted in figure 3.14 as a generalized schematic diagram. The backdrop from the beamline effect, which creates the undesirable signal in the raw XAS signal, is the first issue to examine (especially in C k-edge region). The photon energy shift produced by electron beam oscillations in the ring current or undesired absorption signal from carbon contamination on the beamline optics are two examples of background variations (monochromator, grating, mirror etc.). As a result, these backdrops should be eliminated. Normally, the gold mesh is used to calculate background subtraction by measuring photon flux in front of the analysis chamber. The I_0 signal refers to the drain current. In theory, gold has no absorption in the C and N Kedge areas, and only a minor absorption in the O Kedge zone. Only the background beamline signal is present in the C Kedge signal from the gold mesh. As a result, the raw signal's background beamline can be subtracted by dividing it by the I_0 signal.

The background of the removed beamline can therefore be represented as

$$I_{sub} = \frac{I_{sample}}{I_0} \quad (3.3)$$

where I_{sub} refers to the subtracted signal and I_{sample} refers to the sample's raw current signal. However, unanticipated carbon, such as carbon contamination in the beamline, frequently covers the gold mesh. As a result, the XAS signal is corrupted in its raw form. This signal can be corrected by calibrating with a signal of clean Au form. The

I_{gold} signal is the name for this signal. The raw data of a clean Au or I_{gold} signal is made up of two signals: the beamline background and the undesirable signal from gold mesh contamination. When the I_{gold} signal is removed from the background by the I_0 signal, the data of contaminants on the gold mesh is all that is left. As a result, all background in the raw XAS signal may be removed using double background subtraction, the first of which is background from the beamline and the second from the gold mesh. Where the signal is derived through double background subtraction and is referred to as $I_{double\ sub}$, Eq. (3.3) can be rewritten as:

$$I_{double\ sub} = \frac{\left(\frac{I_{sample}}{I_0}\right)}{\left(\frac{I_{gold}}{I_0}\right)} \quad (3.4)$$

The synchrotron flux has not been stable in general. Over time, it would gradually decline. When measuring multiple samples, each measurement took a varied amount of time. Synchrotron flux is used in a variety of ways in each experiment. The angle of the radiation beam falling on the monochromator may change over time, causing the photon energy to alter. As a result, the photon energy of signals taken at different times should be synchronized before background removal. Figure 3.16 shows the difference in photon energy of I_0 between clean gold and DLC sample. Shifting the X axis to correspond with the desired signal can be used to calibrate photon energy (all I signals should be shifted to the same position). The signals were then adjusted to allow comparison with other spectra in the last phase. Typically, the spectrum's pre-edge was set to 0 and the post-edge was set to 1. The XAS spectra processing scheme is shown below, step by step.

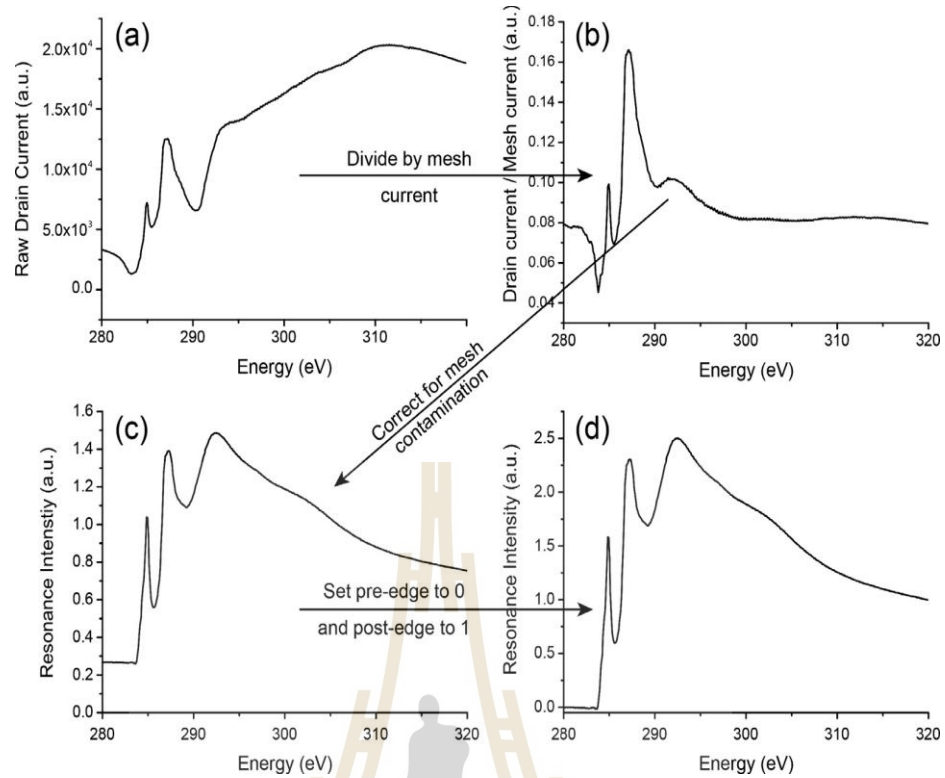


Figure 3.16 (a) Raw drain current spectrum. (b) the Mesh current corrects the spectrum. (c) the mesh's carbon contamination was removed from the spectra. (d) spectrum with the pre-edge (280 eV) and post-edge (320 eV) set to 0 and 1, respectively.

CHAPTER IV

RESULTS AND DISCUSSION

In this chapter, the thickness, homogeneity, bulk and surface resistivity of the DLC films prepared by various deposition time were examined. Different properties of the films were evaluated by the XPS and XAX analysis.

4.1 DLC films properties

4.1.1 DLC film thickness

A laser interferometer was used to measure the thickness of DLC films deposited for 10, 20, and 30 minutes, and the results were 44, 91, and 134 nm, respectively. Within time intervals, the thickness of the DLC films increases linearly with deposition time, showing a constant deposition rate of roughly 4.5 nm/min, as shown in figure 4.1.

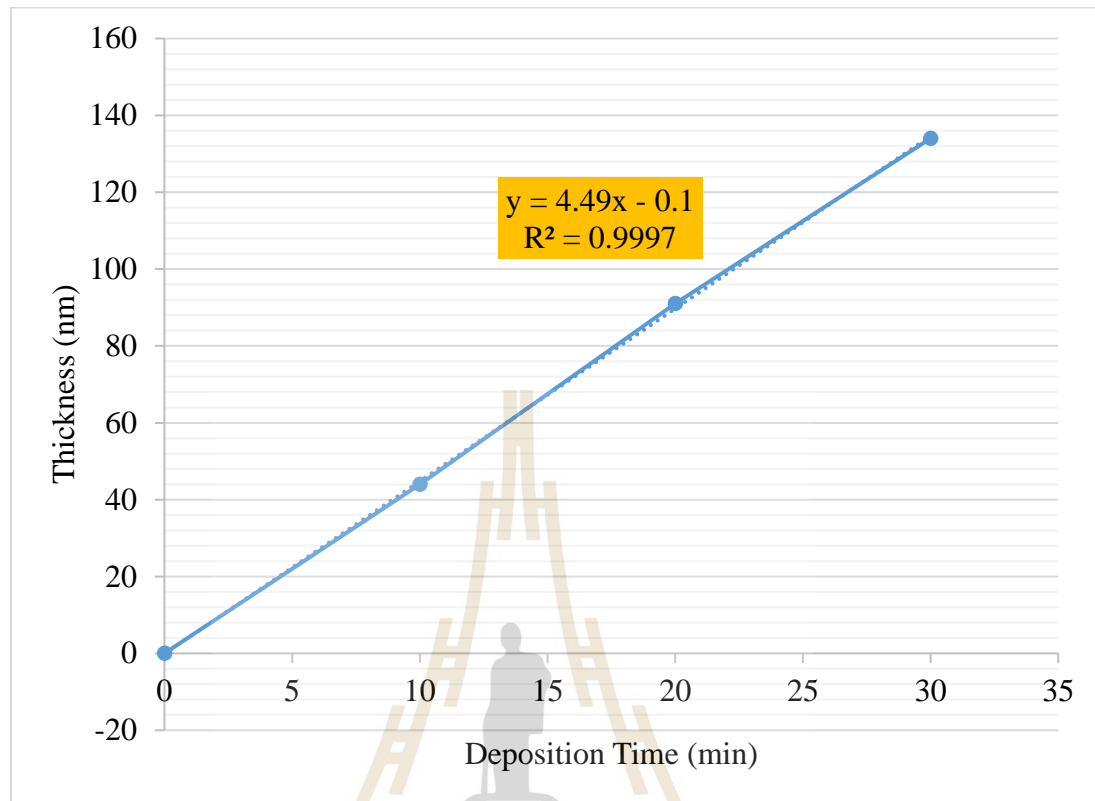


Figure 4.1 Deposition time versus thickness of films.

4.1.2 DLC films homogeneity

Figure 4.2 shows the SEM cross-sectional image of DLC-10 for the example.

It is seen that the DLC film is smooth and can be probed by the SEM technique. The thickness measured by this technique is in order of 500 nm. The thickness increases with depositing time.

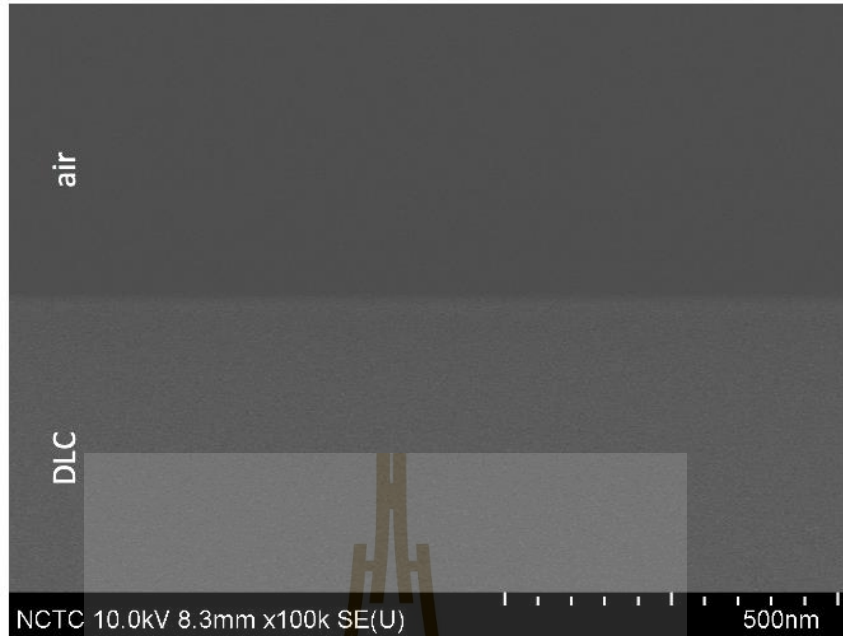


Figure 4.2 SEM cross-sectional image of DLC-10.

Figure 4.3 shows the thickness mapping of the DLC prepared with 20 mins and 40 mins deposition time, respectively. The color online indicates the thickness of each position varies from red (thickest) to blue (thinnest). Nine points were determined in one sample. As the deposit head was placed above and centre to the sample. The thickest region at the centre would be expected. The results in figure 4.3 perfectly confirm our assumption.

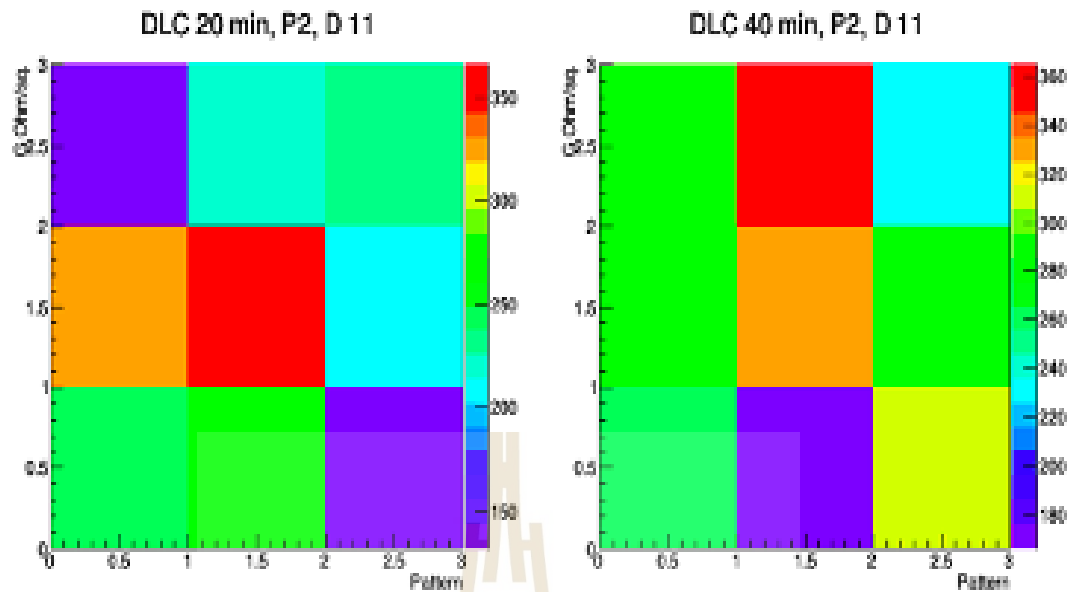


Figure 4.3 Thickness mapping of DLC film prepared at 20 and 40 mins deposit time.

4.2 DLC films resistivity

HiPIMS employed pure graphite as the objective for making DLC films. As substrates for DLC films, microscope slide glass with diameters of $1 \times 1 \text{ cm}^2$ and $2.5 \times 5 \text{ cm}^2$ were used. In an ultrasonic bath, the substrates were gently cleaned with ethanol and then DI water for 20 minutes each. The substrates were then N_2 gas-blow-dried. Chemical and structural characterizations were carried out on the small substrates, whereas electrical resistivity measurements were carried out on the larger ones.

HiPIMS deposited DLC thin films at a set average power of 110 Watts during deposition durations of 10, 20, and 30 minutes. The Ar gas flow rate was kept constant at 25 sccm. The working pressure was roughly 4.5 mTorr and the distance between the target and substrate was 60 mm. A laser interferometer was used to measure the thickness of the DLC films. The chemical composition of the films was determined using XPS and XAS techniques. For XPS measurements, monochromatized Al $\text{K}\alpha$ (1486.7 eV) was used as

the excitation. The Synchrotron Light Research Institute of Thailand's beamline 3.2b was used to conduct XAS measurements. [6]. The electrical resistance between the two ends of the patterned DLC films illustrated in figure 4.4 was measured using a mega-ohm electrometer. Using nitrogen vapor in a liquid nitrogen dewar, the temperature of the films may be regulated.

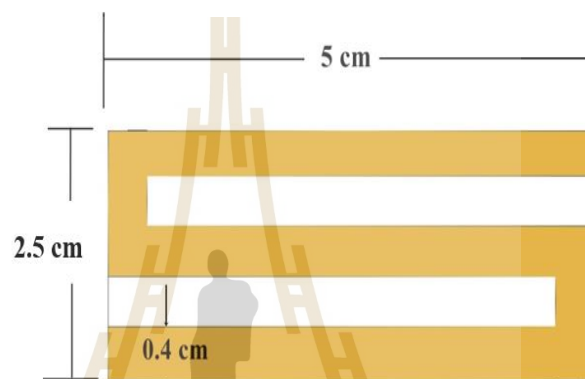


Figure 4.4. Electrical resistance measurements using patterned DLC coatings on glass.

4.2.1 DLC films resistivity at various thicknesses

The sheet resistivity (R_s) of the DLC films was estimated using a mega-ohm electrometer to measure the resistance (R) between both ends of the DLC strip. $R_s = \rho/t = RW/L$ is the relationship between sheet resistivity and resistance, where ρ is the resistivity and W , L , and t are the width, length, and thickness of the DLC films, respectively. Table 4.1 shows the sheet resistivity for three different DLC thicknesses. The thinnest sample has the highest sheet resistivity of $3.23 \text{ G}\Omega/\text{cm}^2$, which is similar to the previously reported value of $4 \text{ G}\Omega/\text{cm}^2$. The disparity in sheet resistivity for various DLC film thicknesses is detailed below, along with supporting XPS and XAS data.

Table 4.1 DLC film thickness, electrical resistance, and sheet resistivity.

Samples ID	Deposition time (min)	Thickness (nm)	Resistance (M Ω)	Resistivity (Ω -cm)	Sheet Resistivity (G Ω /cm ²)
DLC10	10	44	12.74	142.08	3.23
DLC20	20	91	1.33	30.26	0.33
DLC30	30	134	1.39	55.03	0.41

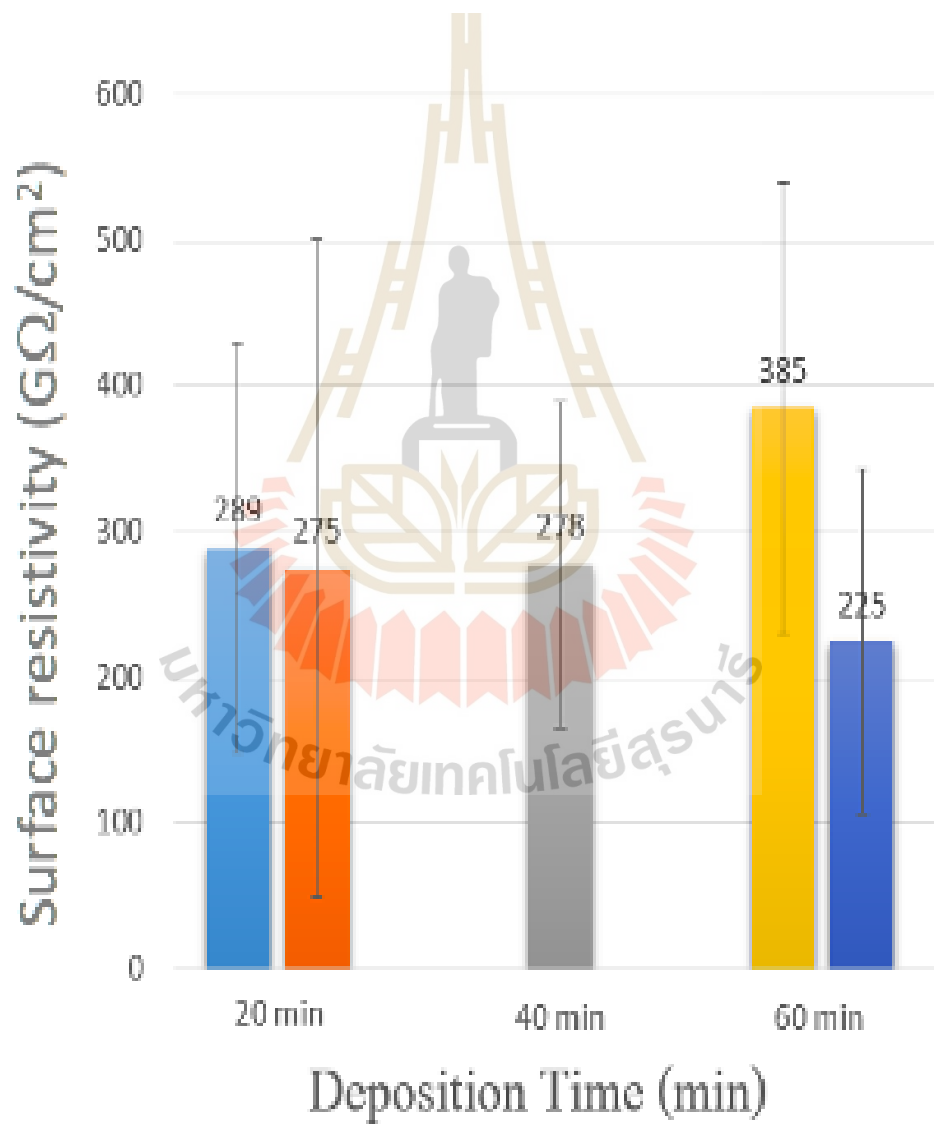
**Figure 4.5** Surface resistivity as a function of deposit time.

Figure 4.6 shows relation in three dimension of deposition time, thickness and surface (sheet) resistivity of DLC films at 10, 20 and 30 min. Sheet resistivity or surface resistivity of in a $G\Omega/cm^2$ range can be obtained. Deposition time increase, thickness increase with related bulk DLC. So, DLC films can be deposited on glass substrates by using HiPIMS with a linear deposition rate.

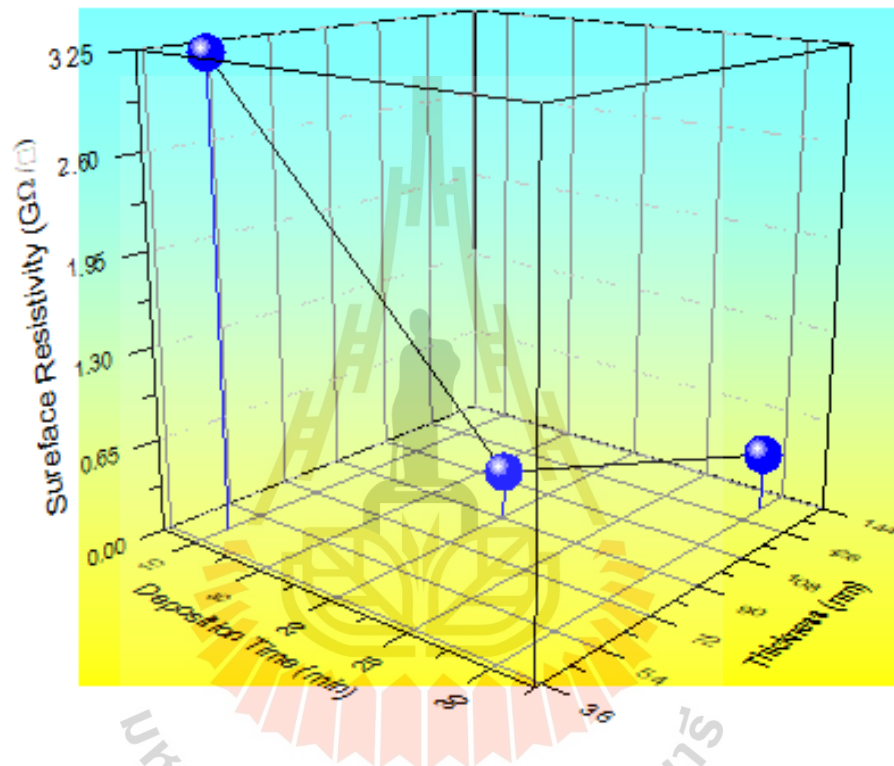


Figure 4.6 Three-dimension: Deposition time, thickness and surface (sheet) resistivity of DLC films at 10, 20 and 30 min.

4.2.2 DLC Films resistivity as a function of growing position

The resistivity was measured along the horizontal line of the prepared films. Figure 4.7 shows the line scan of resistivity of the same samples as shown in Figure 4.3. It is seen that most of the resistivity of the DLC 20 mins lies between 140 to 360 $G\Omega/cm^2$ while the DLC-40 have higher resistivity which is around 160 to 380 $G\Omega/cm^2$. This shows

that 1) the samples are not homogeneous 2) the higher deposit time the higher resistivity. So, the centre position of each films was choose the be characterized in the next section.

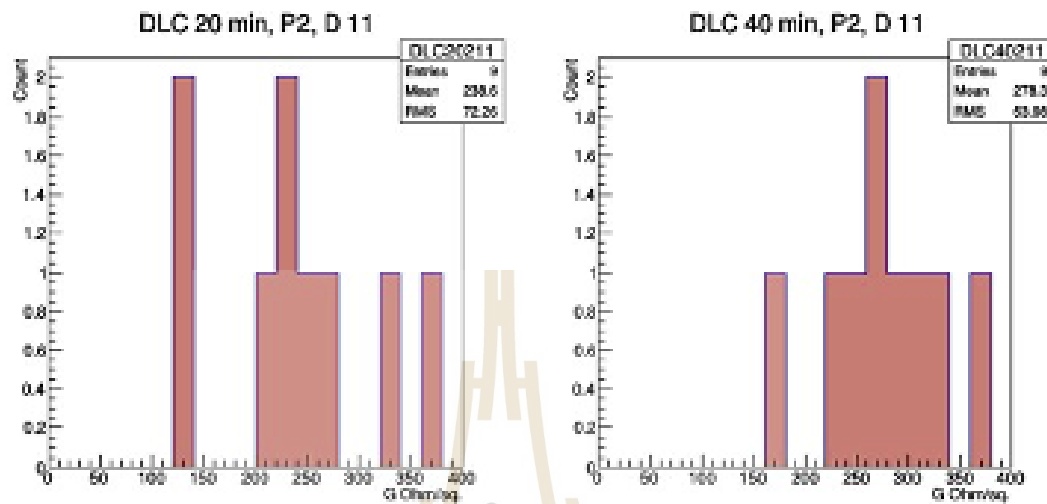


Figure 4.7 Thickness ad resistivity relationship of the DLC films prepared at 20 and 40 mins deposition time.

4.2.3 DLC resistivity as a function of temperature

The resistance measured between both ends of the DLC strip as a function of temperature of the DLC-10 sample is shown in Figure 4.8. It was discovered that when the temperature drops, the resistance increases exponentially, which is consistent with prior research [7]. At -165 °C, the resistance is 334 MΩ.

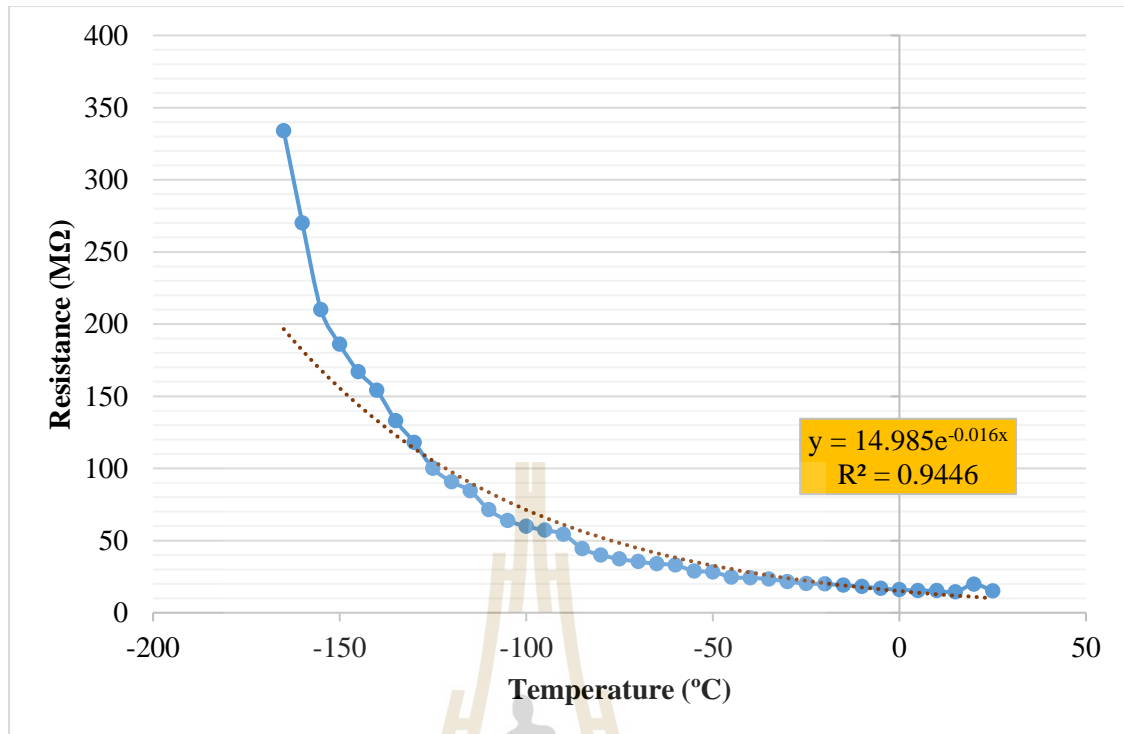


Figure 4.8 Temperature versus resistance in liquid nitrogen environment.

4.3 Raman spectroscopy results on DLC films

Raman spectroscopy was used to investigate the bonding behavior of the DLC produced by the sputtering technique. This approach can be used to calculate the ratio of diamond-like (sp^3) to amorphous bonding (sp^2). Raman spectroscopy investigates vibrational modes in a material using the Raman shift; phonon vibrations are particular to the bonds present. A Raman shift occurs when light is scattered inelastically with vibrational modes, changing the wavelength of laser light somewhat (Raman shifted). The background reflected light is eliminated via gratings, and the Raman shift is plotted against relative intensity to provide a spectrum. Because sp^2 sites are substantially resonant and so dominate the spectrum, visible Raman spectroscopy of diamond-like carbon cannot directly investigate the sp^3 bonding prominence. On the other hand, the relative intensities

of the so-called D and G peaks have been shown to be indicative of sp^3 content. (Ferrari et al., 2000).

The spectra were fitted to Gaussian approximations using a 532 nm excitation light source, allowing the area under the D and G peaks to be compared. The so-called D peak, which occurs at around 1365 cm^{-1} and is caused by graphitic-like rings breathing, occurs only where the graphite rings have room to expand and does not exist in continuous sheets of graphitic rings. The G peak, which is around 1536 cm^{-1} and occurs at all sp^2 sites since it does not require the presence of 6-fold graphite rings, is another notable peak. With increasing disorder, ID (integrated intensity) rises from graphitic dominating carbon to nano-crystalline graphite and amorphous carbon. IG has a relatively constant intensity, but its relative wavenumber position goes through a two-stage process. With increased bond disorder, the peak location shifts to lower wavenumbers, but returns to higher wavenumbers when sp^3 chains are formed. The sp^3 to sp^2 ratio may be accurately calculated using these two markers (Ferrari et al., 2004).

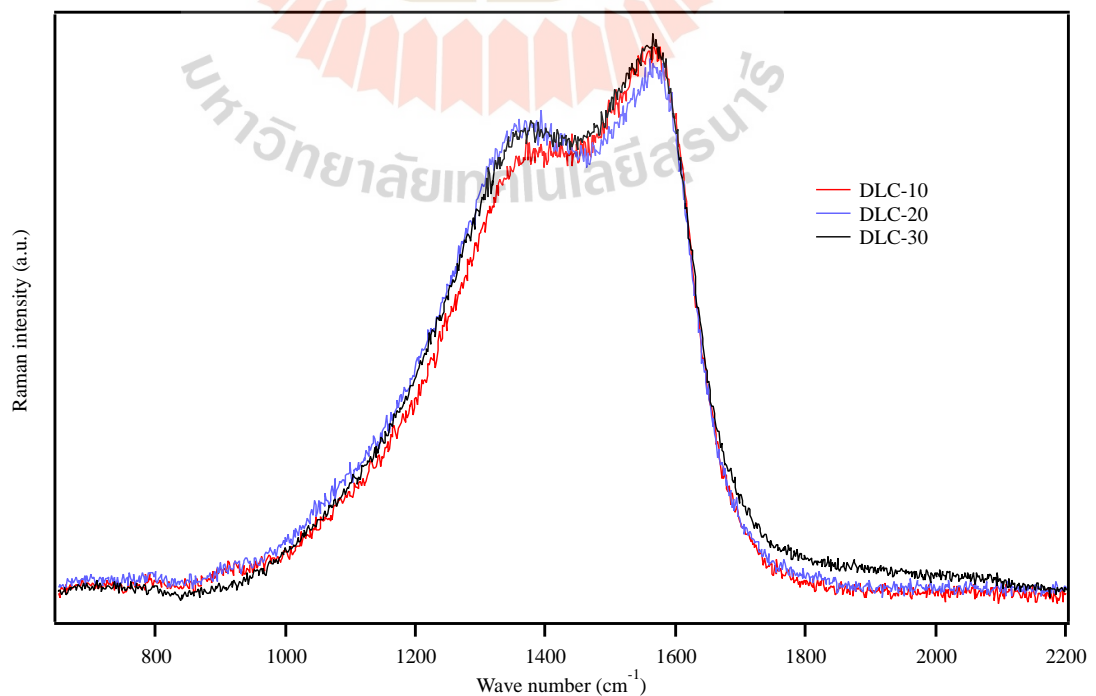


Figure 4.9 Raman spectra of the DLC-10, DLC-20 and DLC-30.

Figure 4.9 shows the Raman spectra of the DLC sputtered at 10, 20 and 30 mins, respectively. Two peaks were clearly seen in all spectra which located at the position around 1390 and 1570 cm^{-1} . This is slightly shifted from the expected D and G peaks as reported earlier which may be due to the experimental setup. Despite of such systematic error, the analysis could still be processed. As shown in Figure 4.9 The example fitting of DLC-10 was shown. The D and G peaks were indicated by green and red curves, respectively.

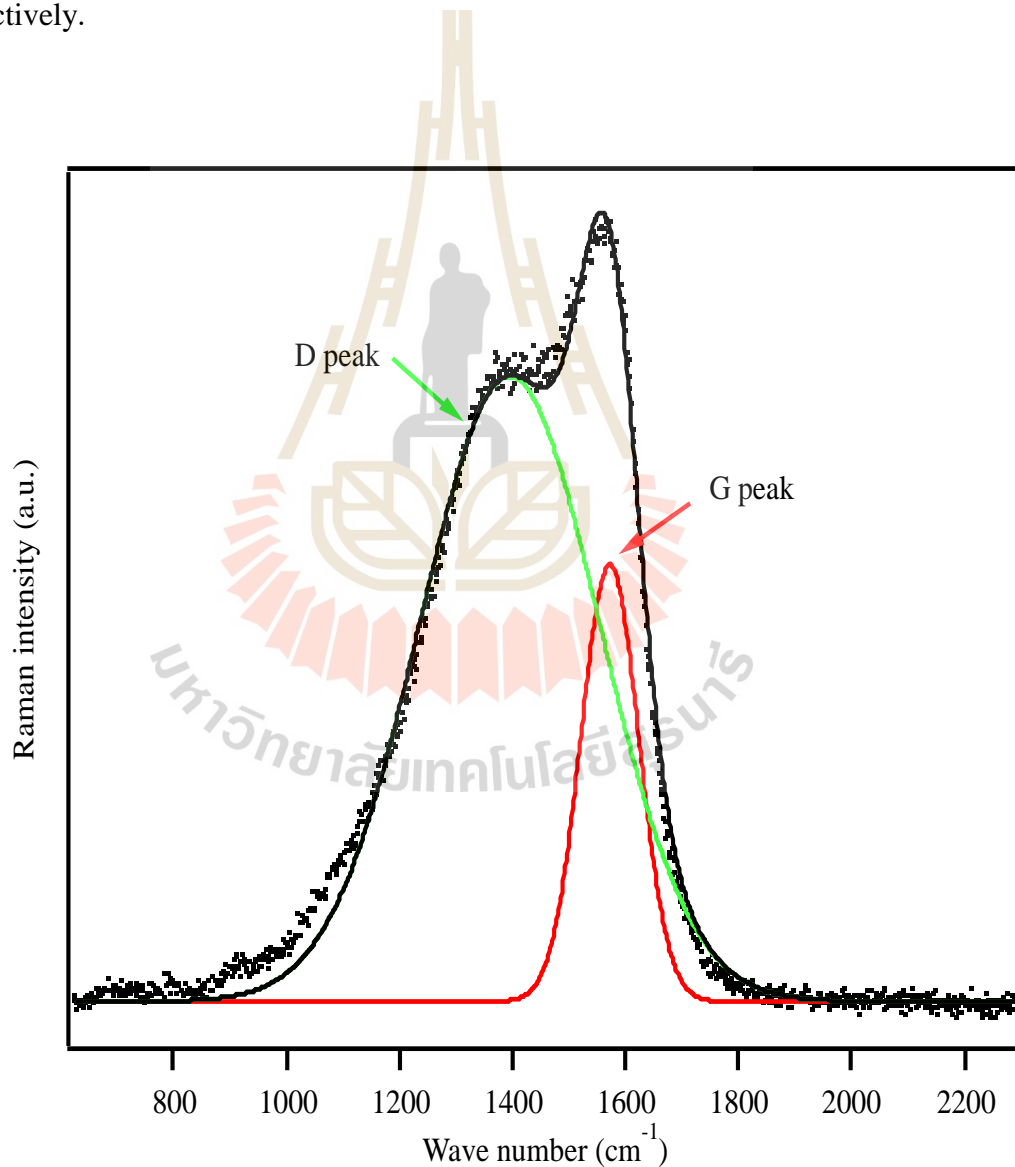


Figure 4.10 Raman spectrum of DLC-10 indicates the G and D peaks fitting.

All spectra were computed where the results were summarized in table 4. x. It is clearly seen that the D peak position decreases from 1393.3 to 1386.3 cm^{-1} at the deposition increase from 10 to 20 mins. The D peak position located at similar position from the DLC-30. This is in contrast to the G peaks were their position increases in the DLC-20. The I_D/I_G are 4.44, 5.76 and 4.36 for DLC-10, DLC-20 and DLC-30, respectively. This is in agreement with the Resistivity measured above where the DLC-20 is the best among these samples.

Table 4.2 Raman spectra fitting parameters.

Samples	Dep.	D peak	G peak	I_D/I_G
	Time(min)	position (cm^{-1})	position (cm^{-1})	
DLC-10	10	1393.3	1570.6	4.44
DLC-20	20	1386.3	1573.9	5.76
DLC-30	30	1386.0	1573.3	4.36

4.4 XPS results on DLC films

A photoelectron spectra of C 1s collected from a DLC film with a 10-minute coating duration is shown in Figure 4. 11. The C 1s peak was deconvoluted into four separate peaks, each representing a different carbon species. Coskun group used to assign the four peaks (Coskun et al., 2015). The photoelectrons originating from the sp^2 -C and sp^3 -C species are responsible for the first two prominent peaks, which are positioned at 284.7 and 285.5 eV, respectively. The peaks at 286.9 eV (C–O) and 288.5 eV (C=O), respectively, are photoelectrons from carbon atoms bound to an oxygen atom with single and double bonds. Surface contamination produces the carbon species with the maximum binding energy, i. e. carbon double bonded with oxygen (C=O). Table 4.2 shows the findings of C 1s XPS peak fitting. The sp^3 hybridized carbon content is highest in the

thinnest layer, i.e. the film with the shortest deposition period, according to the XPS results. With increasing deposition time, a decrease in sp^3 content and an increase in sp^2 content were observed. With increasing deposition time, a decrease in sp^3 content and an increase in sp^2 content were observed. Longer deposition times result in increased energy dissipation, creating more stress in the depositing film, and incident carbon ions prefer to create sp^2 bonded hybridizations rather than sp^3 carbon sites (Huang et al., 2012)

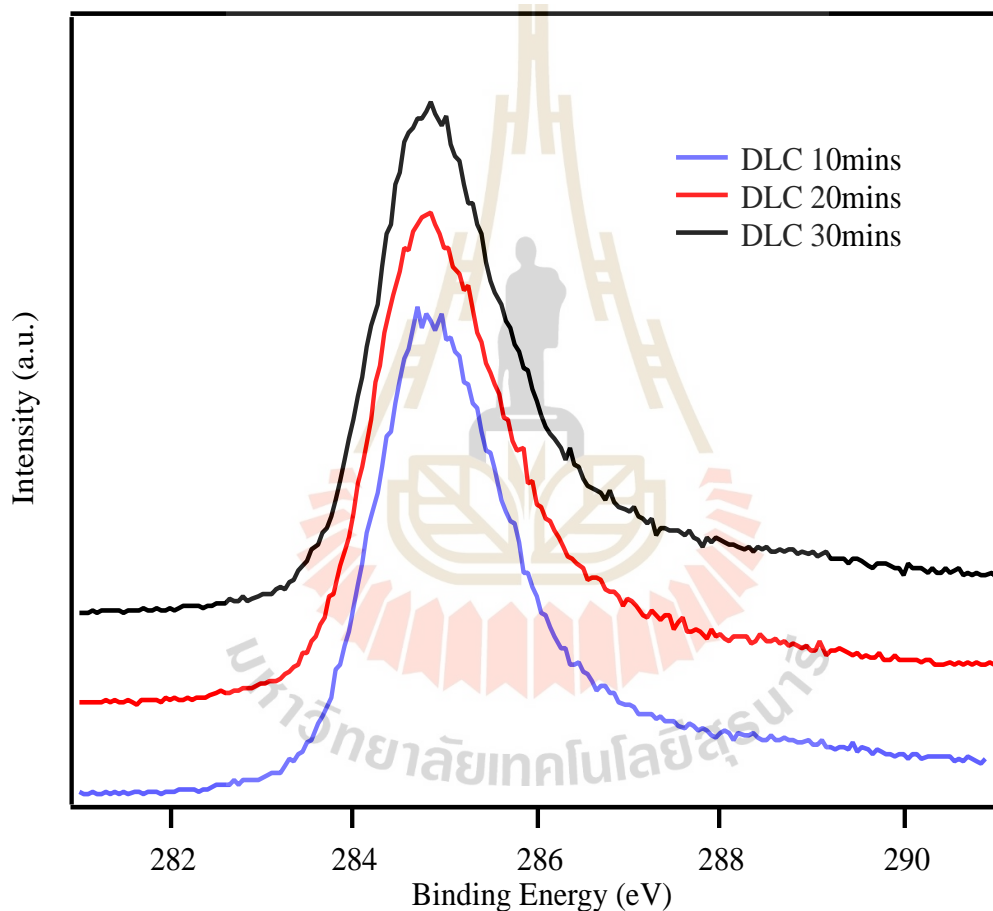


Figure 4.11 C 1s XPS spectrum taken from the DLC-10, DLC-20 and DLC-30.

The C 1s XPS peak from the DLC film is shown in Figure 4.12. Background subtraction and Voigt function fitting were used to deconvolute the XPS spectra. Chemical states of amorphous carbon films are typically identified using C 1s peaks in the XPS spectrum. The DLC film's C 1s spectrum was divided into four sub-peaks with locations

of 284.5, 285.1, 286.8, and 288.4 eV, respectively (Zhang et al., 2018). The graphitic structure (sp^2 carbon (C=C)) and the diamond structure (sp^3 carbon (C-C)) have C 1s peaks around 284.5 and 285.1 eV, respectively (Ronning et al., 1998). The sp^3 configuration has a lower proportion than the sp^2 configuration, as shown in the diagram. Due to film contamination from exposure to the atmosphere, two extra C species occur in the C 1s XPS spectra, which are attributed to C-O, C=O, and O-C=O bonds (Alawajji et al., 2018).

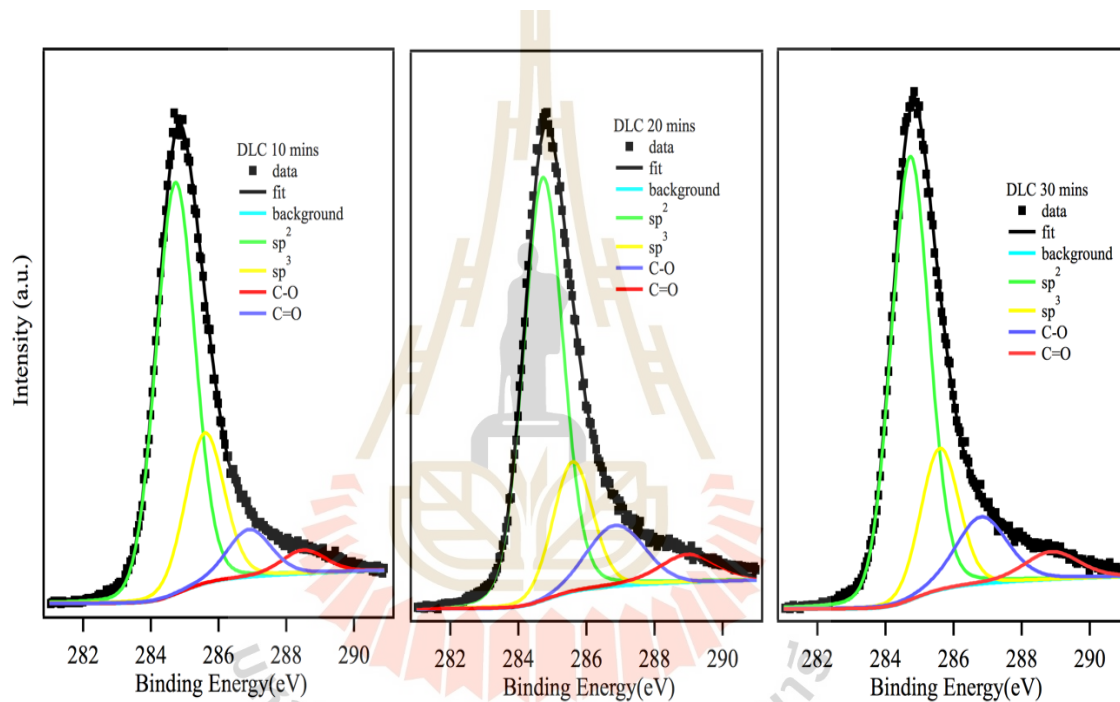


Figure 4.12 Deconvolution of the C1s XPS spectrum of the DLC-10, DLC-20 and DLC-30 prepared by HiPIMS.

Table 4.3 Peak positions, regions under the peak, and the $sp^3:sp^2$ ratio for DLC films with varying deposition durations were determined by deconvolution of the XPS C 1s spectra.

Samples ID	Peak position (eV)				Area (cps·eV)				$sp^3:sp^2$
	sp^2 -C	sp^3 -C	C-O	C=O	sp^2 -C	sp^3 -C	C-O	C=O	
DLC10	284.7	285.5	286.9	288.5	13407	4973	1829	908	1:2.7
DLC20	284.7	285.5	286.8	288.9	14255	4361	2794	1492	1:3.3
DLC30	284.7	285.5	286.8	288.8	14293	4482	3096	1350	1:3.2

4.5 XAS results on DLC films

The normalized C K-edge XANES spectra of DLC films produced by HiPIMS with varied deposition durations are shown in Figure 4.13. The three samples exhibit distinct characteristics in the photon energy range of 283 – 291 eV. This is owing to the fact that the three DLC films contain varying proportions of distinct carbon species. The sp^2 hybridized carbon atoms (or the π^* bond of C=C) are responsible for the feature showing as a peak at photon energy of 284.7 eV in the thickest layer, DLC-30. Another notable aspect of the thinnest DLC film, DLC10, is the peak at roughly 287.7 eV photon energy. The existence of the σ^* bond between carbon and hydrogen atoms is the fundamental reason of this property (Ohmagari et al., 2009). According to one report, the C=O π^* bond should also be seen as a characteristic in the 288-290 eV range (Ray et al., 2004). Some hydrocarbons in the deposition system may be included in the film, in addition to surface pollution (Tunmee et al., 2015). The hydrogen content of the film, as determined by XANES spectra, has a significant impact on its resistivity. The resistivity of DLC films appears to increase with hydrogen concentration. The resistivity as a function of hydrogen concentration will need to be studied further.

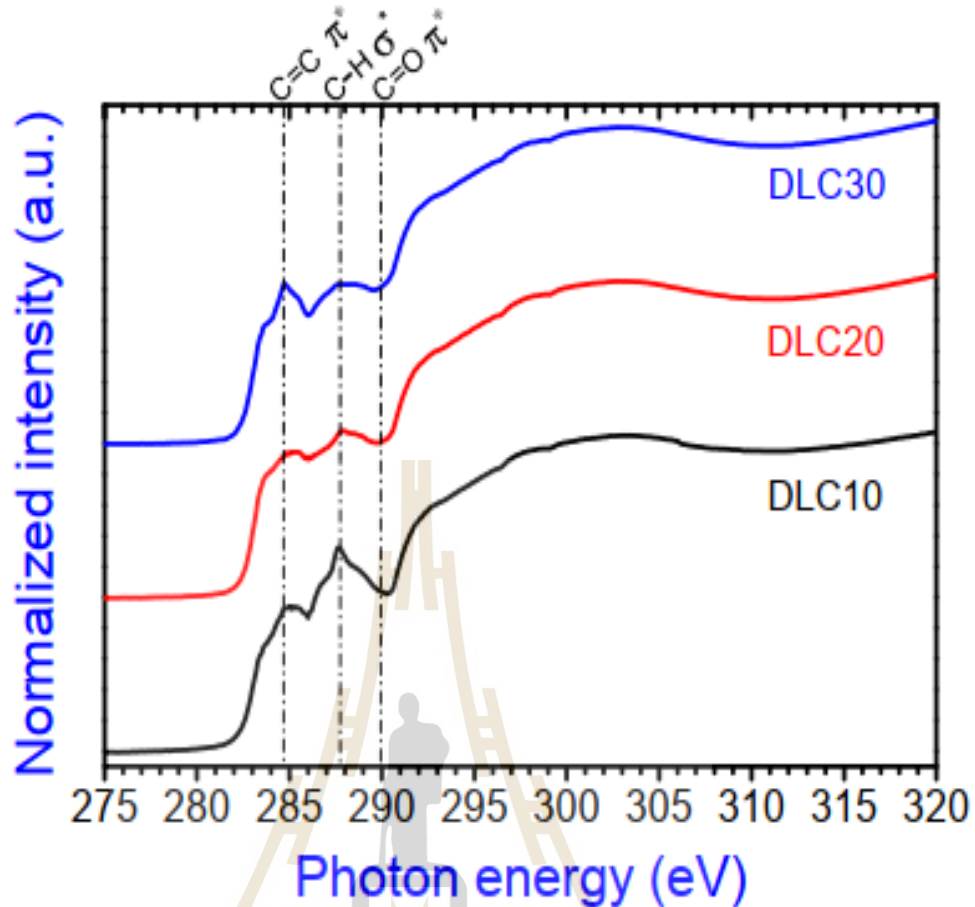


Figure 4.13 DLC films with three different coating times with normalized C K-edge XANES spectra.

The normalized C K-edge XANES spectra of the DLC film and curve fitting are shown in Figure 4.15. Curve fitting was used to deconvolute the observed spectra, yielding the Gaussian transition peaks (from 1s to permitted orbitals) and the ionization step function. The peaks at 284.8 eV and 292.2 eV, which correspond to the π^* and σ^* bands, are typical of the C=C bond (sp^2) and the tetrahedral C-C bond (sp^3), respectively (Ray et al., 2004). Other peaks come from other carbon species: ketone/aldehyde (σ^* C - H) at 286.7 eV, carboxyl carbon (C = O(OH)) at 288.7 eV, Cls of σ^* C-C at 293.5 eV, Cls of σ^* C=C at 300 eV, and Cls 1 and σ^*_2 of O=C-OH at 296.6 and 303.5 eV, respectively (Jaouen et al., 1995).

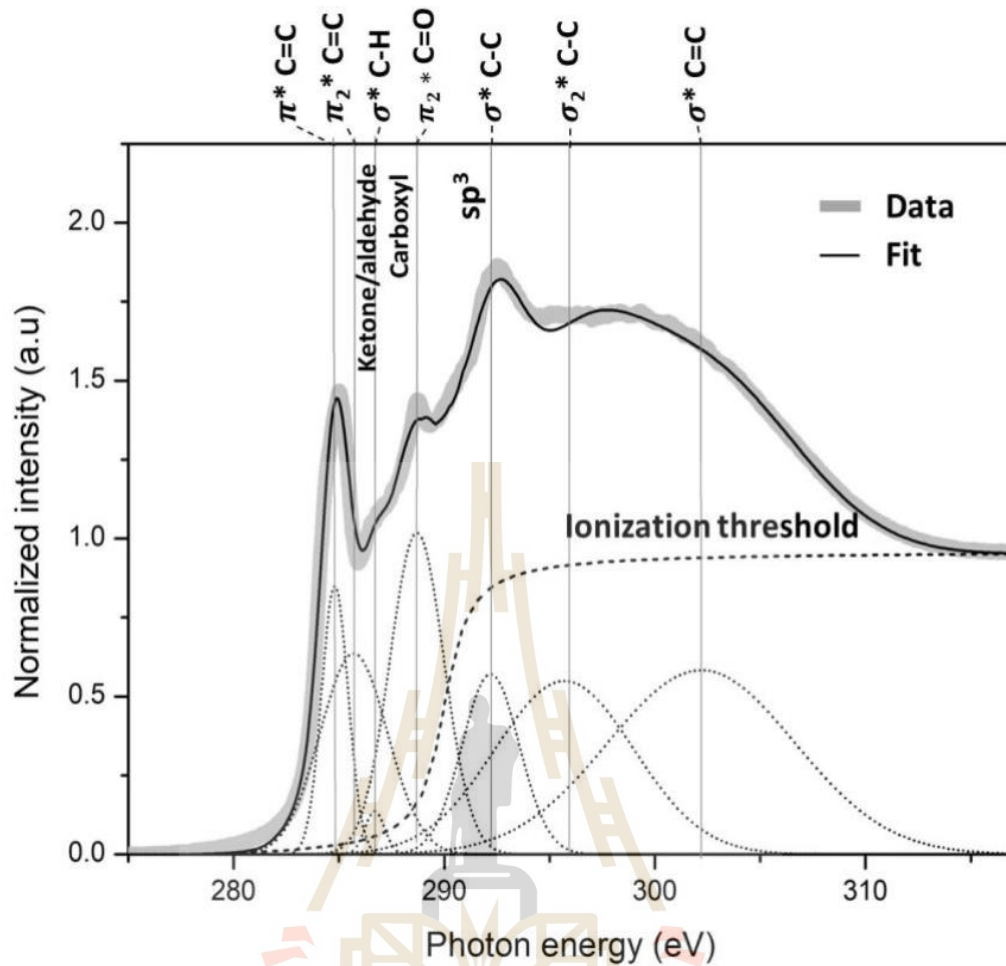


Figure 4.14 DLC films' Normalized C K-edge XANES spectra using curve fitting.

Both techniques show that there is more carbon in the sp^2 configuration in the DLC film than in the sp^3 configuration. DLC has a sp^2/sp^3 ratio of about 1.7, according to XPS analysis. This result is little lower than 2.0, which was acquired by XAS analysis. The sp^2 to sp^3 ratio disparity could be related to changes in probed depth. Because XPS is more surface sensitive than XAS, XPS spectra may contain surface contamination information, resulting in erroneous data reduction. This could be a topic for additional research, especially if surface contamination needs to be removed.

CHAPTER V

CONCLUSIONS

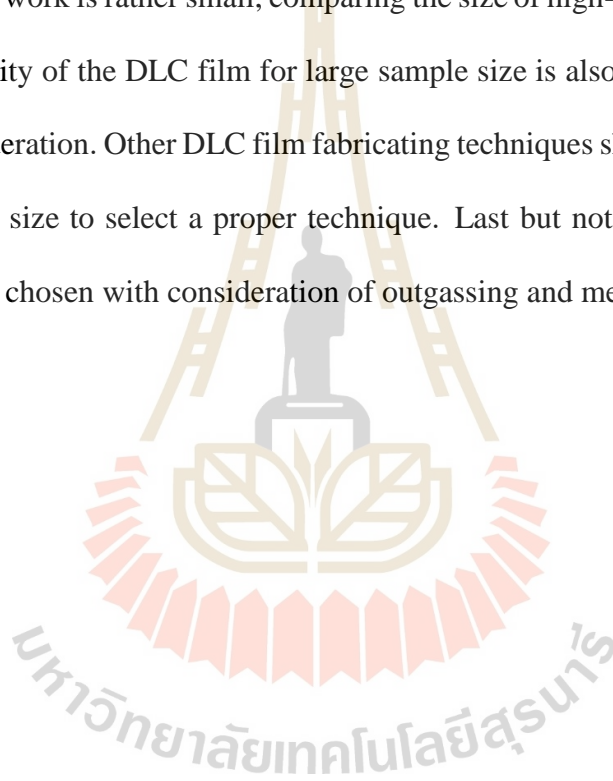
In this thesis work, a simple home-made HiPIMS thin film deposition system was employed to fabricate DLC films. The resistivity of the DLC films at room and low temperatures were measured to justify the feasibility to be used as electrode materials for particle detectors. The chemical composition of the films was also investigated by XPS and XAS techniques to establish the correlation with the measured resistivity.

It was demonstrated that DLC films could be deposited at a consistent and controllable rate using the HiPIMS deposition technique. It was found that the contamination, particularly hydrocarbons in the deposition system, affects the electrical properties of the films. The resistivity of the DLC coating is increased by the presence of hydrogen. This finding suggests a possibility to adjust the resistivity of DLC films by controlling the amount of hydrogen in the films. At liquid Xe temperatures, the resistivity of DLC films was found to be as high as hundreds of giga-ohm suggesting that DLC films could be employed as a large area resistive surface for electrodes in nuclear and particle physics detectors.

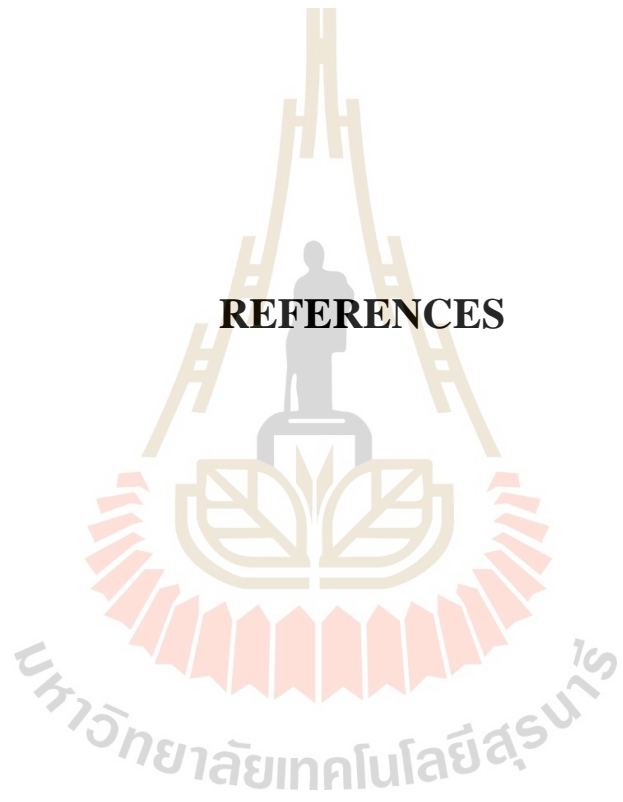
The XPS and XAS techniques were employed to investigate the composition of the DLC films. The results obtained from both methods suggest that the DLC films contain more sp^2 carbon than sp^3 carbon. However, the two techniques yield different sp^2/sp^3 ratio. This could be owing to the fact that the two approaches probe samples at different depths. It is well-known that XPS is a rather surface-sensitive technique, most of the information was from the surface atomic layers. It is found that the sp^2/sp^3 ratio obtained from XPS is

higher than that obtained from XAS, indicating that more sp^2 content is at the surface region of the DLC films.

This thesis suggests that DLC is a potential candidate as a resistive material for fabricating a large area resistive surface for electrodes in high energy particle detectors. More research is needed for better understanding of how hydrogen can be used to control the resistivity of DLC films. It is important to note that the dimensions of DLC films fabricated in this work is rather small, comparing the size of high-energy particle detectors. Thus, homogeneity of the DLC film for large sample size is also crucial and that must be taken into consideration. Other DLC film fabricating techniques shall also be experimented for large sample size to select a proper technique. Last but not least, a proper substrate material shall be chosen with consideration of outgassing and mechanical strength.



REFERENCES



REFERENCES

- Alawajji, R. A., Kannarpady, G. K., Nima, Z. A., Kelly, N., Watanabe, F. and Biris, A. S. (2018). Electrical properties of multilayer (DLC-TiC) films produced by pulsed laser deposition. **Applied Surface Science**. 437: 429.
- Anders, A. (2017). Tutorial: Reactive high-power impulse magnetron sputtering (R-HiPIMS). **Japanese Journal of Applied Physics**. 121: 171101.
- Balandin, A. A. (2011). Thermal properties of graphene and nanostructured carbon materials. **Nature Materials**. 10: 569.
- Bewilogua, K. and Hofmann, D. (2014). History of diamond-like carbon films — From first experiments to worldwide applications. **Surface and Coating Technology**. 242: 214.
- Biesinger, M. C. (2018). Depth of Analysis, Inelastic Mean Free Path (on-line). Available at <http://www.xpsfitting.com/2012/08/depth-of-analysis-inelastic-mean-free.html>
- Chachiyo, T. and Chachiyo, H. (2020). Understanding electron correlation energy through density functional theory. **Computational and Theoretical Chemistry**. 1172: 112669.
- Chaiyabin P., Giboni K. L., Han K., Ji X., Juyal P., Kobdaj C., Liu J., Lomon J., Pasaja N., Poolcharuansin P., Rujirawat S., Songsiriritthigul P., Yan Y. and Zhaoa L. (2017). Novel field cage design for the PandaX-III double beta decay experiment. **Journal of Instrumentation**. 12: 10014.

- Charitidis, C. A. Koumoulos, E. P. and Dragatogiannis, D. A. (2013). Nanotribological Behavior of Carbon Based Thin Films: Friction and Lubricity Mechanisms at the Nanoscale. **Lubricants**. 1: 22.
- Cheng, Q., Tam, E., Xu, S. and Ostrikov, K. (2010). Si quantum dots embedded in an amorphous SiC matrix: nanophase control by non-equilibrium plasma hydrogenation. **Nanoscale**. 2: 594.
- Coşkun, O. D. and Zerrin, T. (2015). Optical, structural and bonding properties of diamond-like amorphous carbon films deposited by DC magnetron sputtering. **Diamond and Related Materials**. 56: 29.
- Ferrari, A. C. and Robertson, J. (2000). Interpretation of Raman spectra of disordered and amorphous carbon, **Physical Review B**. 61: 14095.
- Ferrari A. C. and Robertson, J. (2004). Raman spectroscopy of amorphous, nanostructured, diamond-like carbon, and nanodiamond. **American Physical Society**. 61: 96.
- Huang, Y., Wang, Q., Wang, M., Fei, Z. and Li, M. (2012). Characterization and analysis of DLC films with different thickness deposited by RF magnetron PECVD. **Rare Metals**. 31: 198.
- Jaouen, M., Tourillon, G., Delafond, J., Junqua, N. and Hug, G. (1995). A NEXAFS characterization of ion-beam-assisted carbon-sputtered thin films. **Diamond Relat Mater**. 4: 200.
- Kimura, T., Kamata, H., Nakao, S. and Azuma, K. (2016). Preparation of Titanium-Doped Diamond-Like Carbon Films With Electrical Conductivity Using High Power Pulsed Magnetron Sputtering System With Bipolar Pulse Voltage Source for Substrate. **IEEE Transactions on Plasma Science**. 44: 12.
- Lenhart, J. L., Fischer, D. A., Sambasivan, S., Lin, E. K., Jones, R. L., Soles, C. L., Wu, W., Goldfarb, D. L. and Angelopoulos, M. (2005). X-ray Absorption Spectroscopy

- to Probe Surface Composition and Surface Deprotection in Photoresist Films. **Langmuir**. 21: 4007.
- Liao, Z., Jiang, P., Zhong, Z. and Li, R.-W. (2020). Materials with strong spin-textured bands. **npj Quantum Materials**. 5: 30.
- Liu, D., Li, X., Chen, S., Yan, H., Wang, C., Wu, C., Haleem, Y. A., Duan, S., Lu, J., Ge, B., Ajayan, P. M., Luo, Y., Jiang, J. and Song, L. (2019). Atomically dispersed platinum supported on curved carbon supports for efficient electrocatalytic hydrogen evolution. **Nat Energy**. 4: 512.
- Merel, P., Tabbal, M., Chaker, M., Moisa, S. and Margot, J. (1998). Direct evaluation of the sp³ content in diamond-like-carbon films by XPS. **Applied Surface Science**. 136: 105.
- Mohai, M. (2000). The mean free path [on-line]. Available at [http:// www.lasurface.com/xps/imfp.php](http://www.lasurface.com/xps/imfp.php)
- Moriguchi, H., Ohara, H. and Tsujioka, M. (2016). History and Applications of Diamond-Like Carbon Manufacturing Processes., **SEI Technical Review**. 82: 52.
- Ochi, A., Homma, Y., Yamazaki, Y., Yamane, F., Takemoto, T., Kawamoto, T., Kataoka, Y., Masubuchi, T., Kawanishi, Y. and Terao, S. (2014). Carbon Sputtering Technology for MPGD detectors. **PoS**. 351.
- Ohmagari, S., Yoshitake, T., Nagano, A., AL-Riyami, S., Ohtani, R., Setoyama, H., Kobayashi, E. and Nagayama, K. (2009). Near-Edge X-Ray Absorption Fine Structure of Ultrananocrystalline Diamond/ Hydrogenated Amorphous Carbon Films Prepared by Pulsed Laser Deposition. **Journal of Nanomaterials**. 2009: 876561.
- Paul, B., Simon, J. and Martin, V. (2006). Properties of Synchrotron Radiation [on-line]. Available: <http://pd.chem.ucl.ac.uk/pdnn/inst2/prop.htm>

- Panda, P. K., Grigoriev, A., Mishra, Y. K., and Ahuja, R. (2020). Progress in supercapacitors: roles of two dimensional nanotubular materials. **Nanoscale Advances**. 2: 70.
- Poolcharuansin P., Estrin F. L. and Bradley J. W. (2015). The use of segmented cathodes to determine the spoke current density distribution in high power impulse magnetron sputtering plasmas. **Japanese Journal of Applied Physics**. 117: 163304.
- Pop, E., Varshney, V. and Roy, A. K. (2012). Thermal properties of graphene: Fundamentals and applications. **MRS Bulletin**. 37: 1273.
- Quiros, C., Soriano, L. Gomez, J. G., Palomares, F. J., Elizalde, E., Bressler, P. R., and Sanz, J.M. (1999). XAS and XPS study of amorphous carbon nitride films. *Bessy Jahresbericht 1999*. (Annual report 1999 of the Berliner Elektronenspeicherring-Gesellschaft fuer Synchrotron strahlung (BESSY)).
- Ray, S. C., Tsai, H. M., Chiou, J. W., Bose, B., Jan, J. C., Kumar, K., Pong, W. F., Dasgupta, D. and Tsai, M.-H. (2004). X-ray absorption spectroscopy (XAS) study of dip deposited a-C:H(OH) thin films. **Journal of Physics: Condensed Matter**. 16: 5713.
- Raúl, B. (2000). Electron-surface interactions [on-line]. Available at https://www2.Virginia.edu/ep/SurfaceScience/electron_interactions.htm
- Ronning, C., Feldermann, H., Merk, R., Hofsass, H., Reinke, P. and Thiele, J. U. (1998). Carbon nitride deposited using energetic species: A review on XPS studies. **Physical Review B: Condensed Matter**. 58: 2207.
- Sainio, S., Nordlund, D., Caro, M. A., Gandhiraman, R., Koehne, J., Wester, N., Koskinen, J., Meyyappan, M. and Laurila, T. (2016). Correlation between sp³-to-sp² Ratio and Surface Oxygen Functionalities in Tetrahedral Amorphous Carbon (ta-C) Thin

Film Electrodes and Implications of Their Electrochemical Properties. **Journal of Physical Chemistry C**. 120: 8298.

Shinya, O., Tsuyoshi, Y., Akira, N., Sausan, A.-R., Ryota, O., Hiroyuki, S., Eiichi, K. and Kunihiro, N. (2009). Near- Edge X- Ray Absorption Fine Structure of Ultrananocrystalline Diamond/Hydrogenated Amorphous Carbon Films Prepared by Pulsed Laser Deposition. **Journal of Nanomaterials**. 876561: 5.

Sikora, A., Bourgeois, O., Sanchez-Lopez, J. C., Rouzaud, J.-N., Rojas, T. C., Loir, A.-S., Garden, J. L., Garrelie, F. and Donnet, C. (2009). Effect of boron incorporation on the structure and electrical properties of diamond-like carbon films deposited by femtosecond and nanosecond pulsed laser ablation. **Thin Solid Films**. 518: 1470.

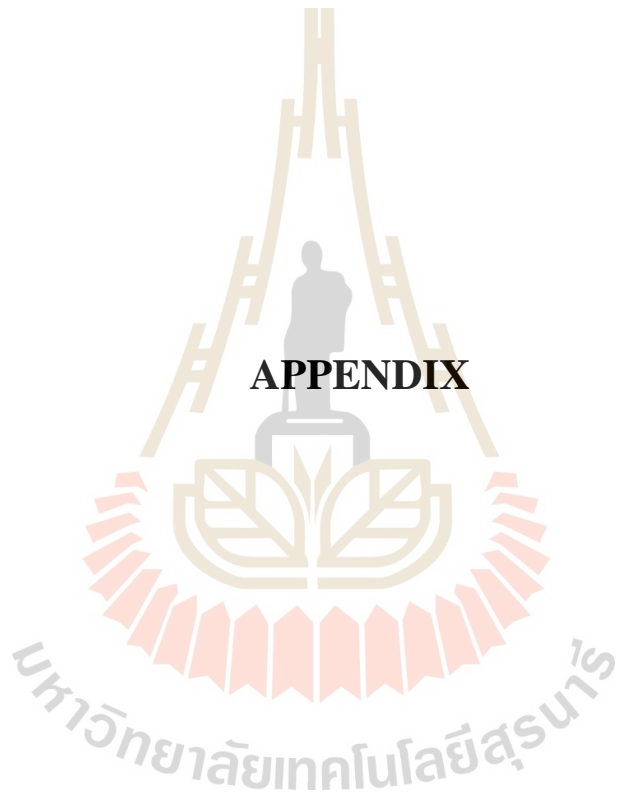
Steinberger, R., Celedón, C. E., Bruckner, B., Roth, D., Duchoslav, J., Arndt, M., Kurnsteiner, P., Steck, T., Faderl, J., Riener, C. K., Angeli, G. and Bauer, P. (2017). Oxygen accumulation on metal surfaces investigated by XPS, AES and LEIS, an issue for sputter depth profiling under UHV conditions. **Applied Surface Science**. 411: 189.

Stöhr, J. (1992). NEXAFS Spectroscopy. Springer Series in Surface Science. Springer Verlag, Berlin. 25.

Tanaka, Y., Miyake, K. and Saito, A. (2019). Diamond-like Carbon Film for Bearing Parts and Its Mass Production Technology, **SEI Technical Review**. 88.

Tunmee, S., Supruangnet, R., Nakajima, H., Zhou, X. L., Arakawa, S., Suzuki, T., Kanda, K., Ito, H., Komatsu, K. and Saitoh, H. (2015). Study of synchrotron radiation near-edge X-ray absorption fine-structure of amorphous hydrogenated carbon films at various thicknesses. **Journal of Nanomaterials**. 16: 414.

- Usman, A., Rafique, M. S., Shaukat, S. F., Siraj, K., Ashfaq, A., Anjum, S., Imran, M. and Sattar, A. (2016). Impact of Argon gas on optical and electrical properties of Carbon thin films. **Physica B: Condensed Matter**. 503: 157.
- Wilson, E. J. N. (1996). Fifty Years of Synchrotrons. CERN, Geneva, Switzerland. Conference proceeding.
- Yuan, Q., Lin, C.-T. and Chee, K. W. A. (2019). All-carbon devices based on sp²-on-sp³ configuration. **APL Materials**. 7: 030901.
- Zemek, J., Jiricek, P., Houdkova, J., Artemenko, A. and Jelinek, M. (2016). Diamond-like carbon and nanocrystalline diamond film surfaces sputtered by argon cluster ion beams. **Diamond and Related Materials**. 68: 37.
- Zhang, T. F., Wan, Z. X., Ding, J. C., Zhang, S., Wang, Q. M. and Kim, K. H. (2018). Microstructure and high- temperature tribological properties of Si- doped hydrogenated diamond-like carbon films. **Applied Surface Science**. 435: 963.

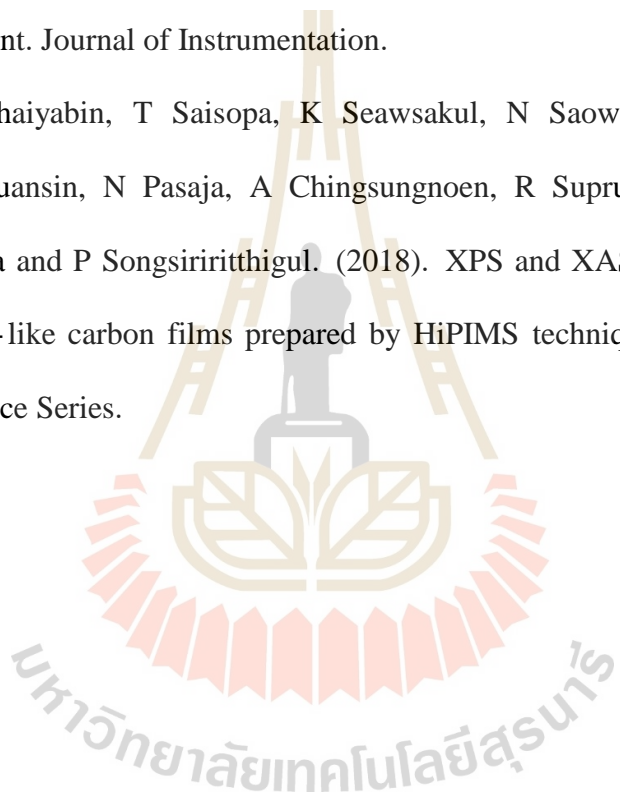


APPENDIX

APPENDIX

P. Chaiyabin, J Lomon, K.L. Giboni, K. Han, X. Ji, P. Juyal, C. Kobdaj, J. Liu, J. Lomon, N. Pasaja, P. Poolcharuansin, S. Rujirawat, P. Songsiriritthigul, Y. Yan and L. Zhao. (2017). Novel field cage design for the PandaX III double beta decay experiment. *Journal of Instrumentation*.

J Lomon, P Chaiyabin, T Saisopa, K Seawsakul, N Saowiang, K Promsakha, P Poolcharuansin, N Pasaja, A Chingsungnoen, R Supruangnet, N Chanlek, H Nakajima and P Songsiriritthigul. (2018). XPS and XAS preliminary studies of diamond-like carbon films prepared by HiPIMS technique. *Journal of Physics: Conference Series*.



CURRICULUM VITAE

Name: Ponthip Chaiyabin

Date and Place of Birth: February 13, 1994, and Nakhon Phanom, Thailand

Educations:

- 1999 - 2010; Junior High School in Ratsamakkee School, Nakhon Phanom, Thailand
- 2009 - 2012; Senior High School in Nawa Pittayakom School, Nakhon Phanom, Thailand
- 2012 - 2016; B.Sc. Physics in Khon Kaen University, Thailand
- 2016 - 2020; M.Sc. Applied Physics in Suranaree University of Technology, Thailand
- 2017; Researcher of M.Sc. Applied Physics (SUT) in Shanghai Jiao Tong University, China

Awards: 2017; SISSA paper in Journal of Instrumentation

Grants and Fellowships: Synchrotron Light Research Institute Scholarship, SUT, CHE-RNU project (SUT-COE: High Energy Physics & Astrophysics), and Thailand Research Fund (TRF)

Position and Place of work: M. Sc. Student in School of Physics, Institute of Science, Suranaree University of Technology 111 University Avenue, Sub District Suranaree, Muang District, Nakhon Ratchasima 30000, Thailand